Components for quantum computing based on optical transitions in single quantum dots

Matthew A. Pooley
Churchill College
University of Cambridge

A dissertation submitted for the degree of
Doctor of Philosophy
November 2012

Declaration

This dissertation is the result of work carried out in the Semiconductor Physics Group at the Cavendish Laboratory and the Cambridge Research Laboratory of Toshiba Research Europe Limited, from October 2009 to October 2012.

This dissertation is my own work and contains nothing which is the outcome of work done in collaboration with others, except as specified in the acknowledgement and text. It has not been submitted in part, or as a whole, for any degree at this, or any other, university. It does not exceed 60,000 words.

Matthew Pooley
Churchill College
November 2012

Acknowledgements

Financial support for this work was provided by the EPSRC and Toshiba Research Europe Limited (TREL).

I am very grateful to my supervisors, Prof. David Ritchie at the Cavendish and Dr. Andrew Shields at TREL. They have welcomed me into their groups and provided me with the fantastic opportunity to conduct interesting research in a very pleasant environment.

I also want to acknowledge Dr. Anthony Bennett, who has been a source of advice and inspiration throughout my PhD. His detailed knowledge of semiconductor physics and quantum optics has been invaluable and his helpful guidance for the last 3 years has been very much appreciated.

Thanks must go to many other people. Dr. Ian Farrer grew all the wafers used in this project, and Ken Cooper taught me the cleanroom processing skills needed to make devices from them. Dr. Raj Patel and Dr. David Ellis kindly fabricated the micropillar samples used in this work. Dr. Martin Ward has tirelessly organised our Helium needs. In addition, Dr. Niklas Sköld, Dr. Mark Stevenson, and Dr. Joanna Skiba-Szymanska must be thanked for many productive discussions.

Also, I want to thank all the people who have made my time here in Cambridge so very enjoyable. Edmund, Marc, Matt, Rob, Cameron, and Antoine to name but a few. Finally a special thanks must go to Katie, whose constant support and encouragement have been a great source of strength.

TOSHIBA

Journal Publications

1. *Electric-field-induced coherent coupling of the exciton states in a single quantum dot*
   A. J. Bennett, **M. A. Pooley**, R. M. Stevenson, M. B. Ward, R. B. Patel, A. Boyer de la Giroday, N. Sköld, I. Farrer, C. A. Nicoll, D. A. Ritchie, A. J. Shields
   Nature Physics, 6, 947 (2010)

2. *All-electrical coherent control of the exciton states in a single quantum dot*
   A. Boyer de la Giroday, A. J. Bennett, **M. A. Pooley**, R. M. Stevenson, N. Sköld, R. B. Patel, I. Farrer, D. A. Ritchie, A. J. Shields
   Phys. Rev. B 82, 241301 (2010)

3. *Free induction decay of a superposition stored in a quantum dot*
   A. J. Bennett, **M. A. Pooley**, R. M. Stevenson, I. Farrer, D. A. Ritchie, A. J. Shields
   Phys. Rev. B 84, 195401 (2011)

4. *Controlled-NOT gate operating with single photons*
   M. A. Pooley, D. J. P. Ellis, R. B. Patel, A. J. Bennett, K. H. A. Chan, I. Farrer, D. A. Ritchie, A. J. Shields
   Appl. Phys. Lett. 100, 211103 (2012)

Conference Proceedings

1. *Coherent coupling of the excitonic states in a single quantum dot*
   A. J. Bennett, **M. A. Pooley**, R. M. Stevenson, M. B. Ward, R. B. Patel, A. Boyer de la Giroday, N. Sköld, I. Farrer, C. A. Nicoll, D. A. Ritchie, A. J. Shields
   Proc. SPIE 7947, 794707 (2011)

2. *Observation of anticrossings in the exciton state of single quantum dots via electrical tuning of the fine-structure splitting*
   M. A. Pooley, A. J. Bennett, R. M. Stevenson, M. B. Ward, R. B. Patel, A. Boyer de la Giroday, N. Sköld, I. Farrer, C. A. Nicoll, D. A. Ritchie, A. J. Shields
   J. Phys.: Conf. Ser. 286, 012026 (2011)

3. *High-speed electrical control of a solid-state photonic quantum interface*
   A. Boyer de la Giroday, A. J. Bennett, **M. A. Pooley**, R. M. Stevenson, N. Sköld, R. B. Patel, I. Farrer, D. A. Ritchie, A. J. Shields
   Quantum Electronics and Laser Science Conference, OSA Technical Digest CD) (Optical Society of America, 2011), paper QThR6)

4. *Quantum light generation by semiconductor devices*
   A. J. Shields, A. J. Bennett, R. M. Stevenson, C. L. Salter, R. B. Patel, **M. A. Pooley**, M. B. Ward, A. Boyer de la Giroday, N. Sköld, I. Farrer, C. A. Nicoll, D. A. Ritchie
   Proc. European Quantum Electronics Conference (EQEC), CLEO/Europe and EQEC Conference Digest, OSA Technical Digest (CD) EA4 5 (2011)

5. *Semiconductor single photon devices for quantum information processing*
   O. Thomas, C. L. Salter, A. J. Bennett, R. M. Stevenson, **M. A. Pooley**, M. B. Ward, R. B. Patel, A. Boyer de la Giroday, N. Sköld, I. Farrer, C. A. Nicoll, D. A. Ritchie, A. J. Shields
   AIP Conf. Proc. 1363, 339-344 (2010)

Contributed Presentations

1. *Observation of anticrossings in the exciton state of single quantum dots via electrical tuning of the fine-structure splitting*
   M. A. Pooley, A. J. Bennett, R. M. Stevenson, M. B. Ward, R. B. Patel, A. Boyer de la Giroday, N. Sköld, I. Farrer, C. A. Nicoll, D. A. Ritchie, A. J. Shields
   Condensed Matter and Materials Physics 2010, Warwick (UK), 14 - 16 December 2010

2. *Electrical manipulation of a solid-state qubit* (Poster)
   M. A. Pooley, A. J. Bennett, R. M. Stevenson, M. B. Ward, R. B. Patel, A. Boyer de la Giroday, N. Sköld, I. Farrer, C. A. Nicoll, D. A. Ritchie, A. J. Shields
   Quantum Science and Technologies 2011, Rovereta (Italy), 9 - 12 May 2011

3. *Electrical control of quantum dot energy levels for quantum computing*
   M. A. Pooley, A. J. Bennett, R. M. Stevenson, M. B. Ward, R. B. Patel, A. Boyer de la Giroday, N. Sköld, I. Farrer, D. A. Ritchie, A. J. Shields
   Cavendish Laboratory Graduate Student Conference 2011, Cambridge (UK), 2 December 2011

4. *Coherent electrical manipulation of a quantum dot qubit*
   M. A. Pooley, A. J. Bennett, R. M. Stevenson, M. B. Ward, R. B. Patel, A. Boyer de la Giroday, N. Sköld, I. Farrer, C. A. Nicoll, D. A. Ritchie, A. J. Shields
   APS March Meeting 2012, Boston (USA), 27 February - 2 March 2012

In loving memory of my dear Noni.

Norma June Tognarelli
1931 – 2010

Summary

The optically active nature of direct bandgap semiconductors makes them well suited for applications in quantum optics. Semiconductor quantum dots (QDs) are particularly promising, due to their discrete atom-like energy levels. In this thesis, transitions between these energy levels are used to investigate the effects of electric and magnetic fields on the energy structure of single QDs, with a view to developing applications in the field of quantum computing.

In the work presented here a novel method of creating entangled photon pair emitters is presented, in which an electric field is used to tune the energy structure of single QDs to allow the fidelity of the emitted entangled state to be increased. In addition, a technique for the creation of energy-tunable entangled photon pairs is proposed and shown to be feasible with current technology.

Furthermore, the potential of QDs to act as an interface between photonic and spin qubits is explored. Application of a time varying electric field is used to dynamically tune the QD energy levels, allowing the evolution of excitons confined within single QDs to be manipulated. Using this system a controlled phase rotation of the exciton spin state is implemented.

Finally, indistinguishable single photons, emitted by the radiative decay of the exciton state, are used to generate the input state for an integrated-photonic two-qubit quantum logic gate. This is the first demonstration of a two-qubit gate using on-demand single photons. It is also the first demonstration of such a gate with all components realised using semiconductor materials.

Contents

Chapter 1

Introduction

Quantum computing is the use of quantum mechanical phenomena in order to allow computation which outperforms classical algorithms. The key difference between classical and quantum information processing lies in the properties of how the information is encoded. In classical computing information is encoded using a series of "bits", each of which can be in one of two different states. However, quantum computing encodes information using quantum bits (qubits), which can exist in superpositions of the possible states. In addition, quantum computing can take advantage of other novel properties of quantum mechanics, such as entanglement.

Optical quantum computing, in which information is encoded into the states of single photons, is a promising area of research. Using photons as qubits offers several advantages. For example, photons have long coherence lengths and travel at nature's speed limit, the speed of light. This makes them well suited for the transmission of quantum information. Also, individual photonic qubits can be manipulated by simply passing them through linear optics components, such as waveplates and beamsplitters. However, interactions between photonic qubits are difficult to achieve, which makes efficient methods of processing information encoded into photons cumbersome to implement.

The direct bandgap of the InGaAs quantum dots (QDs) studied in this work allows them to be used for several different applications in the field of

optical quantum computing. Of particular relevance to this thesis is the ability of single QDs to generate non-classical light, along with their ability to interact with individual photons to allow optically transmitted qubits to be converted into solid-state qubits, which are often easier to manipulate. Other quantum systems, such as isolated molecules or trapped ions, possess similar characteristics, however the use of semiconductor materials has several advantages. Specifically, the well established processing techniques developed by the electronics industry allows incorporation of semiconductor QDs conveniently into electronic and optical devices. As such, semiconductor QDs, and associated optical structures, provide an interesting environment in which to investigate quantum information applications with a view to developing a scalable quantum computing regime. Although the creation of a viable large scale quantum computer remains a long term goal, this thesis presents work towards the development of components which may be suitable for inclusion in such a computer.

1.1 Thesis overview

This thesis studies the effects of electric and magnetic fields on the energy structure of single QDs, via observation of photons emitted from transitions between different states. The known energy structure of QDs, along with other relevant background theory required in order to understand the experimental work, is introduced and explained in chapter 2. In addition, the devices and experimental methods used throughout the work presented in this thesis are detailed in chapter 3.

Much of the experimental work in this thesis concentrates on the effects of the fine-structure splitting (FSS) of the neutral exciton state. In chapter 4 a method of tuning this FSS using an electric field is introduced and characterised. This leads to a method of reducing the magnitude of the FSS, which is used to allow the observation of entanglement between photons emitted from the two neutral transitions. In addition, as the magnitude of the FSS is reduced, coherent coupling between the two eigenstates of the neutral exciton

is observed.

The effects of a magnetic field, applied to the QDs in conjunction with the electric field, are investigated in chapter 5. Two different magnetic field orientations are studied: one which allows the out-of-plane g-factor of confined excitons to be probed as a function of electric field; and one which tunes the FSS, thus allowing the application of two independent tuning mechanisms. A method of creating energy-tunable entangled photon pairs using these two mechanisms simultaneously is proposed and shown to be feasible.

The potential of using the exciton state as a solid-state qubit is also explored. In chapter 6 a method of transferring quantum information from photons into the spin of the exciton state is demonstrated. This allows the initialisation of a solid-state qubit, which is then manipulated with the application of a time varying electric field in order to dynamically control the FSS. The effects of the fluctuating nuclear magnetic field on the evolution of the exciton state are also investigated.

Finally, in chapter 7, a controlled two-qubit interaction is demonstrated using indistinguishable single photons from a single QD, emitted by the transition between the neutral exciton state and the ground state. This work is the first implementation of a photonic two-qubit gate where the input state is generated using an on-demand single photon source. Furthermore, all the components required for the gate are realised using semiconductor devices. As such, this work represents a significant step towards the creation of a scalable optical quantum computing regime in the solid-state.

Chapter 2

Semiconductor quantum dots

2.1 Introduction

Semiconductor quantum dots (QDs) are nanosized regions of semiconductor which can confine carriers to within their de Broglie wavelength, leading to a range of interesting quantum phenomena. The QDs studied in this thesis typically are lens shaped, with a diameter of $\sim$ 20 nm and an apex height of $\sim$ 5 nm. The work in this thesis is conducted using III-V semiconductor materials, with InAs QDs being encapsulated in GaAs or AlGaAs. The direct bandgap of these materials allows the QDs to be optically active, and therefore transitions between different QD states can emit or absorb photons easily.

In this chapter an overview of QDs is presented, beginning with an explanation of the effects of carrier confinement. This is followed by a discussion of the growth method used to create the QDs. Carrier creation via optical pumping is also explained. The energy structure of single QDs is then introduced, leading to a discussion of the optical transitions which are particularly important in this thesis. Finally, the effects of optical cavities on QD emission is included to aid in understanding the devices used throughout this thesis. For a more complete review of QDs see references [1, 2].

2.2 Carrier confinement

A brief summary of the important consequences of carrier confinement within QDs is included here, however a detailed explanation can be found in either [3] or [4].

Before considering the effects of quantum confinement, it is useful to first consider the energy and dispersion relation of particles in a semiconductor. Consider the Schrödinger equation for a carrier in a semiconductor,

$$\left[-\frac{\hbar^2}{2m^*}\nabla^2 + V(\mathbf{r})\right]\Psi(\mathbf{r}) = \epsilon_k \Psi(\mathbf{r}) \tag{2.1}$$

where $\hbar$ is the reduced Planck's constant, m^* is the effective mass of the carrier, $V(\mathbf{r})$ is the potential, and $\Psi(\mathbf{r})$ is the particle wavefunction with ϵ_k the corresponding energy eigenvalue.

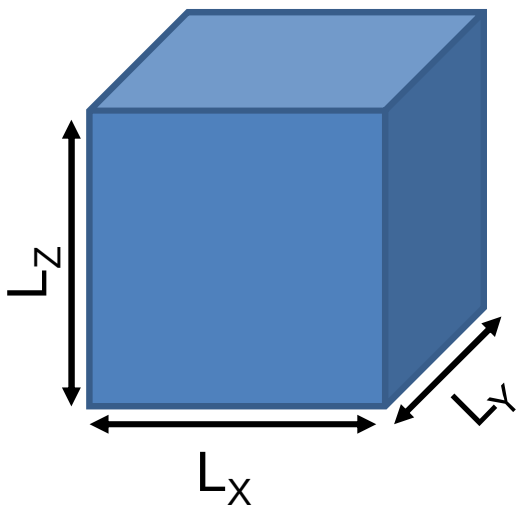

Figure 2.1: Diagram showing a semiconductor of finite dimensions L_x, L_y, L_z, as described in the main text.

The solutions to equation 2.1 for carriers subjected to the periodic potential of the semiconductor lattice are then of the form of Bloch functions

$$\Psi(\mathbf{r}) = u_k(\mathbf{r})\exp(i\mathbf{k}\cdot\mathbf{r}), \tag{2.2}$$

where $u_k(\mathbf{r})$ is periodic with the same period as the lattice potential, and $\mathbf{k}$ is the wavevector. For a finite semiconductor of dimensions L_x, L_y, L_z, $\mathbf{k}$ can only take certain discrete values given by

$$\mathbf{k} = k_x\hat{\mathbf{x}} + k_y\hat{\mathbf{y}} + k_z\hat{\mathbf{z}} \equiv \frac{2n_x\pi}{L_x}\hat{\mathbf{x}} + \frac{2n_y\pi}{L_y}\hat{\mathbf{y}} + \frac{2n_z\pi}{L_z}\hat{\mathbf{z}}, \tag{2.3}$$

where $n_{x,y,z}$ are positive integers. The corresponding energy eigenvalues, and dispersion relation, for states near to the band edges (i.e. states with $|\mathbf{k}|$ near zero for the direct bandgap semiconductors of interest here) are given by

$$\epsilon_k = E(\mathbf{k}) = \frac{\hbar^2|\mathbf{k}|^2}{2m^*}. \tag{2.4}$$

A carrier is confined when its motion is restricted to a length comparable or smaller than its de Broglie wavelength, which for carriers in a semiconductor is given by

$$\lambda_b \propto \frac{h}{\sqrt{m^* k_B T}} \tag{2.5}$$

where h and k_B have their usual meanings of Planck's and Boltzmann's constants, respectively, and T is the temperature. A reduction in the length of one dimension results in an increase in the separation between the allowed values of the corresponding component of $\mathbf{k}$, as can be seen in equation 2.3. Thus, confinement in a given direction results in quantization of the corresponding component of $\mathbf{k}$.

For InAs and GaAs, λ_b is of the order of 10 - 100 nm at the cryogenic temperatures used for the experiments detailed in this thesis. Therefore, the QDs used in this work, which have approximate dimensions of $20 \times 20 \times 5$ nm, confine carriers in all three spatial directions and act as zero-dimensional potential wells. The quantum confinement energy due to these wells can be estimated from the difference in energy of photons emitted from the ground state of the QDs and those emitted from the bulk GaAs surrounding material. The QDs studied in this thesis have confinement energies in the range of $\sim$ 90 - 175 meV.

2.2.1 Confinement-modified density of states

The density of states can be calculated by considering how much volume in k-space is required for each state, along with the volume element for small changes in $\mathbf{k}$, in the relevant geometry determined by the number of unconstrained dimensions.

For example, in a bulk semiconductor the carriers are free to move in all three spatial dimensions. For the corresponding three dimensional k-space, the volume occupied by each state is $V_{3\mathrm{D}} = \frac{8\pi^3}{L_x L_y L_z}$, and the volume element (see figure 2.2a) is given by $V_{\mathrm{dk}} = 4\pi|\mathbf{k}|^2\ \mathrm{d}\mathbf{k}$. The ratio of these quantities gives the density of states in k-space. Taking into account the two-fold spin degeneracy of the carriers, the density of states, per unit volume of real space V, is given by

$$D\left(\mathbf{k}\right)_{3\mathrm{D}} = \frac{2}{V}\frac{V_{\mathrm{dk}}}{V_{3\mathrm{D}}} = \frac{|\mathbf{k}|^2}{\pi^2}\ \mathrm{d}\mathbf{k}. \tag{2.6}$$

To get the density of states in terms of energy, E, the dispersion relation given in equation 2.4 can be used. From the dispersion relation $|\mathbf{k}| = \sqrt{\frac{2m^*E}{\hbar^2}}$ and $\mathrm{d}k = \sqrt{\frac{m}{2\hbar^2}}E^{-\frac{1}{2}}\ \mathrm{d}E$. Substitution into equation 2.6 yields

$$D(E)_{3D} = \frac{1}{2\pi^2}\left(\frac{2m^*}{\hbar^2}\right)^{\frac{3}{2}} E^{\frac{1}{2}}\ \mathrm{d}E \tag{2.7}$$

and so the density of states smoothly varies and is proportional to $\sqrt{E}$ for unconfined carriers in bulk semiconductor, as shown in figure 2.2a.

The volume element and the space occupied by each state depends on the number of unconstrained dimensions. Figures 2.2b and 2.2c show the k-space available to particles confined in one and two dimensions, respectively, along with the density of states as a function of energy. These are calculated using the same method as used above for the case of a bulk semiconductor and are given by,

$$\begin{aligned} D(E)_{2D} &= \tfrac{m^*}{\pi\hbar^2}\ \mathrm{d}E \\ D(E)_{1D} &= \sqrt{\tfrac{2m^*}{\pi^2\hbar^2}}E^{-\frac{1}{2}}. \end{aligned} \tag{2.8}$$

Note that the different possible values which the quantized components

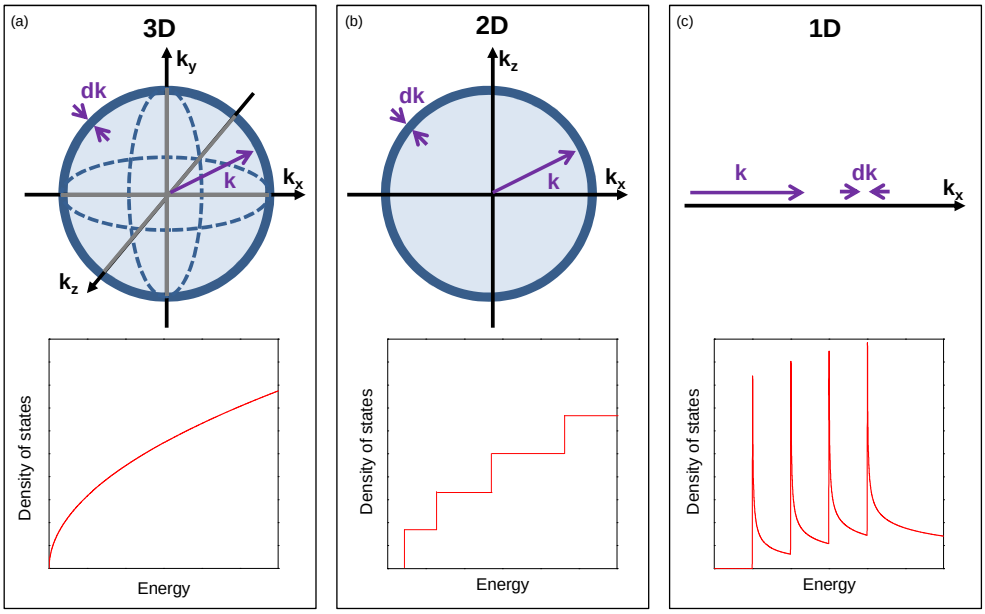

Figure 2.2: Diagram of fermi surface in k-space and the corresponding density of states for carriers free to move in three dimensions (a), two dimensions (b), and one dimension (c).

of **k** can take leads to the multiple energy levels seen in $D(E)_{2D}$ and $D(E)_{1D}$.

Density of states in QDs

QDs confine carriers in all three directions, with L_x, L_y, and L_z all comparable or smaller than λ_b. As a result, carriers in a QD are not free to move in any spatial direction. All three components of the carrier wavevector are then quantized and **k** can only take a set of discrete values with the energy of the corresponding states given by

$$E_{n_x,n_y,n_z} = \frac{\hbar^2}{2m^*}\left(\frac{2n_x\pi}{L_x} + \frac{2n_y\pi}{L_y} + \frac{2n_z\pi}{L_z}\right) \equiv E_{n_x} + E_{n_y} + E_{n_z} \tag{2.9}$$

Thus, the density of states for an ideal QD is a set of delta functions, one

for each combination of $n_{x,y,z}$, as described by

$$D(E)_{QD} = \sum_{n_x,n_y,n_z} \delta\left(E - E_{n_x} - E_{n_y} - E_{n_z}\right) \tag{2.10}$$

This gives rise to the discrete set of ladder-like energy levels depicted in figure 2.4. The transitions between these energy levels are of great interest to the work presented in this thesis.

2.3 Self assembled growth

There are a variety of methods available for the fabrication of semiconductor QDs, however all of the QDs studied in this work were grown via molecular beam epitaxy (MBE). MBE is a process which allows semiconducting material to be deposited epitaxially and allows precise control of layer thicknesses. A substrate wafer is held in an ultra high vacuum, and crucibles of the desired materials are heated until sublimation is achieved. The resulting stream of particles condense on the wafer and thus the sample is grown. The very slow growth rate, typically on the order of micrometers per hour, combined with heating of the substrate results in significant surface diffusion which allows reorganisation of the atoms into a stable ordered crystal.

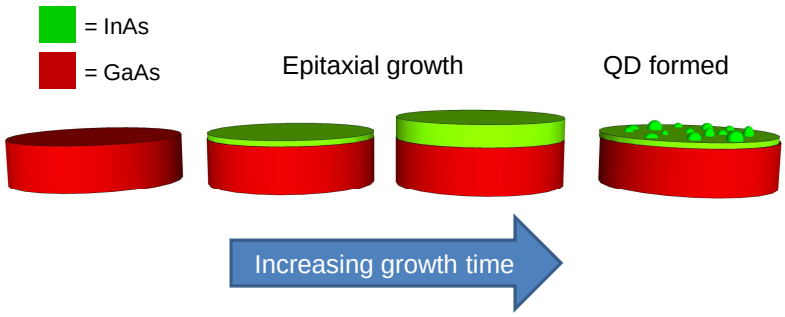

Figure 2.3: Diagram showing QD formation via Stranski-Krastanov growth. QD material is deposited on the lower cladding layer, growth is epitaxial until a critical thickness above which 3D islands spontaneously form.

MBE is well suited for depositing flat layers of material and creating

wafers with well defined planar structure. In order to create the three dimensional structures of QDs, Stranski-Krastanov growth is used[5, 6, 7]. This mode of growth relies on strain between different layers, due to the unequal lattice constants of the different materials, to achieve the formation of three dimensional islands. A layer of cladding material is grown onto which a thin layer of dot material is deposited. Initially the growth is epitaxial, however at a critical thickness, which is typically a few monolayers, the lattice mismatch induced strain results in the nucleation and growth of small three dimensional islands. The QDs are then capped in another layer of cladding material. This method of self-assembled growth results in a layer of QDs, with random lateral positions, on top of a thin epitaxial layer of the QD material. This thin layer from which the QDs emerge is known as the wetting layer and forms a two dimensional quantum well, the effects of which are clearly visible in optical spectroscopy. The QD growth process, and resulting structure, is shown schematically in figure 2.3.

2.4 Band structure

The three dimensional confinement potential of a QD is achieved via differences in the conduction and/or valence band energy of the QD material and the surrounding cladding material. Depending on the relative energies of the conduction and valence bands in the two materials it is possible for QDs to confine both electrons and holes, or to confine just one kind of carrier whilst repelling the other. Those that confine just one kind of carrier are known as type 2 QDs. In type 2 QDs the energy level of both the conduction and valence bands are offset from those of the surrounding material in the same direction. For example, in a type 2 QD which confines only electrons the conduction and valence levels of the QD material are both lower than those of the surrounding material, leading to a potential well for electrons in the conduction band but not for holes in the valence band. The QDs studied in this thesis are type 1 QDs which confine both kinds of carriers. To achieve this, the bandgap of type 1 QD material must be smaller than that of the

surrounding cladding material, in order to create a potential well for carriers in both the conduction and valence bands. The bandgap of GaAs, at a temperature of 300 K, is 1.424 eV and that of InAs is 0.354 eV. The resulting bandgap of the QDs is between these two values. This is because, although the QDs are grown using InAs, subsequent diffusion of Ga atoms leads to a mixed composition.

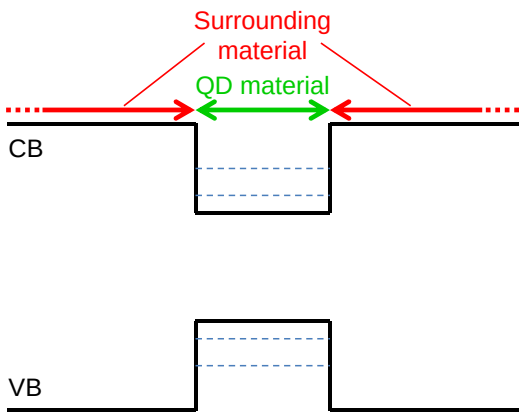

Figure 2.4: Schematic diagram of a one dimensional cross section of a QD band structure along the growth direction. The dot material has a smaller bandgap than the surrounding material, forming a potential well for both electrons in the conduction band and holes in the valence band. The confinement creates a ladder of discrete energy levels for carriers trapped in the QD, these are indicated schematically by dashed horizontal lines.

Figure 2.4 shows a schematic diagram of a one dimensional cross-section through the resulting band structure. Carriers in the surrounding material which enter the QD are trapped by the lower potential in the QD material. Confinement of electrons in the conduction band and holes in the valence band leads to a modification of the density of states as discussed above. This results in each kind of carrier occupying a discrete set of energy levels, two of which are shown schematically in figure 2.4 as dashed horizontal lines.

2.5 Optical excitation

The above sections explain how the band structure of a QD embedded within a semiconductor forms a potential that can trap carriers. In this section the origins of the carriers are discussed. In the region of the QDs the semiconductor is undoped and so the fermi energy lies between the top of the valence band and the bottom of the conduction band. Thus, at the cryogenic temperatures used throughout this thesis, the valence band is normally full and the conduction band is normally empty. Carriers can be introduced into the QDs using a variety of methods ranging from electrical injection[8, 9], such as in a light emitting diode, to more exotic methods involving surface acoustic waves, which can modulate the QD energy levels[10] or transport electrons through the semiconductor[11]. The method of carrier creation used for the work presented in this thesis is optical excitation, where electrons from the valence band are promoted across the bandgap into the conduction band via the absorption of a photon. The two different excitation schemes widely used throughout this thesis are detailed below.

2.5.1 Above-band excitation

In the above-band excitation regime the sample is excited by photons with an energy greater than the bandgap of the bulk GaAs which surrounds the QD layer. This creates a large amount of carriers around the region of the QD, some of which are captured in the wetting layer which forms a thin two-dimensional quantum well near the region of the QDs. The trapped carriers then decay via non-radiative processes, predominately via longitudinal-optical phonon scattering[12, 13], into the lowest unoccupied QD energy levels. An electron from the conduction band can then combine with a hole from the valence band with the emission of a photon. Due to the non-radiative relaxation prior to recombination of the electron-hole pair the emitted photon has a lower energy than the laser being used to excite the carriers. This difference in energy is useful as it allows the excitation laser to be easily removed from the collected emission via spectral filtering.

This method of carrier creation can populate all of the states, with variation of the excitation power and the applied electric field able to control the relative intensity of the various transitions which are studied. A single excitation wavelength can be used to study all the QDs in a given sample, as the carriers are created in the surrounding GaAs and so the rate of carrier creation does not depend on the energy levels of the individual QD being measured. These properties make above band excitation a useful regime for characterising samples and for measuring ensembles of QDs.

2.5.2 Quasi-resonant phonon assisted excitation

In the quasi-resonant phonon assisted excitation regime carriers are excited via phonon resonances. This is achieved by using excitation photons with an energy of

$$E = E_{|X\rangle} + E_{\text{phonon}}, \tag{2.11}$$

where $E_{|X\rangle}$ is the energy of the desired transition and E_{phonon} is the energy of a phonon. Thus an electron from the valence band can be promoted into the desired state, along with the creation of a phonon. In the GaAs/InAs material system used in this work, a suitable phonon resonance is found ~ 32 meV above the energy of the transition[14], which allows for spectral filtering of the laser light from the collected emission as in the above band regime.

In addition to driving individual transitions, quasi-resonant excitation leads to narrower lines in the emission spectrum and an improvement of the coherence time of the emitted photons compared to above band excitation. This is because quasi-resonant excitation only creates carriers in the QD and so fluctuations of the Coulomb potential around the QD are reduced relative to the above band case. However, due to the reduced absorbtion cross section, significantly higher excitation powers are required for quasi-resonant excitation. Furthermore, as quasi-resonant excitation selectively excites individual transitions, the energy of the excitation laser must be carefully tuned to match the phonon resonance of the particular QD being measured. Therefore, this method of excitation is useful for studying individual transitions in detail, but less convenient for observing all QD transitions simultaneously or

for rapid assessment of many QDs.

2.6 Electronic structure

The electronic energy structure of QDs is the focus of much of the work presented in this thesis. In chapters 4, 5 and 6 the effects of external electric and magnetic fields on the energy levels of single QDs is investigated. In chapter 7 a well defined transition between two QD states is used to emit indistinguishable photons for use in an optical logic circuit. In this section the electronic structure of single QDs is discussed, and the excited states, caused by carriers trapped within the QD, are introduced and defined.

2.6.1 Gross Energy Structure

As detailed in section 2.2, the gross energy level structure of carriers within a QD is determined by the 3D confinement potential, which results in a series of discrete energy levels leading to an emission spectrum composed of several narrow peaks. Each energy level can be occupied by up to two carriers with opposite spin, in accordance with the Pauli exclusion principle. The QDs studied in this thesis can trap electrons in the conduction band, holes in the valence band, or a combination of both electrons and holes. The number of confined energy levels is determined by the size of the QD and the difference in bandgap between the QD and the cladding material.

The state of a QD is defined by the number of carriers confined within it. The ground state, $|0\rangle$, corresponds to an empty QD containing no trapped carriers. The neutral exciton state, $|X_1\rangle$, corresponds to one confined exciton. The neutral biexciton state, $|X_2\rangle$, corresponds to two confined excitons. In general, the nth neutral state corresponds to n electron-hole pairs and is denoted $|X_n\rangle$. It is also possible for a QD to confine unpaired electrons or holes, leading to states with a net electric charge. A charged state with m unpaired electrons or holes and n electron-hole pairs is denoted $|X_n^{\pm m}\rangle$. This thesis only considers transitions involving the ground state and excited states in which the confined carriers occupy exclusively the lowest energy

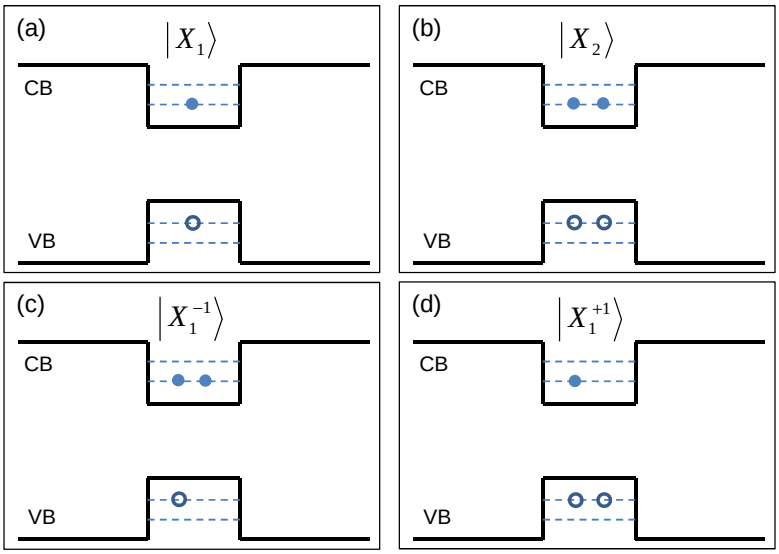

Figure 2.5: Diagram of the carrier configurations corresponding the states studied in this thesis. (a)-(b) neutral exciton and biexciton states, respectively. (c)-(d) Negative and positive singly charged exciton states, respectively.

level in the conduction or valence band; i.e. the neutral exciton ($|X_1\rangle$), the neutral biexciton ($|X_2\rangle$), and the singly charged exciton states ($|X_1^{\pm 1}\rangle$). The carrier configurations corresponding to these states are shown in figure 2.5. Photons emitted from transitions involving other excited states are excluded using spectral filtering.

The transitions corresponding to each spectral line can be identified with certainty using a range of techniques including analysis of the emission intensity as a function of excitation power and applied electric field, and via temporal measurements of the radiative lifetimes.

2.6.2 Fine-structure of the neutral exciton

The gross energy structure is furnished with additional fine structure due to other effects, such as inter-carrier interactions. Of most significance to this thesis is the fine structure of the neutral exciton state[15]. The $|X_1\rangle$ state corresponds to the confinement of one exciton, comprised of an electron in the conduction band and a hole in the valence band. The electron has spin

$s = \pm\frac{1}{2}$. The hole dispersion curve is split, however it is the heavy holes with $j = \pm\frac{3}{2}$ which are dominant. The $|X_1\rangle$ state thus has four possible projections of its angular momentum with $m = \pm 1$ or $m = \pm 2$. The electron-hole exchange interaction lifts this four-fold degeneracy, resulting in two pairs of states with $m = \pm 1$ or $m = \pm 2$, as shown schematically in figure 2.6. The two states with $|m| = 1$ form a degenerate pair known as the 'bright states', due to fact that they can couple to photons which also have spin of ± 1. The two states with $|m| = 2$ do not couple to photons and so are known as the 'dark states'. Typically, transitions involving the dark states are only observed in the presence of a magnetic field. In addition, in QDs without in-plane rotational invariance the degeneracy of the bright states is lifted by anisotropy in the strain, shape, and composition of the QD, as well as by effects of crystal inversion asymmetry.

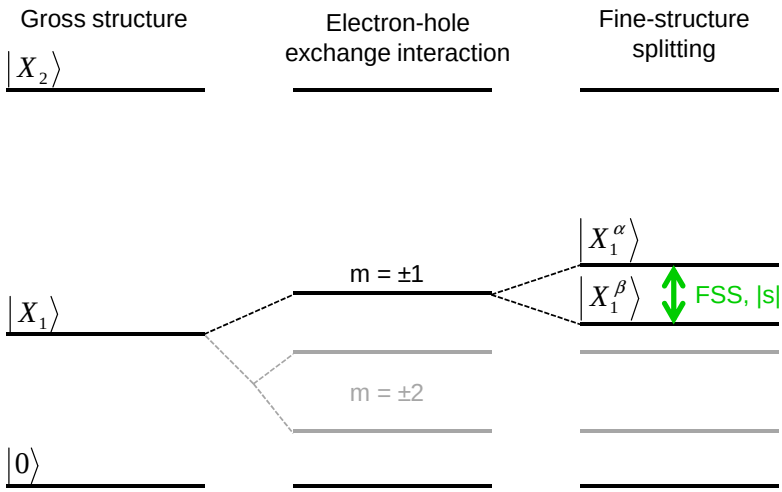

Figure 2.6: Diagram showing the energy structure of QD states. The exciton ($|X_1\rangle$) state is composed of four energy levels. The exchange interaction between electrons and holes splits the levels, as described in the main text. In QDs with in-plane anisotropy the bright states with $|m| = 1$ are separated by a fine structure splitting.

In the work presented in this thesis it is the bright states which are studied. The difference in energy between these two states is known as the fine-structure splitting (FSS), s, and results in the $|X_1\rangle$ state being split into

two spin-dependent energy eigenstates $|X_1^\alpha\rangle$ and $|X_1^\beta\rangle$. Transitions involving $|X_1^{\alpha,\beta}\rangle$ emit linearly polarised photons, with the axis of polarisation orientated parallel to the angular momentum of the relevant eigenstate. Typically, in the absence of an applied electric field, the two axes are orthogonal to each other with one axis parallel to the [110] crystalline axis. This is thought to be due to the strain effects which result in an elongation of the QDs along the [110] axis[16, 17, 18].

2.7 Neutral biexciton cascade

The radiative relaxation process from the biexciton state to the ground state is known as the neutral biexciton cascade. This process is of central importance to much of the work presented in chapters 4 and 5. In addition, the emission from transitions between the neutral states is used to allow measurement of the FSS (see section 3.4). The neutral biexciton cascade emits two photons, one as each of the exciton electron-hole pairs recombine. As the first recombination happens in the presence of the remaining exciton the Coulomb potential is different for each of the recombination events. Thus, the two photons usually have different energy. Hence, in the absence of any fine-structure splitting, the neutral biexciton cascade results in two distinct lines in the QD emission spectrum.

Due to the fine-structure of the $|X_1\rangle$ state there are two possible decay paths for the neutral biexciton decay, one via $|X_1^\alpha\rangle$ and one via $|X_1^\beta\rangle$. This results in each emission line from both the $|X_2\rangle \rightarrow |X_1\rangle$ and $|X_1\rangle \rightarrow |0\rangle$ transitions being split into a pair of closely spaced lines with an energy separation equal to $|s|$.

The emitted photons are linearly polarised. As the two $|X_1^{\alpha,\beta}\rangle$ eigenstates have different spin (and thus a different orientation of angular momentum) the photons emitted from transitions involving each of the eigenstates have a different axis of polarisation. In fact, transitions involving $|X_1^\alpha\rangle$ emit photons with orthogonal linear polarisation to those involving $|X_1^\beta\rangle$. Figure 2.7a shows the two decay paths from the biexciton state to the ground state,

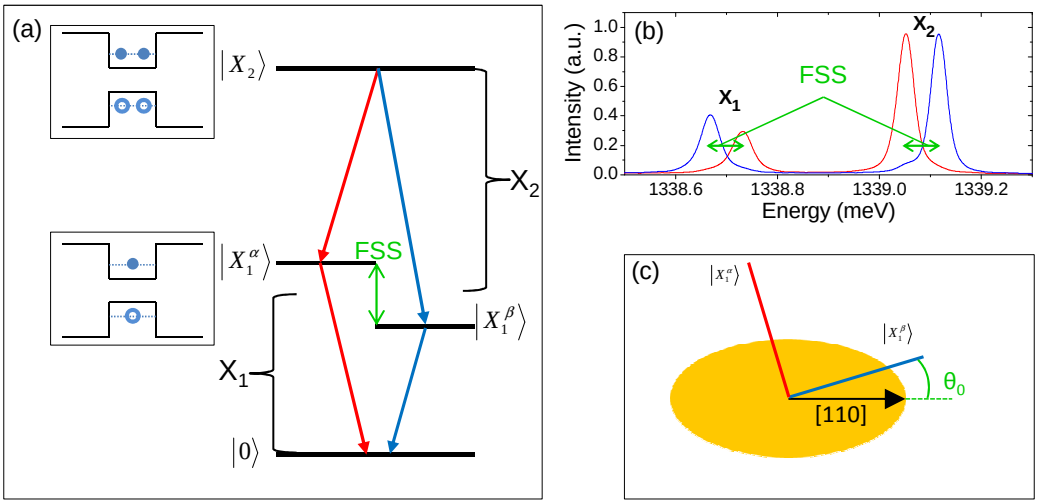

Figure 2.7: Features of the neutral biexciton cascade. (a) Diagram of the two radiative decay paths from the biexciton state, inset boxes show the carrier configuration of each state. The pair of transitions referred to as the biexciton (exciton) transitions are labeled X_2 (X_1). The transitions are shown with arrows which are colour coded to indicate the polarisation of the resulting photon. (b) Polarised PL emission from the neutral transitions, colours correspond to the decay paths indicated in (a). Peaks are labeled according to the initial state of the corresponding transition. (c) Diagram showing θ_0, the angle between the polarisation basis of the neutral emission, and thus the orientation of the eigenstates, relative to the [110] crystalline direction.

along with inset diagrams showing the carrier configuration in the QD at each level. Example polarised spectra, showing emission from the two decay paths, are shown in figure 2.7b and the effects of the FSS can clearly be seen.

The angle between the polarisation of the emitted photons and the [110] crystalline direction, as shown schematically in figure 2.7c, is labeled as θ_0. As discussed in detail in chapter 4 typically $\theta_0 \sim 0°$ and the eigenstates are closely aligned to the [110] and $[1\bar{1}0]$ direction.

2.7.1 State and transition notation

This section explains the main notation used throughout this thesis when referring to the energy levels and transitions involved in the neutral biexciton cascade, as the nature of the presented work makes the established notation inconvenient.

Typically in literature, the linear polarisation of the photons emitted by the neutral biexciton cascade are fixed, with one path emitting horizontally polarised photons and the other emitting vertically polarised photons in the lab frame. This leads to the common notation of $|X_1^H\rangle$ and $|X_1^V\rangle$ for the two $|X_1\rangle$ eigenstates. The resulting photons are often referred to by their polarisation using similar notation, such that a horizontally polarised photon emitted by the $|X_1^H\rangle \rightarrow |0\rangle$ transition is denoted as $|H\rangle$. Using this convention, the two-photon state resulting from the horizontally polarised decay path is denoted $|HH\rangle$ and that of the vertically polarised decay path is denoted $|VV\rangle$.

In the work discussed in this thesis the orientations of the eigenstate angular momentum, and thus the axes of linear polarisation of the photons emitted by the neutral biexciton cascade, are not fixed. This variation in the orientation of the polarisation makes the notation described above cumbersome. For example, photons emitted from transitions involving the state denoted $|X_1^H\rangle$ will not always emit photons with horizontal polarisation in the lab frame.

To prevent any confusion a new notation convention has been used throughout this thesis. The two exciton eigenstates are labeled as $|X_1^\alpha\rangle$ and $|X_1^\beta\rangle$,

as detailed in section 2.7. Photons emitted from transitions involving $|X_1^\alpha\rangle$ are denoted $|\alpha\rangle$ and those from transitions involving $|X_1^\beta\rangle$ are denoted $|\beta\rangle$. Correspondingly, the two-photon states resulting from each of the neutral biexciton decay paths are $|\alpha\alpha\rangle$ and $|\beta\beta\rangle$.

In addition, it is also useful to re-label the common polarisation bases. In order to measure entanglement between the photons emitted from the neutral biexciton cascade the emission is usually analysed in three polarisation bases, two linear bases offset by 45° and the circular basis. It is common in previous work to use the the rectilinear basis, labeled $\{H, V\}$, where the two axes of polarisation are horizontal and vertical in the lab frame; the diagonal basis, labeled $\{D, A\}$, where the two axes are at 45° to those of the rectilinear basis; and to label the right and left handed circular polarisation basis as $\{R, L\}$. However, in this work it is more convenient to define the polarisation bases relative to the orientation of eigenstates, rather than the lab frame. Thus, throughout this thesis the linear polarisation basis aligned with the polarisation of the two decay paths is labeled as $\{\alpha, \beta\}$, and the basis offset by 45° is labeled as $\{\alpha_{45}\beta_{45}\}$. The circular basis is unchanged by rotation of the linear axes in the equatorial plane of the Bloch sphere and so the standard notation is used.

2.8 Entangled photon pair emission

Much of the work presented in chapters 4 and 5 is motivated by the fact that the two photons emitted from the neutral biexciton cascade are entangled. This section gives a brief overview of entanglement and how it arises in the neutral biexciton cascade.

2.8.1 Entangled particles

An entangled wavefunction describing more than one particle cannot be factorised into a product of the individual wavefunctions of the constitute particles. One common example is the Bell state for two particles, here labeled

a and b, with two basis states $|0\rangle$ and $|1\rangle$, given by

$$|\Psi^+\rangle = \frac{1}{\sqrt{2}}\left(|0\rangle_a|1\rangle_b + |1\rangle_a|0\rangle_b\right) \equiv \frac{1}{\sqrt{2}}\left(|01\rangle + |10\rangle\right) \tag{2.12}$$

where $|0\rangle_a$ denotes that particle a is in state $|0\rangle$ etc. The two particles are entangled, as $|\Psi^+\rangle$ cannot be expressed as the product of each individual particle wavefunction. This is in contrast to the unentangled state given by

$$|\Phi\rangle = \frac{1}{2}\left(|00\rangle + |01\rangle + |10\rangle + |11\rangle\right) \tag{2.13}$$

which can be factorised in terms of each individual particle's wavefunction to give

$$|\Phi\rangle = \frac{1}{2}\left([|0\rangle + |1\rangle]_a \times [|0\rangle + |1\rangle]_b\right). \tag{2.14}$$

Systems described by the two wavefunctions, $|\Psi^+\rangle$ and $|\Phi\rangle$, have drastically different properties upon measurement. If the system is in state $|\Psi^+\rangle$ then measurement of one of the particles reveals the state of the other. For example, if particle a is individually measured to be in state $|0\rangle$ then the system wavefunction is collapsed into state $|01\rangle$ and subsequent measurement of particle b will always yield it to be in state $|1\rangle$. However, if the system is in state $|\Phi\rangle$ then measurement of one particle does not give information about the state of the other. In this case, if particle a is measured to be in state $|0\rangle$ then the system is either in state $|00\rangle$ or $|01\rangle$ and particle b is equally likely to be measured in either state.

2.8.2 Entangled pairs from the biexciton cascade

The two photons emitted by the neutral biexciton cascade are polarisation entangled, however unless $|s| = 0$ the resulting wavefunction describing the two emitted photons is not time-independent[19]. As shown in figure 2.7, there are two possible decay paths for the biexciton state. When the first electron-hole pair recombines both the $|X_2\rangle \rightarrow |X_1^\alpha\rangle$ and $|X_2\rangle \rightarrow |X_1^\beta\rangle$ transitions are equally likely, and thus the QD is left in a superposition of the two $|X_1^{\alpha,\beta}\rangle$ states. After a delay, τ_X, the remaining electron hole pair re-

combines with the emission of a second photon. Due to spin conservation, both photons have the same linear polarisation and thus the final two-photon wavefunction will be a superposition of the two possible decay paths, $|\alpha\alpha\rangle$ and $|\beta\beta\rangle$. Where the state $|\alpha\alpha\rangle$ corresponds to the first and second transition both involving exciton state $|X_1^\alpha\rangle$. As discussed in detail in references [19] and [20], during the time between the two emission events a phase difference, given by $\frac{|s|\tau_X}{\hbar}$, develops between the two possible states such that the two-photon wavefunction is given by

$$|\Psi\rangle = \frac{1}{\sqrt{2}}\left(|\alpha\alpha\rangle + \exp(\frac{i|s|\tau_X}{\hbar})|\beta\beta\rangle\right), \tag{2.15}$$

which, using the notation convention detailed in section 2.7.1, corresponds to

$$|\Psi\rangle = \frac{1}{\sqrt{2}}\left(|X_\alpha^2 X_\alpha^1\rangle + \exp(\frac{i|s|\tau_X}{\hbar})|X_\beta^2 X_\beta^1\rangle\right). \tag{2.16}$$

If $|s|$ is reduced to zero equation 2.15 becomes the maximally entangled Bell state given by

$$|\Psi^+\rangle = \frac{1}{\sqrt{2}}\left(|\alpha\alpha\rangle + |\beta\beta\rangle\right) \equiv \frac{1}{\sqrt{2}}\left(|X_\alpha^2 X_\alpha^1\rangle + |X_\beta^2 X_\beta^1\rangle\right) \tag{2.17}$$

and the two-photon state is time-independent, and thus ideally suited for applications which require a known input state such as quantum logic operations.

Note that even if $|s| > 0$ the emitted photons are still entangled, however time resolved measurements with a temporal resolution capable of resolving oscillations of frequency $\frac{|s|}{\hbar}$ are required in order to observe the entanglement. If the oscillation frequency is fast relative to the temporal response time of the measurement, the entanglement cannot be detected and instead classically correlated polarisation pairs are observed and the system has equal probability of appearing to be in either state $|\alpha\alpha\rangle$ or state $|\beta\beta\rangle$.

In addition, temporal filtering of emission from a QD with $|s| > 0$ can allow restoration of the time-independent state given in equation 2.17. This can be achieved by only selecting photon pairs which have a small value

of τ_X, i.e. filtering out events in which the time between detection of the biexciton and exciton photons is above a threshold value. Although this limits the phase differences accrued between the two eigenstate components of the collected photons, it also reduces the efficiency of the system due to a reduced count rate of photon pairs. A smaller value of $|s|$ leads to slower evolution of the exciton superposition state and thus less drastic temporal filtering is required to yield a useable entangled state. As a result, QDs with small $|s|$ are desirable.

2.9 Quantum dots in optical cavities

Placing QDs in optical cavities alters the spontaneous emission rate via modification of the optical density of states, $\rho(\omega)$. The spontaneous emission rate of a transition, $\frac{1}{\tau_R}$, is given by Fermi's golden rule:

$$\frac{1}{\tau_R} = \frac{2\pi}{\hbar}|\langle \mathbf{d} \cdot \mathbf{E} \rangle|^2 \rho(\omega), \tag{2.18}$$

where ω is the angular frequency of the photons, $\mathbf{d}$ is the dipole moment operator, $\mathbf{E}$ is the electric field operator, and $\langle \mathbf{d} \cdot \mathbf{E} \rangle$ is the matrix element of the perturbation between the initial and final states.

In a bulk semiconductor material the optical density of states, normalised over a volume V, is given by

$$\rho_0(\omega) = \frac{V n^3 \omega^3}{\pi^2 c^3}. \tag{2.19}$$

The presence of a Lorentzian cavity mode centered at frequency ω_c with width $\Delta\omega_c$ alters the optical density of states. The density of states then has the form

$$\rho_c(\omega) = \frac{2}{\pi \Delta\omega_c} \frac{\Delta\omega_c^2}{4(\omega - \omega_c)^2 + \Delta\omega_c^2} + \rho_0. \tag{2.20}$$

The emission rate of a transition resonant with such a cavity, $\frac{1}{\tau_{\mathrm{CAV}}}$, is found by substituting the modified density of states into equation 2.18. The factor by which the emission rate is changed is known as the Purcell

factor[21], F_p, and is given by the ratio of the emission rates with and without a cavity, such that $F_p = \frac{\rho_c}{\rho_0}$. If the transition is exactly on resonance with the cavity, i.e. it emits photons with $\omega = \omega_c$, is located at an antinode of the electric field inside the cavity mode, and its electric dipole is parallel to the cavity electric field, this is given by[22]:

$$F_p = \frac{3Q}{4\pi^2 V}\left(\frac{\lambda}{n}\right)^3 \tag{2.21}$$

where the volume, V, is now the volume of the cavity mode and $\frac{2\pi\lambda}{n} = \frac{c}{\omega}$. Thus the emission rate of transitions are increased when $F_p > 1$. Transitions which are resonant with the cavity experience an increased rate of emission, due to the increased optical density of states at the resonance. However, the factor by which the emission is increased decreases as the detuning between the cavity mode and a transition increases.

In addition to emitting at a modified rate, an emitter coupled to a cavity will emit photons preferentially into the cavity mode. Thus the cavity alters the angular distribution of the emitted photons. This is very useful as it leads to collimation of the emission, which increases collection efficiency. The fraction of photons which are emitted into the cavity mode is known as the spontaneous emission coupling factor, β_{se}. This is related to the Purcell factor and is given by

$$\beta_{\text{se}} = \frac{F_p}{1 + F_p}. \tag{2.22}$$

Note that the analysis presented in this section is only applicable to weak coupling, i.e. when the coupling rate between the emitter and the cavity is less than the radiative decay time. This is the case for the devices studied in the work presented throughout this thesis.

Chapter 3

Experimental methods and devices

3.1 Introduction

One of the key advantages of semiconductor quantum dots is that they are compatible with well developed processing techniques and can easily be integrated into a wide range of semiconductor devices. The results presented in chapters 4, 5, and 6 are obtained from QDs embedded inside diodes which allow the application of a vertical electric field. In chapter 7, pillar microcavity structures are used to enhance the temporal properties of photons emitted from QDs.

In this chapter, the structure and properties of the devices used in this work, and the experimental methods used to assess them, are discussed.

3.2 Devices

3.2.1 Electronic diodes

Electronic diode devices are used to allow the application of a vertical electric field to a layer of quantum dots. The diodes are designed to maximise the range of applied electric fields over which the quantum dots remain optically

active. The diodes are fabricated from a wafer grown via MBE. The structure and fabrication of the diode devices is described below.

Planar structure

The planar structure is grown on a commercially supplied substrate. First a 250 nm buffer layer of GaAs is deposited. Then a distributed Bragg reflector (DBR) consisting of 15 periods of alternating GaAs and AlGaAs layers is grown. Each layer in the DBR has a thickness of $\frac{\lambda_0}{4n}$, where λ_0 is the free-space wavelength for which the structure is optimised and n is the refractive index of the layer. On top of the DBR a 70 nm GaAs/AlAs superlattice is deposited. The superlattice consists of 31 periods of alternating GaAs and AlAs layers and is equivalent to a single layer of 75% AlGaAs. The use of a superlattice allows the effective alloy concentration to be controlled, without varying the rate of Al deposition, by changing the relative thicknesses of the GaAs and AlAs layers. Next a 5 nm layer of GaAs is deposited, onto which the InAs quantum dots are grown before being capped by another 5 nm layer of GaAs. Another 70 nm superlattice layer, identical to the previous one, is then deposited. Finally, 4.5 periods of a second GaAs/AlGaAs DBR are deposited, with equal layer thicknesses as used in the bottom DBR.

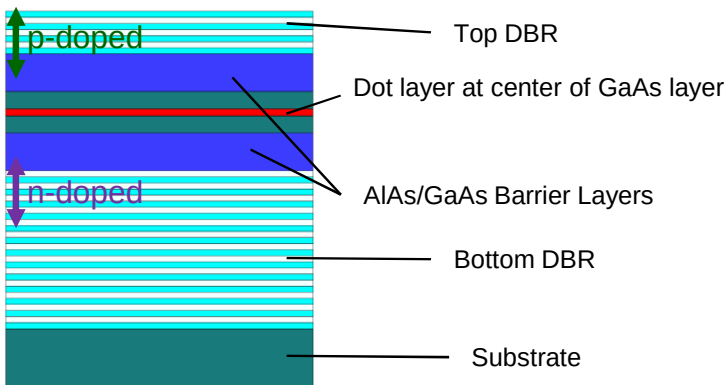

Figure 3.1: Diagram of wafer structure used for diode devices.

The resulting wafer structure is shown in figure 3.1. The superlattices create a two-dimensional potential quantum well, which significantly reduces

the rate at which carriers can tunnel out of the QD and thus drastically increases the range of electric field which can be applied without quenching the optical activity[23]. The two DBRs form a weak planar cavity, with the thickness of the superlattices and GaAs cladding layers chosen so that the optical length of the cavity is $\frac{\lambda_0}{2n}$.

Effects of a planar cavity

The high refractive index of III-V materials, relative to air, leads to total internal reflection of a significant fraction of the photons emitted by the QDs. This results in only 1-5% of QD emission penetrating the top semiconductor-air interface for QDs in a single semiconductor slab[24]. The collection efficiency is further limited by the numerical aperture (N_A) of the objective lens, as only photons which leave the semiconductor with angles less than $\sin^{-1}\left(\frac{N_A}{n_{\mathrm{GaAs}}}\right)$ are collected. Embedding the QDs in a planar cavity improves the collection efficiency, both by increasing the proportion of photons which leave the semiconductor from the top surface and by reducing the angular spread of the photons[25].

The DBRs which form the cavity have a very high reflectivity at the wavelength for which they are designed, due to constructive interference of reflections from successive layer interfaces. The reflectivity of a DBR at its design wavelength is determined by the refractive indices of the two materials which make up each period, n_1 and n_2, as well as those of the material either side of the DBR, n_a, n_b. The reflectivity increases with the number of mirror periods, N, and is given by

$$R = |r|^2 = \left(\frac{1 - \frac{n_b}{n_a}\left(\frac{n_1}{n_2}\right)^{2N}}{1 + \frac{n_b}{n_a}\left(\frac{n_1}{n_2}\right)^{2N}} \right)^2 . \tag{3.1}$$

Although the refractive indices are wavelength dependent, the major contributor to the wavelength dependence of the DBR reflectivity is the phase difference between successive reflections. This depends on the refractive index, n, and thickness, l, of each layer, and is given by $\delta = \frac{2\pi}{\lambda} 2nl$.

The effective reflection coefficient, Γ, for a DBR can be calculated using recursive iteration of the propagation and reflection matrices for each layer, as described in [26]. The value of Γ for interface I of a DBR is given by

$$\Gamma_I = \frac{r_I + \Gamma_{I+1} \exp(-i\delta)}{1 + r_I \Gamma_{I+1} \exp(-i\delta)}, \tag{3.2}$$

where $r_I = \frac{n_I - n_{I-1}}{n_I + n_{I-1}}$ is the reflection coefficient for layer I. Iteration of equation 3.2 from the final DBR interface forward to the first interface allows the total reflectivity, $|\Gamma_1|^2$, to be calculated. Figure 3.2a shows the calculated reflectivity as a function of wavelength for four DBRs, each of which has a different number of mirror periods. The design wavelength of the DBRs is $\lambda_0 = 930$ nm and around this wavelength destructive interference effects cause a highly reflective region known was the stopband. As the number of periods is increased the stopband becomes increasingly defined and its reflectivity increases.

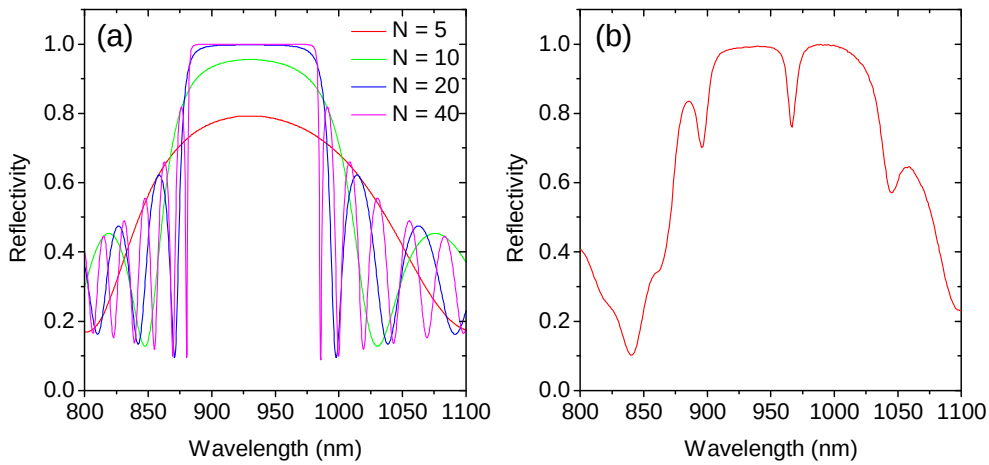

Figure 3.2: Reflectivity as a function of wavelength for planar structures. (a) Calculated reflectivity for four DBRs, each with a different number of mirror periods, N. The DBRs are deposited on a GaAs substrate and the design wavelength is $\lambda_0 = 930$ nm. (b) Measured reflectivity of a planar cavity wafer from which diode device used in this thesis were fabricated.

In the wafers studied in this thesis, a cavity layer is sandwiched between two DBRs. This cavity layer causes a narrow transmission window in the

stopband, resulting in the cavity mode. Photons with wavelength in this region can couple to the mode, as described in section 2.9, resulting in an increase in the collection efficiency as desired. Figure 3.2b shows the room temperature reflectivity of a wafer, with the planar structure described in section 3.2.1, from which some of the diode devices used in the thesis were fabricated. The cavity mode can clearly be seen around 966 nm. However, when cooled to 5 K the cavity wavelength shifts to around 930 nm.

Note that although the planar cavity increases collection efficiency it does not significantly alter the radiative lifetime of transitions. This is because of the large cavity volume which leads to a small Purcell factor, as shown in equation 2.21.

Diode fabrication

The structure described above is doped to place the QD layer at the center of the intrinsic region of a P-I-N diode. The bottom DBR and the first three periods of the bottom superlattice are n-doped with Silicon at a concentration of 1.75×10^{18} cm^{-1}. The last three periods of the upper superlattice and the top DBR are p-doped with Carbon at a concentration of 1×10^{18} cm^{-1}, apart from the top 5 nm of the wafer for which the dopant concentration is increased to 5.4×10^{19} to ensure a good ohmic contact between the wafer and metal contacts deposited on the top surface. The applied electric field, E, is calculated from $E = \frac{V-V_b}{d}$, where V is the potential difference between the n-type and p-type contacts, V_b is the built in potential due to the P-I-N junction, and d is the thickness of the intrinsic region. For the devices used in this work $V_b = 2.2$ V and $d = 140$ nm.

The diodes are fabricated using a combination of metal deposition via thermal evaporation and wet-etching. Optical lithography is used to pattern the features for both of these processes. An Aluminium shadow mask is first deposited on the wafer surface. Wet-etching is then used to expose an area of n-doped GaAs in the bottom DBR, onto which the n-type contacts are deposited using thermal evaporation of a Gold-Germanium-Nickel alloy. Thermal annealing ensures good penetration of the contacts into the n-doped

region of the wafer. A second wet-etching step is then used to define a mesa, with dimensions to accommodate the Aluminium shadow mask. The etch depth is such that the p-doped layer is penetrated but the n-doped layer remains intact. Finally, the p-contacts are deposited using thermal evaporation of 20 nm of Titanium followed by 100 nm of Gold. The resulting device structure is shown schematically in figure 3.3

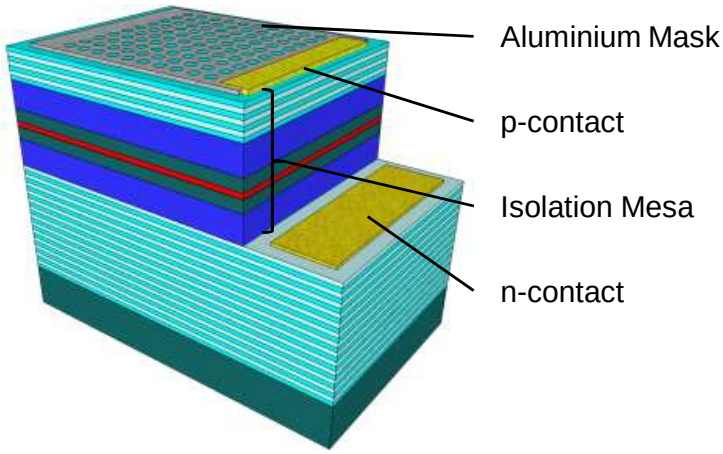

Figure 3.3: Diagram of diode devices.

The Aluminium shadow mask is patterned with an array of micron diameter holes. This allows small areas of the wafer to be optically addressed so that individual quantum dots can be probed. The mesa under the shadow mask serves to reduce the active volume of the device. This both limits the effects of wafer defects which can cause current leakage and reduces the capacitance, thus allowing the device to respond faster to changes in electric field. The majority of the work presented in this thesis was conducted on devices with mesa areas of 360×360 μm. However for the experiments in chapter 6 involving rapidly varying electric field a device with a mesa area of 35×60 μm was used.

3.2.2 Pillar microcavities

Pillar microcavities are used to alter the temporal properties of the emission from QDs via coupling between the QD transitions and the optical mode of the microcavity structure. As explained in section 2.9, this coupling enhances the rate of spontaneous emission from the coupled transition, thus reducing the radiative lifetime of the initial state.

Pillar structure and fabrication

As with the planar structure described above, the pillar microcavities are fabricated from wafers grown via MBE. The pillars are defined using a combination of optical lithography and reactive ion etching.

The planar structure of the pillars consists of a GaAs cavity of thickness $\frac{\lambda_0}{n}$ sandwiched between two unequal DBR mirrors. This is similar to that of the diode devices, however there are no superlattice layers and the sample is not doped. The pillars create three dimensional optical cavities. The DBRs provide vertical confinement, with the lateral confinement caused by the interface between the pillar edge and its surroundings.

The purpose of embedding QDs in pillar microcavities is to increase the rate and coherence time of photons emitted from QD transitions coupled to the cavity mode. This is achieved via Purcell enhancement of the emission, as described in section 2.9. In order to increase the Purcell factor the ratio of quality factor to cavity volume ($\frac{Q}{V}$) must be increased. Scattering caused by rough pillar sidewalls leads to a reduction of Q, necessitating optimisation of the etch conditions to increase sidewall smoothness. Furthermore, the quality factor can be increased by adding more periods to the DBRs. However, increasing Q reduces the spectral width of the cavity mode and thus reduces the probability of finding QDs which have transitions resonant with the cavity mode. The pillars used in this thesis have 17 (24) DBR periods above (below) the cavity.

The volume of the cavity can be decreased by reducing the pillar diameter. However this also reduces the Q, due to increased sidewall scattering. This leads to an optimum diameter which, for the samples used in this thesis, was

found to be around $1 - 3\mu$m.

3.3 Optical measurement techniques

For all optical measurements the sample is held in a cryostat and cooled using a continuous flow of liquid Helium. A heater and temperature sensor, embedded in the cold finger on which the sample is mounted, allow the sample temperature to be set by an automatic temperature controller. Most of the measurements are conducted at temperatures of ~ 5 K. The cryostat is equipped with electrical feedthroughs which allow voltages to be applied to the device if required. For all of the techniques described below, the objective lens is mounted on a 3-axis micrometer controlled positioning stage. This allows the location of the sample onto which the laser is focused, and from which emission is collected, to be varied.

3.3.1 Photoluminescence spectroscopy

The most widely used technique in this thesis is photoluminescence (PL) spectroscopy. The basic experimental configuration used for this technique is shown in figure 3.4a. The sample is optically excited by a laser, a variety of excitation regimes are used as described in section 2.5. The resulting QD emission is collected and collimated by an objective lens with a numerical aperture of 0.42. The QD emission is spectrally filtered to remove laser light before being dispersed by a spectrometer onto a liquid Nitrogen cooled Silicon charged coupled device (CCD) detector. The spectrometer, which has a focal length of 640 mm, has two interchangeable diffraction gratings: a coarse grating with line density of 600 mm^{-1}, which allows spectra over a wide wavelength range of 60 nm with a spectral resolution of 0.06 nm; and a fine grating with line density of 1800 mm^{-1}, which allows measurements over a smaller range of 10 nm but with a finer spectral resolution of 0.02 nm. White light can be combined coaxially with the excitation laser using a beamsplitter (BS2), and a removable beamsplitter (RBS) in front of the spectrometer allows imaging of the sample for positioning.

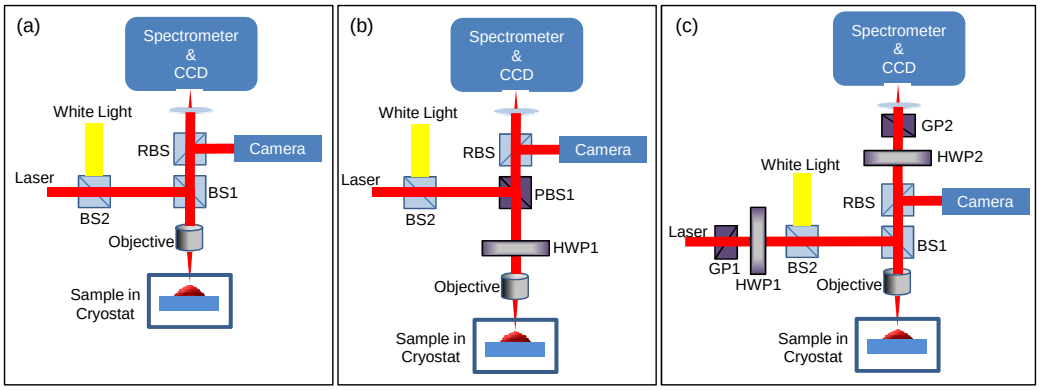

Figure 3.4: Diagram of experimental arrangement for PL spectroscopy. (a) Polarisation insensitive configuration, a beamsplitter (BS2) allows laser and white light to be combined and directed to the sample via another beamsplitter (BS1). An objective lens both focuses the laser and collects the QD emission, which is passed to a spectrometer. A removable beamsplitter (RBS) allows the sample to be imaged on a camera. (b) Configuration for performing linear polarised PL measurements. The set-up is as in (a) but a polarising beamsplitter (PBS1) and half-waveplate (HWP1) allow for polarisation selection. (c) Independent control of the excitation and emission polarisation is achieved by including two Glan-polariser and half-waveplate pairs, as described in the text.

The configuration shown in figure 3.4a is insensitive to the polarisation of the QD emission. The ability to measure the spectra as a function of polarisation is achieved by the addition of polarisation optics. In 3.4b the beamsplitter which directs laser light to the sample (BS1) is replaced with a polarising beamsplitter (PBS1) and a half-waveplate (HWP1) is inserted in front of the sample. Rotation of HWP1 rotates both the polarisation of the laser light which excites the sample, and that of the QD emission which is transmitted through PBS1 into the spectrometer.

Some experiments require independent control of the polarisation of the excitation laser and of the polarisation of the QD emission which is collected. This is achieved using the configuration shown in 3.4c. The laser polarisation is controlled by placing HWP1 and a Glan-polariser (GP1) directly in front of the laser; and a second half wave-plate (HWP2) and Glan-polariser (GP2) is used to control the polarisation of the emission which is transmitted into the spectrometer. Note that a non-polarising beamsplitter (BS1) is used to direct the laser onto the sample for this configuration.

3.3.2 Etalon spectroscopy

The resolution of the diffraction grating spectrometer described above is broader than the natural linewidth of the QD transitions. In order to accurately measure the shape and linewidths of transitions a wavelength tuneable etalon is used to perform detailed spectroscopy.

The etalon is composed of two mirrors separated by an air gap to form a highly reflective cavity with a narrow transmission range. The cavity length is controlled by piezo actuators which can vary the separation of the mirrors. This allows the wavelength of transmission to be selected by setting the voltage applied to the piezo actuators. The linewidth of the transmission band through the etalon is 0.8μeV, allowing accurate measurements of the QD transition linewidths which are typically on the order of 10μeV.

The configuration used to perform etalon spectroscopy is shown in figure 3.5, it is similar to that used for PL spectroscopy but before the QD emission reaches the spectrometer it is coupled into fiber and sent through the etalon

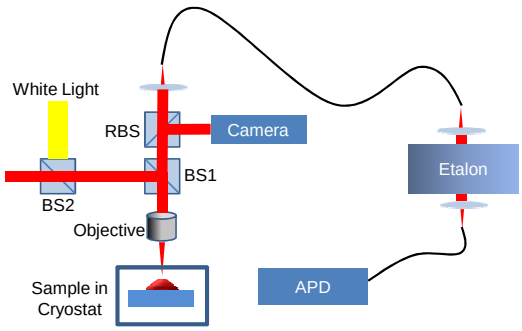

Figure 3.5: Diagram of the experimental configuration used to perform etalon spectroscopy.

to an avalanche photodiode detector (APD). The transmission wavelength is varied by sweeping the voltage applied to the piezo actuators, and the intensity detected by the APD is recorded. If polarisation control is required BS1 is replaced with a polarising beamsplitter and a half-waveplate is inserted in front of the sample. This method of spectroscopy has a narrow range and is time consuming, relative to using the diffraction grating spectrometer and CCD. Therefore it is only appropriate to use this method for specific measurements where an exceptionally fine resolution is required, such as measurements of the linewidth of transitions within single QDs.

3.3.3 Photoluminescence excitation spectroscopy

Information about the energy structure of a QD can be investigated using photoluminescence excitation (PLE) spectroscopy. This technique measures the intensity of transitions as a function of the excitation laser wavelength and allows resonances to be found.

The configuration used to perform PLE spectroscopy is shown in figure 3.6a. It is similar to that used for etalon spectroscopy but the etalon is replaced with a transmission grating. The QD is excited by a variable wavelength laser. The QD emission is spectrally filtered using a transmission grating to select the wavelength of the transition to be measured. The filtered emission is then sent to an APD and the intensity of the transition

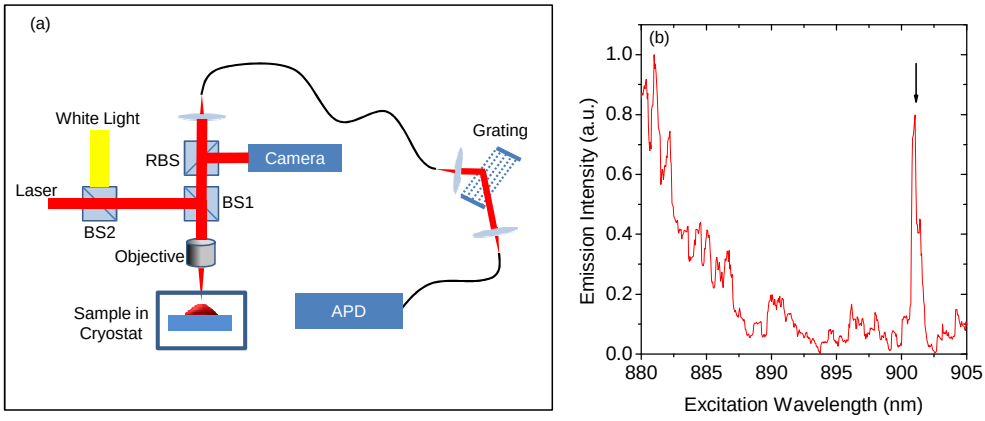

Figure 3.6: PLE measurements. (a) Diagram of the experimental configuration used to perform PLE spectroscopy. (b) Example PLE measurement of a $|X_1\rangle \rightarrow |0\rangle$ transition in a typical QD. The phonon resonance is indicated with an arrow.

is measured as the wavelength of the excitation laser is varied. Peaks in the transition emission intensity correspond to excitation resonances. Therefore they reveal information about the energy structure of the QD, such as the energy of the s-shell, p-shell, and other excited states which decay via the transition being measured. In this thesis, PLE spectroscopy is used to find the phonon resonances required for the quasi-resonant excitation scheme described in section 2.5. Figure 3.6b shows an example PLE measurement which shows a typical phonon resonance.

3.3.4 Time-resolved spectroscopy

It is possible to measure the temporal properties of individual transitions using time-resolved spectroscopy techniques. This is achieved using the configuration shown in figure 3.7a. The sample is excited with a pulsed laser and the desired transition is selected via spectral filtering with a transmission grating. The filtered emission is sent to an APD, which is used to trigger the start input of a Single Photon Counting Module (SPCM). The stop input of the SPCM is triggered using a signal generated from the excitation laser clock. This allows the timing of the photons emitted by the QD, relative to the excitation pulse, to be measured. One common use for this set up

is seen in section 7.4 where the radiative lifetime of the $|X_1\rangle$ state in a QD is measured by recording the temporal distribution of photons emitted from the $|X_1\rangle \rightarrow |0\rangle$ transition.

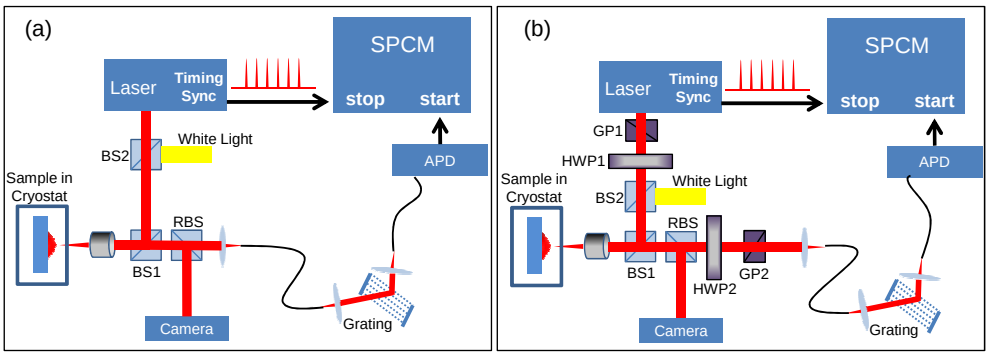

Figure 3.7: Diagram of experimental configuration used for time resolved spectroscopy of individual transitions. (a) Polarisation insensitive configuration, used for measurements of the radiative lifetime of excitons within QDs. (b) Inclusion of polarisation optics allows the polarisation of the excitation laser and the collected emission to be selected.

In chapter 6, polarised time-resolved spectroscopy is used to investigate the temporal evolution of the $|X_1\rangle$ state. To obtain these measurements, polarising optics are added to the time-resolved spectroscopy setup. Two half-waveplate and Glan polariser pairs are inserted: one directly after the laser (GP1 and HWP1) and one before coupling the emission into fiber (GP2 and HWP2), as shown in figure 3.7b. This enables the polarisation of the excitation laser and of the emission which is analysed to be individually selected, as required for the measurements detailed in section 6.2

3.3.5 Photon correlation measurements

Photon correlation measurements allow the relative timing of different photon detection events to be measured. As with time-resolved spectroscopy a SPCM is used, however both the start and stop signals are supplied by APDs which are triggered by photon detection events. This allows the time interval, τ, between the detected photons to be measured.

Several kinds of photon correlation measurements are used in this thesis. Polarised correlation measurements of the bi-exciton cascade are used to measure entanglement in chapter 4, and correlation measurements are crucial to the measurement of the optical CNOT gate presented in chapter 7. Outlined below are the principles of three important correlation measurement techniques.

Second-order autocorrelation

A second-order autocorrelation, $g^{(2)}(\tau)$, is a widely used technique for determining the quantum nature of an emitter. It is obtained by comparing the intensity, $I(t)$, of a signal with itself as a function of a time interval, τ, according to equation 3.3.

$$g^{(2)}(\tau) = \frac{\langle I(t)I(t+\tau)\rangle}{\langle I(t)\rangle\langle I(t+\tau)\rangle} \tag{3.3}$$

A second-order autocorrelation function can be measured using the set-up shown in figure 3.8a. Light from an emitter is split at a 50/50 beamsplitter, and sent to two APDs. One APD triggers the start input and the other triggers the stop input of the SPCM, and thus the time interval between emitted photons can be measured. The results are accumulated into a histogram showing the number of counts as a function of τ. Normalisation of this histogram yields $g^{(2)}(\tau)$.

A light source can be categorised according to the value of its second-order autocorrelation at $\tau = 0$. Classical light sources can only have $g^{(2)}(0) \geq 1$, as a classical wave can always have half of its intensity directed out of each of the outputs from the 50/50 beamsplitter. However, a single quantum emitter can have $g^{(2)}(0) < 1$, as an individual photon must exit from one of the beamsplitter outputs and cannot be split between them. An ideal single photon source, which emits exactly one photon at a time, has $g^{(2)}(0) = 0$, as it is impossible for a single photon to simultaneously be detected by both of the APDs.

Photon correlation measurements can be acquired under both continuous

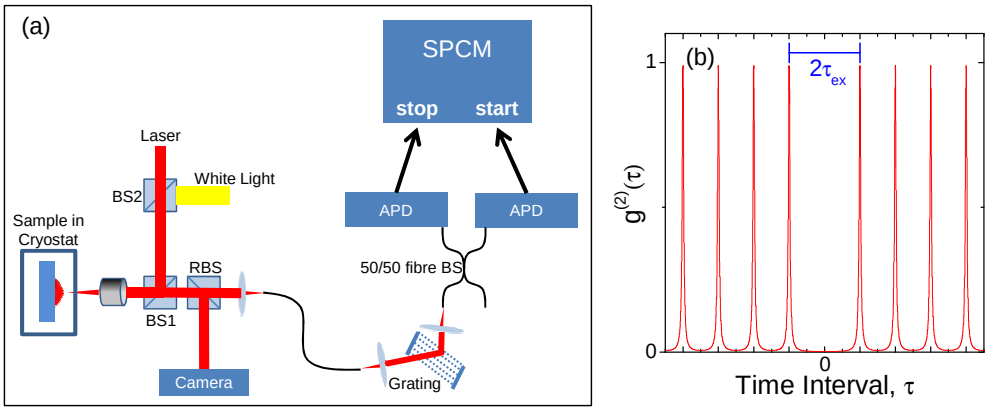

Figure 3.8: (a)Diagram of experimental configuration for the measurement of second-order autocorrelation functions. (b) Simulated $g^{(2)}(\tau)$ for an ideal single photon source with pulsed excitation at frequency $\frac{1}{\tau_{\text{ex}}}$.

wave or pulsed excitation regimes, as both the start and stop events are triggered by photons emitted from QDs. This is in contrast to the time-resolved spectroscopy described in section 3.3.4, where the timing of emitted photons is recorded relative a pulsed excitation laser. For the work in the thesis, second-order autocorrelation functions are measured under pulsed excitation such that the QD based emitters are excited at regular time intervals, τ_{ex}, by a pulsed laser. Under these conditions, peaks in $g^{(2)}(\tau)$ are expected when τ is equal to an integer multiple of τ_{ex}. A peak at $\tau = 0$ is only possible if multiple photons are emitted simultaneously. The relative area of the peak at $\tau = 0$ compared to the other peaks gives the probability of multi-photon emission. Figure 3.8b shows a simulated $g^{(2)}(\tau)$ for an ideal single photon source under pulsed excitation conditions.

Polarised second-order pair correlation

Polarised second-order pair correlation measurements are used in this thesis as a means to measure entanglement of photon pairs emitted from the neutral biexciton cascade, as outlined in section 4.5. These second-order pair correlations are calculated by comparing the intensity of emission from the two transitions in the cascade as a function of time interval, τ, as described

by

$$g^{(2)}_{P1,P2}(\tau) = \frac{\langle I_1(t) I_2(t+\tau)\rangle}{\langle I_1(t)\rangle\langle I_2(t+\tau)\rangle}, \tag{3.4}$$

where I_1 and I_2 are the intensities from the $|X_2\rangle \rightarrow |X_1\rangle$ and $|X_1\rangle \rightarrow |0\rangle$ transitions respectively. This is very similar to the second-order autocorrelation described by equation 3.3. However for the autocorrelation both the start and stop signal to the SPCM are triggered by photons from the same transition, but for the pair correlation the start signal is triggered by a photon from the $|X_2\rangle \rightarrow |X_1\rangle$ transition and then the stop signal is triggered by the subsequent photon from the $|X_1\rangle \rightarrow |0\rangle$ transition. The subscripts $P1$ and $P2$ indicate the polarisation of the start and stop photon, respectively.

Recall the two-photon state resulting from the neutral biexciton cascade given in equation 2.15,

$$|\Psi\rangle = \frac{1}{\sqrt{2}}\left(|\alpha\alpha\rangle + \exp(\frac{i|s|\tau_X}{\hbar})|\beta\beta\rangle\right) \tag{3.5}$$

where τ_X is the time interval between the two emission events and state $|\alpha\alpha\rangle$ ($|\beta\beta\rangle$) corresponds to both the photons being emitted via the $|X_1^{\alpha}\rangle$ ($|X_1^{\beta}\rangle$) state. Second-order pair correlation measurements are very useful for assessing this state as $g^{(2)}_{P1,P2}(\tau)$ is proportional to the probability that the two emitted photons are in state $|P1\ P2\rangle$.

Figure 3.9a shows a schematic diagram of the experimental measurement used to achieve this. The emission from a QD is spectrally filtered to separate the photons emitted by the $|X_2\rangle \rightarrow |X_1\rangle$ transition from those emitted by the $|X_1\rangle \rightarrow |0\rangle$ transition. To achieve this, the emission is split with a 50/50 beamsplitter, with light from the two beamsplitter outputs sent to different spectrometers. One spectrometer then selects the $|X_2\rangle \rightarrow |X_1\rangle$ transition and the other selects the $|X_1\rangle \rightarrow |0\rangle$ transition. Emission from the $|X_2\rangle \rightarrow |X_1\rangle$ transition is passed through a polarising beamsplitter. This selects emission from just one of the decay paths, which is then sent to an APD. Emission from the $|X_1\rangle \rightarrow |0\rangle$ transition is split at another polarising beamsplitter, and light from each of the two decay paths is sent to two separate APDs. The three APDs are used to trigger the start and stop inputs

on two synchronised SPCMs, allowing co- and cross-polarised second-order pair correlation measurements to be simultaneously acquired.

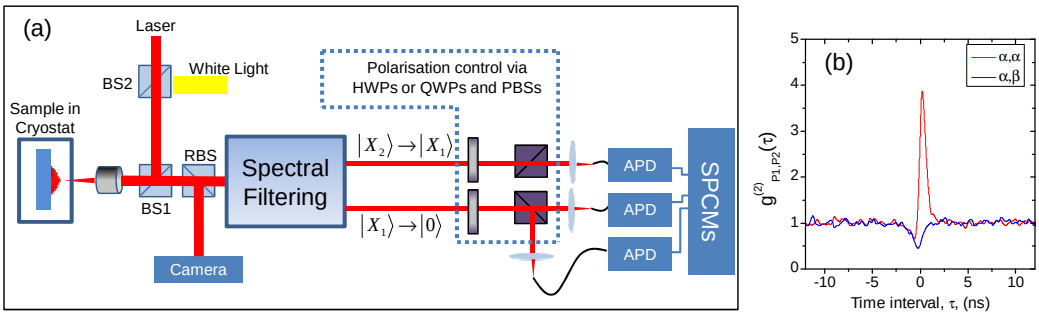

Figure 3.9: (a) Diagram of experimental configuration used for measuring second-order pair correlations as described in the text. (b) Example of second-order pair correlations for co- and cross-polarised emission in the basis aligned with the QD eigenstates. The legend indicates $P1, P2$ for each measurement. As explained in the main text the two measurements show that polarisation correlated photon pairs are likely to be emitted as expected.

Half-waveplates inserted in front of the two polarising beamsplitters allow the orientation of the linear polarisation basis being measured to be rotated. Replacing these with quarter-waveplates allows the circular polarisation basis to be measured. Thus, this configuration allows measurement of the second-order pair correlations required to observe entanglement between the two photons, as detailed in section 4.5.

The correlation measurements are normalised to the value of $g^{(2)}_{P1,P2}(\tau)$ for $|\tau| \gg 0$, as coincidence events in this time range correspond to photons from different cascade events and so are uncorrelated. Thus $g^{(2)}_{P1,P2}(\tau) = 1$ is expected for photon pairs with uncorrelated polarisation; $g^{(2)}_{P1,P2}(\tau) > 1$ indicates an increased probability of state $|P1\ P2\rangle$ being emitted; and $g^{(2)}_{P1,P2}(\tau 0) < 1$ indicates a suppression of state $|P1\ P2\rangle$, relative to the expected emission if each photon had random polarisation.

Figure 3.9b shows an example of a co- and cross polarised second-order pair correlation for a QD measured in the linear basis aligned to the eigenstate orientation. As discussed in section 2.7, each of the decay paths of the neutral biexciton cascade emits a pair of co-polarised photons. The effects of this

are clearly visible in the data. Coincidences with small positive values of τ correspond to cases where both photons are likely to be from the same cascade event. The co-polarised correlation shows a peak in this region as a result of the increased probability of the two photons having the same polarisation. Correspondingly, the cross-polarised correlation shows a dip below $g^{(2)}_{\alpha,\beta}(\tau) = 1$ in this region, indicating the reduced probability of the two photons having opposite polarisation. Coincidences with $-\tau$ correspond to events in which a photon from the $|X_1\rangle \rightarrow |0\rangle$ transition is detected before a photon from the $|X_2\rangle \rightarrow |X_1\rangle$ transition. Both data sets show a dip in $g^{(2)}_{P1,P2}(\tau)$ for small negative values of τ. This is because coincidences in this region are only possible if the $|X_2\rangle$ state is re-excited very quickly after the $|X_1\rangle \rightarrow |0\rangle$ transition has occurred, which is unlikely.

3.4 Measurement of fine-structure splitting

As detailed in section 2.6.2, the spectral lines due to the $|X_2\rangle \rightarrow |X_1\rangle$ and $|X_1\rangle \rightarrow |0\rangle$ transitions are each composed of a pair of linearly polarised lines separated in energy by the fine-structure splitting, s (see figure 2.6). Photons from the two decay paths have orthogonal polarisation and thus the fine-structure splitting can be measured using polarised PL-spectroscopy. This technique is used extensively in chapters 4 and 5.

The experimental set-up shown in figure 3.4b is used, allowing acquisition of polarised spectra as explained in section 3.3.1. To measure the fine-structure splitting, the angle of linear polarisation measured, θ, is rotated through 180° in increments of 11.25° and the emission spectrum is recorded for each polarisation. The lines due to the $|X_1\rangle \rightarrow |0\rangle$ and $|X_2\rangle \rightarrow |X_1\rangle$ transitions are fit with Lorentzian peaks, and the energy of the peak intensity for each line is extracted.

If $|s|$ is large enough to be clearly resolved by the spectrometer the two polarised transitions can clearly be seen, and the energy of the peak intensity abruptly changes when HWP1 is aligned with each of the transitions, as shown in figure 3.10a. It is trivial to extract the value of $|s|$ in this case.

If $|s|$ is below the resolution of the system, as in figure 3.10b, then the energy at which the peak intensity is detected appears to vary sinusoidally between the energy of the two transitions, as the relative contribution from each transition is varied. For each polarisation, the difference in energy between the $|X_2\rangle \rightarrow |X_1\rangle$ and $|X_1\rangle \rightarrow |0\rangle$ transitions, $\Delta E_{X_2-X_1}(\theta)$,is calculated. Calculating the difference between the two lines removes any systemic drift due to rotation of the polarisation optics, which can cause small deflections to the path of the emitted light. A sinusoidal function is fit to $\Delta E_{X_2-X_1}(\theta)$, with the peak-to-peak amplitude of the sinusoid equal to $2|s|$, as shown in figure 3.10c.

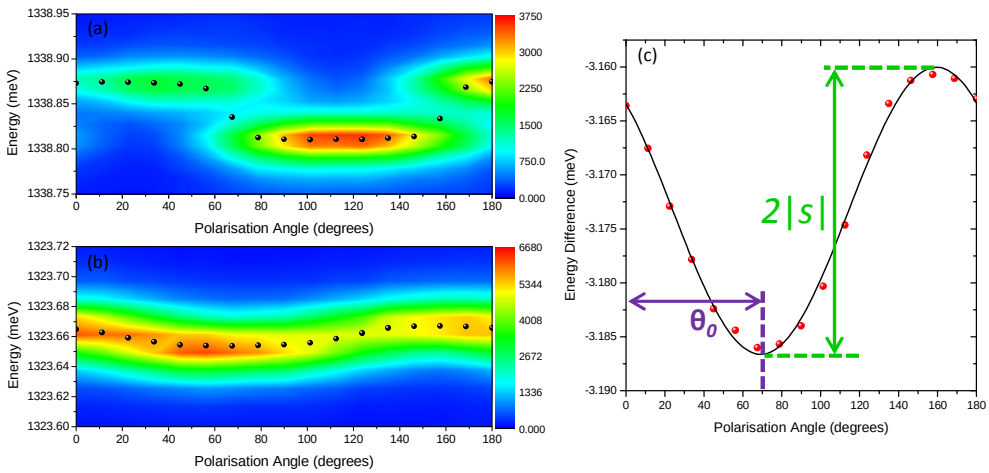

Figure 3.10: Method of measuring fine-structure splitting. (a) and (b) show emission spectra the $|X_1\rangle \rightarrow |0\rangle$ transition as a function of linear polarisation angle from two quantum dots with $|s|$ $65\mu eV$ and $|s|$ $12\mu eV$ respectively. Black spheres show the energy of peak intensity which is extracted from a Lorentzian fit. For cases where $|s|$ is smaller than the system resolution the difference in energy between the two neutral transitions is calculated as a function of polarisation angle. A sinusoidal fit then allows $|s|$ and the orientation of the state polarisation basis, θ_0, to be extracted as shown in (c).

In principle it is possible to measure $|s|$ by simply acquiring two polarised spectra, one aligned with each of the polarisation axes. However, the method described above allows much smaller values of $|s|$ to be accurately measured. In addition, using multiple polarisation angles between 0° and 180° allows

the orientation of the eigenstates to be measured. This is the actual angle, θ_0, which the polarisation basis makes with the crystalline axis and is obtained from the phase of the fit to $\Delta E_{X_2-X_1}(\theta)$ as shown in figure 3.10c.

Chapter 4

Electrical manipulation and coherent coupling of the exciton states in single quantum dots

4.1 Introduction

As detailed in Chapter 2, the energy structure of single quantum dots provides a simple level system which is well suited for demonstrations of quantum phenomena in the solid-state. The neutral biexciton cascade is of particular interest as it can be used as a source of entangled photon pairs[27]. However in order for the entangled state to be practically useful, the fine structure splitting, s, of the $|X_1\rangle$ state must be small, as detailed in section 2.8. This has motivated significant work into methods to reduce $|s|$.

Several methods have been demonstrated for tuning the FSS. Manipulation of the strain field has been much studied, with early attempts to reduce $|s|$ involving the piezoelectric application of strain[28]. Although promising, these initial experiments were not able to bring the FSS close to zero. However, more recently the effects of strain on the exciton eigenstates and the FSS have been understood in more detail[29, 30, 31]. A theoretical analysis

of different QD symmetries is presented by Singh and Bester[29], where they show that the application of uniaxial stress can only eliminate the FSS in ideally symmetric QD. For experimentally realised QDs they predict that there will be a lower bound below which the FSS can not be reduced, and that the orientation of the exciton eigenstates rotates as the system is swept through the resulting anticrossing. This work is built upon by Gong *et al.*[31], who establish a theoretical relationship between the applied strain and properties of the exciton eigenstates, such as their orientation and the FSS. In addition, they demonstrate that the minimum values attainable for the FSS under the application of strain can be estimated from measurements made at zero external strain, thus allowing QDs with small enough minimums to be preselected for further study easily. These findings are of particular relevance to the work presented in this chapter, where similar behaviour is observed experimentally whilst tuning the FSS using the application of an electric field.

Other approaches which have been investigated include the application of magnetic fields[32, 33], strong coherent lasers[34, 35], lateral electric field[36, 37, 38], and vertical electric field[39, 40]. Those studies that have been able to minimize the FSS have observed the states to cross through each other[32, 34, 35, 36, 37].

Tuning of the FSS via application of a vertical electric field is possibly the most convenient technique yet reported. However previous work using this method has been limited by the low confinement potential of QDs, which results in carriers tunneling from the QDs at field magnitudes on the order of tens of kilovolts per centimeter. Thus, only relatively small changes in $|s|$ have been observed using this method to date. The work presented in this chapter overcomes this limitation via the use of the diode devices described in chapter 3. In these devices the QDs are embedded in a two-dimensional quantum well which increases carrier confinement and allows large electric fields, on the order of a few hundred kilovolts per centimeter, to be applied without carrier tunneling quenching optical emission (see section 3.2.1 and figure 3.1).

In this chapter, a linear shift in $|s|$ over a range of $\sim 100\mu$eV is reported,

due to the two $|X_1\rangle$ eigenstates ($|X_1^\alpha\rangle$ and $|X_1^\beta\rangle$) undergoing Stark shift at different rates. As $|s|$ is reduced, an anticrossing of the eigenstates is observed. This imposes a minimum value, s_0, below which $|s|$ can not be reduced using this method. In addition, close to the anticrossing hybridization of the $|X_1^\alpha\rangle$ and $|X_1^\beta\rangle$ states induces a rotation in the linear polarisation of the photons emitted from the two $|X_1^{\alpha,\beta}\rangle \rightarrow |0\rangle$ transitions. The angle between the axes of linear polarisation and the [110] crystalline direction, θ_0, is observed to rotate through $\sim 90°$ as the system is swept through the anticrossing. The behaviour of the system is well described by a coherent coupling model, which allows the variation in both $|s|$ and θ_0 to be explained. Finally, entangled-photon-pair emission is measured from the neutral biexciton cascade of a QD which has a minimum $|s|$ of $s_0 = 1.4\mu$eV [41].

4.2 Sample characterisation

The results presented in this chapter are obtained from studies of QDs embedded in P-I-N diodes, as described in detail in chapter 3 section 3.2.1. These devices allow the application of a vertical electric field, parallel to the growth direction of the sample. In addition, a patterned shadow mask on the top surface of these devices creates micron sized apertures through which individual QDs can be optically addressed. This allows photoluminescence (PL) spectroscopy measurements to be used to investigate the effects of electric field on the energy level structure of single QDs.

The samples are cooled to ~ 5 K using liquid helium in a continuous flow cryostat and polarised PL spectroscopy measurements are acquired using the methods detailed in section 3.3.1. For measurements of the FSS, the sample is optically excited using the above-band method described in section 2.5, as this method can drive both of the $|0\rangle \rightarrow |X_1^{\alpha,\beta}\rangle$ transitions. Figure 4.1a shows the PL emission from a typical quantum dot as a function of electric field. The parabolic variation in the emission energy due to the Stark shift can clearly be seen. The relative intensity of the different transitions also varies, as the electric field strongly affects the tunneling rates of electrons

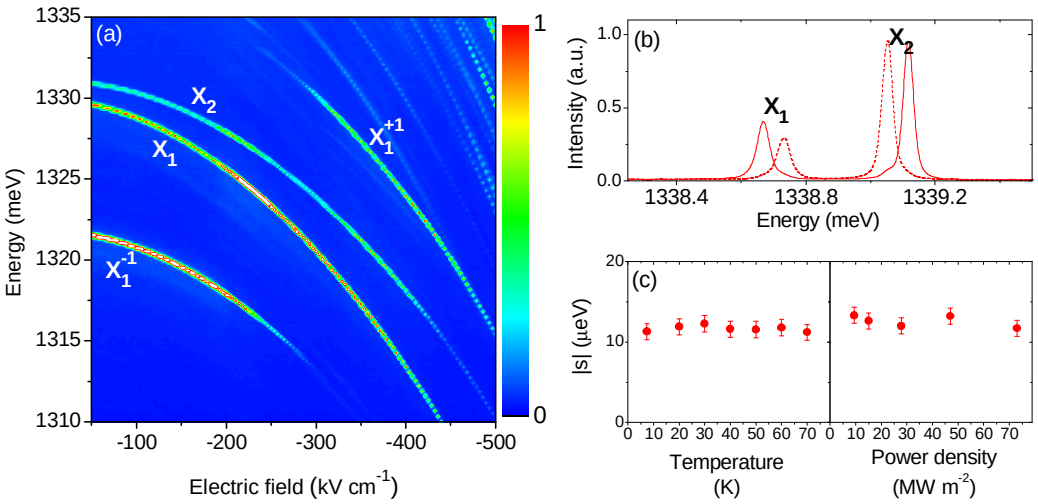

Figure 4.1: Photoluminescence (PL) measurements from a typical QD, emission lines are labeled according to the initial state of the corresponding transition. (a)Unpolarised PL as a function of electric field. (b)Polarised PL spectra showing emission from the neutral transitions, solid (dashed) line shows the emission via the $|X_1^\beta\rangle$ ($|X_1^\alpha\rangle$) state. (c) Magnitude of fine-structure splitting ($|s|$), at fixed electric field, as a function of temperature (left pane) and excitation power (right pane).

and holes. At lower field magnitudes the $|X_1^{-1}\rangle$ state is preferentially created due to an excess of electrons in the QD; whilst at higher field magnitudes an excess of holes preferentially populates the $|X_1^{+1}\rangle$ state. There exists a narrow range of fields where both transitions from the charged states can be observed. In this range, the intensity of the neutral transitions relative to that of the charged transitions is greatest as expected.

Suitable QDs are identified by examining the PL emission from each aperture. Spectral lines due to the different transitions are identified with certainty using a variety of techniques, such as analysis of the emission intensity as a function of excitation power and electric field magnitude. Example spectra showing typical emission from the neutral biexciton cascade are shown in figure 4.1b, with the effects of a relatively large $\sim 60\mu$eV FSS clearly visible. The relative intensities of the $|X_2\rangle \rightarrow |X_1\rangle$ and $|X_1\rangle \rightarrow |0\rangle$ transitions depend on the power of the excitation laser. However, the FSS is remarkably robust to changes in both the excitation power and temperature as shown in figure 4.1c.

4.3 Manipulation of fine-structure with electric field

Application of a vertical electric field, F, induces a Stark shift in the energy levels of the QDs of the form

$$E = E_0 - pF + \beta F^2 \tag{4.1}$$

where E_0 is the energy when $F = 0$, p is the permanent dipole moment in the z direction, and β is the polarisability. The values of these parameters are different for each transition and each QD.

The $|X_1^{\alpha}\rangle$ and $|X_1^{\beta}\rangle$ neutral exciton eigenstates undergo a Stark shift at different rates, and thus the FSS is varied as the electric field is changed.

The magnitude of the FSS is given by

$$|s| = |E_\alpha - E_\beta| = |\Delta E_{\alpha-\beta} - F(p_\alpha - p_\beta) + F^2(\beta_\alpha - \beta_\beta)| \tag{4.2}$$

where subscripts on E, p, and β indicate the energy, dipole moment in the z direction, and polarisability, respectively, of the corresponding $|X_1^{\alpha,\beta}\rangle$ states; and $\Delta E_{\alpha-\beta}$ is the magnitude of the energy difference between the two states in the absence of an applied electric field, such that $\Delta E_{\alpha-\beta} = |E_{0,\alpha} - E_{0,\beta}|$.

4.3.1 Measurement of FSS as a function of electric field

The effects of the electric field on the FSS are measured via the acquisition of two sets of orthogonally polarised spectra taken at a range of electric fields. For each set of spectra, the experimental set up shown in figure 3.4b in section 3.3.1 is used to allow polarised PL spectroscopy. The emission from one decay path is selected by fixing the orientation of HWP1, and a series of PL spectra are recorded at a range of electric fields via incrementally varying the applied bias voltage to the device. The correct orientation of HWP1 is determined via a measurement of θ_0 using the method detailed in section 3.4. The process is then repeated with the angle of HWP1 adjusted to select emission from the other decay path.

Each set of spectra is analysed, and the emission energy of each of the $|X_2\rangle \rightarrow |X_1\rangle$ and $|X_1\rangle \rightarrow |0\rangle$ transitions is extracted by fitting Lorentzian peaks to the corresponding emission lines. The difference in energy between corresponding transitions in the two orthogonally polarised data sets is $|s|$, and thus the variation in FSS as a function of electric field is obtained. Figure 4.2 shows the fitted emission energy, along with the extracted FSS, as a function of electric field for an example QD. Note that this method is only suitable for $|s|$ larger than $\sim 10\mu$eV, as for smaller values of FSS the resolution of the system is too large to allow accurate measurements. Also, when the system is near the anticrossing θ_0 rotates and so the fixed orientation of HWP1 will no longer select emission from just one decay path. However, this method is significantly faster than the technique in section 3.4

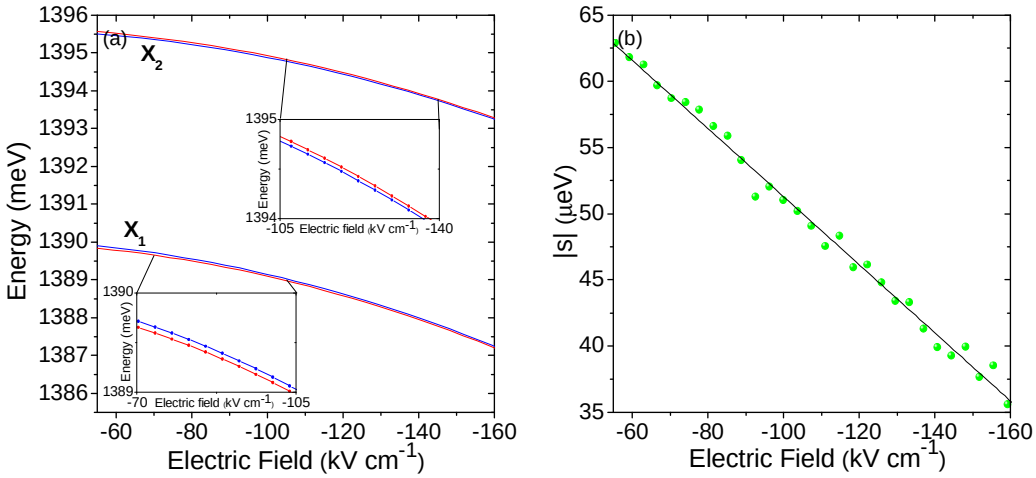

Figure 4.2: Measurement of FSS shift via orthogonally polarised data sets. (a) Emission energy of the neutral transitions, as a function of electric field, for both decay paths. (b) FSS as a function of electric field.

and, whilst not appropriate for measuring small values of FSS or the rotation of θ_0, it is well suited for measuring the large scale changes in $|s|$ over a wide variation in electric field.

4.3.2 FSS tuning rate

Away from the minimum value, s_0, the magnitude of the FSS exhibits a linear change with electric field, with a gradient labeled γ. By inspection of equation 4.2 it can be seen that this implies $\beta_\alpha = \beta_\beta$ and that γ is governed by the difference in the permanent z dipole moment of the two exciton eigenstates, such that $\gamma = p_\alpha - p_\beta$.

This behaviour can be explained by considering the origin of both the Stark shift parameters, which have been investigated by a number of theoretical studies such as [18, 42, 43]. Due to QD shape, built-in strain field, and Indium composition distribution, confined electrons are localised with a different mean z-position to that of confined holes. This leads to a permanent z dipole moment (p), which is proportional to the overlap integral between the electron and hole wavefunctions[44]. In-plane anisotropy of the QD confinement potential causes the spatial distribution of the confined wavefunc-

tions to be dependent on their orientation within the QD. This results in the overlap integral between confined electron and holes being dependent on the orientation of the exciton wavefunction. Thus the two orthogonally orientated exciton eigenstates have different values of p, as observed. The polarisability of the eigenstate wavefunction is not strongly affected by the in-plane anisotropy as it is influenced mainly by the height of the confinement potential, which is the same for both eigenstates[45].

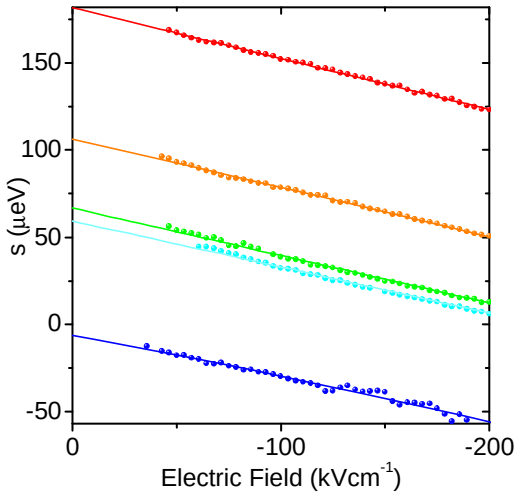

Figure 4.3: FSS, s, as a function of electric field for five QDs from wafer W0194. The FSS varies linearly, and although s is different for each QD the rate of change of s with respect to electric field is the same.

Due to the random nature of the growth process most QD parameters, such as the FSS at zero electric field, neutral transition emission energy, energy difference between the two neutral transitions, and the Stark shift coefficients (p, β), are typically different for each QD. However, the value of γ is observed to be similar for QDs in a given wafer and independent of the other parameters given above. This indicates that the in-plane anisotropy is dependent on the MBE conditions during the growth of the QDs, and suggests that γ may be influenced by engineering different QD shape and strain field via modification of these conditions.

Figure 4.3 shows the FSS as a function of electric field for several QDs from a particular wafer, labeled W0194, in which the QDs were grown to

have emission from the neutral transitions at around 940 nm. For these QDs $\gamma = -0.285 \pm 0.019$ μeV kV^{-1} cm. Shifts in the FSS on the order of 100μeV have been achieved using changes in electric field of $\sim$ 500 kV cm^{-1} for QDs in this wafer.

4.3.3 Effects of QD growth conditions on FSS tuning rate

The effects of different growth conditions on the rate of tuning of the FSS has been qualitatively demonstrated via a study of QDs grown to have different structural and optical properties. This has been achieved by studying QDs in two other wafers, labeled W0462 and W0590. Wafer W0462 contains QDs which are grown to have emission from neutral transitions around 880 nm. To achieve the desired reduction in emission wavelength these QDs are grown smaller than those in wafer W0194 by reducing the time for which the QD material is deposited. This decreases the confinement lengthscale leading to a larger separation between energy levels and thus transitions between states emit photons with shorter wavelength. In addition, the smaller size of these QDs leads to an alteration in the in-plane anisotropy. Wafer W0590 has the same p-i-n wafer structure as the other wafers, but the QD layer is embedded inside a layer of $Al_{0.3}Ga_{0.7}As$ instead of GaAs. The increased lattice mismatch between AlGaAs and InAs leads to an increase in the inter-layer strain, resulting in an alteration of the strain field anisotropy. Thus, both these variations in the growth conditions should affect the rate at which the FSS is tuned by altering the difference between the permanent z dipole moments of the two eigenstates.

Figure 4.4 shows $|s|$ as a function of electric field for QDs in these two wafers. The QDs in wafer W0462 have $\gamma = -0.198 \pm 0.024$ μeV kV^{-1} cm, with the FSS of these QDs varying more slowly with electric field than those in wafer W0194. The QDs in wafer W0590 have $\gamma = -0.306 \pm 0.035$ μeV kV^{-1} cm, and therefore the rate at which the FSS changes with electric field is greater than that for QDs in wafer W0194. These results are consistent with the hypothesis that the difference between p_α and p_β, which

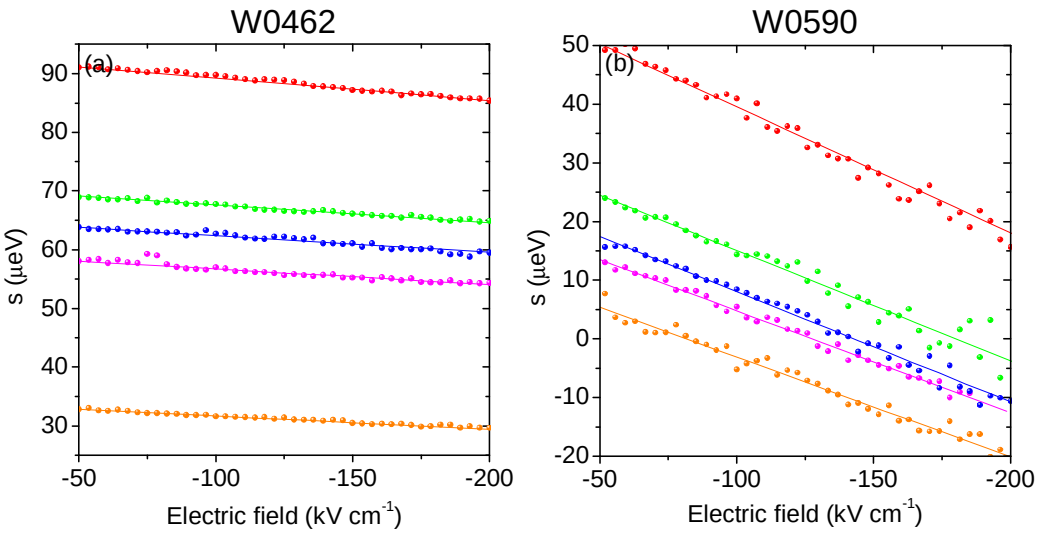

Figure 4.4: FSS as a function of electric field for QDs in two different wafers. (a)-(b) FSS as a function of electric field for QDs in wafers W0462 (left) and W0590 (right), both graphs are plotted with the same y-axis scale to allow direct comparison of the tuning gradients.

is dependent on the in-plane anisotropy of the electron and hole wavefunctions, is responsible for the rate at which FSS is varied by changes in electric field. It also demonstrates that this parameter can be manipulated via careful selection of the QD growth conditions. However, more work is needed to explore the quantitative relationship between the factors affecting the anisotropy and their effects on γ. The remaining results presented in this chapter are obtained from QDs in wafer W0194.

4.4 Coupling of the exciton states

As the method presented in this work allows the FSS to be tuned over such a large range, the sign of the FSS can be inverted for many of the QDs studied. Using the method discussed in section 3.4 it is possible to accurately measure to $|s| \sim 1\mu$eV. This allows detailed study of the FSS as its sign is inverted, as well as investigation of the polarisation orientation (θ_0) when $|s| \sim s_0$[41].

In contrast with previous work, in which the two neutral exciton eigen-

states are independent and the FSS is observed to cross through zero[32, 34, 35, 36, 37], when the eigenstates are tuned close to each other an anticrossing is observed. This results in a minimum value, s_0, below which the FSS can not be reduced. The value of s_0, and the electric field at which it occurs, F_0, are different for each QD. In addition, the orientation of the axes of linear polarisation, θ_0, of the photons emitted from the two neutral biexciton decay paths exhibits a rotation of $\sim 90°$ as the system traverses the anticrossing. Figure 4.5 shows $|s|$ and θ_0 as a function of electric field in the region of the anticrossing for three QDs.

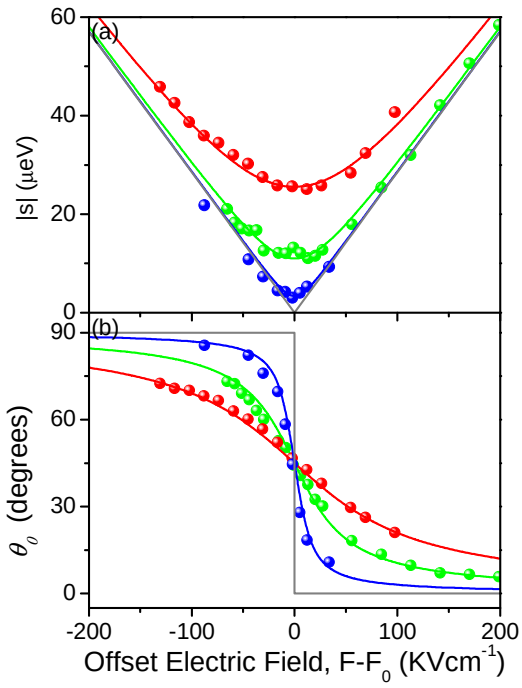

Figure 4.5: FSS and orientation of the polarisation axes as a function of electric field. (a)-(b) Magnitude of FSS ($|s|$) and orientation of the linear polarisation basis (θ_0) as a function of electric field for three QDs with s_0 of 25.5 μeV (red), 12.0 μeV (green), and 3.0 μeV (blue). Note that the electric field has been offset by F_0 to aid comparison. Grey lines indicated the expected results for the case of $s_0 = 0$. Solid coloured lines are fits to the data using the model detailed below.

Far from the anticrossing $|s|$ varies linearly with F, as discussed in the section above. Also, the polarisation axes are aligned with the [110] and

$[1\bar{1}0]$ crystalline directions such that θ_0 is 0° for one decay path and 90° for the other. Note that which decay path results in emission with polarisation aligned to the [110] direction, and thus the sign of s, depends which side of the anticrossing the system is measured.

4.4.1 Coherent coupling model

The observed behaviour is well described by a coherent coupling model of the same form as that used to describe coupled harmonic oscillators[46], strong light-matter coupling[47], and anticrossings in the states of molecular systems[48]. The Schrödinger equation for the system has the form

$$E\begin{pmatrix}\alpha\\ \beta\end{pmatrix} = \begin{pmatrix}E_\alpha & s_0/2\\ s_0/2 & E_\alpha - \gamma(F-F_0)\end{pmatrix}\begin{pmatrix}\alpha\\ \beta\end{pmatrix} \tag{4.3}$$

where the state vector (α, β) gives the components of the two basis states such that the state of the system is given by

$$\Psi(F) = \alpha|X_1^\alpha\rangle + \beta|X_1^\beta\rangle. \tag{4.4}$$

The eigenstates of the system are the symmetric and antisymmetric coherent superposition states

$$\begin{aligned}\Psi^+ &= \cos\theta_0|X_1^\alpha\rangle + \sin\theta_0|X_1^\beta\rangle\\ \Psi^- &= \sin\theta_0|X_1^\alpha\rangle - \cos\theta_0|X_1^\beta\rangle\end{aligned} \tag{4.5}$$

which have corresponding energy eigenvalues, $E_\pm$, and θ_0 given by

$$E_\pm = E_\alpha - \frac{\gamma(F-F_0)}{2} \pm \frac{1}{2}\sqrt{\gamma^2(F-F_0)^2 + s_0^2} \tag{4.6}$$

$$\theta_0 = \pm\tan^{-1}\left[\frac{s_0}{\gamma(F-F_0) \pm (E_- - E_+)}\right] \tag{4.7}$$

Finally, $|s|$ is calculated from the difference between the two energy eigen-

values to yield

$$|s| = \sqrt{\gamma^2 \left(F - F_0\right)^2 + s_0^2}. \tag{4.8}$$

Fits to the experimental data using equations 4.8 and 4.7 show good agreement and are shown in figure 4.5 as solid coloured lines. This model has two degenerate solutions for the evolution of θ_0 with varying electric field, with both clockwise and anticlockwise rotation possible.

4.4.2 Anticrossing ensemble

Data from an investigation into the anticrossings of an ensemble of 22 QDs is shown in figure 4.6. Figure 4.6a shows θ_0 at $|s| \gg s_0$ for the ensemble, this is extracted from fitting equation 4.7 to the data. The tendency for the polarisation basis to be aligned with the [110] crystalline axis is clear and is independent of the value of s_0. The source of the scatter is not known, however it is likely due to variations in QD shape or local fields around the QDs caused by imperfections in the semiconductor environment. It should be noted that this alignment has previously been observed[49] in InAs QDs grown in a single deposition and immediately overgrown in GaAs, as used in this work. However, it is not seen in reports on QDs grown using the "partially capped island" technique[50].

In the model detailed above clockwise and anticlockwise rotation of θ_0, as the anticrossing is traversed, are degenerate. However, in practice each QD is only ever seen to have rotation in one direction. Of the QDs studied in this work, 9 showed rotation in one direction and 13 in the other which is consistent with the ensemble having no preferred direction of rotation. The cause of the direction of preference for individual QDs is not known, but could be due to local defects or fields in the semiconductor environment near to each QD.

The strength of the coupling between the exciton is defined by s_0. In order to identify factors which affect the coupling, the relationship between s_0 and several other QD parameters has been investigated, including the binding energy, defined as the mean difference in energy between the $|X_1\rangle \rightarrow$

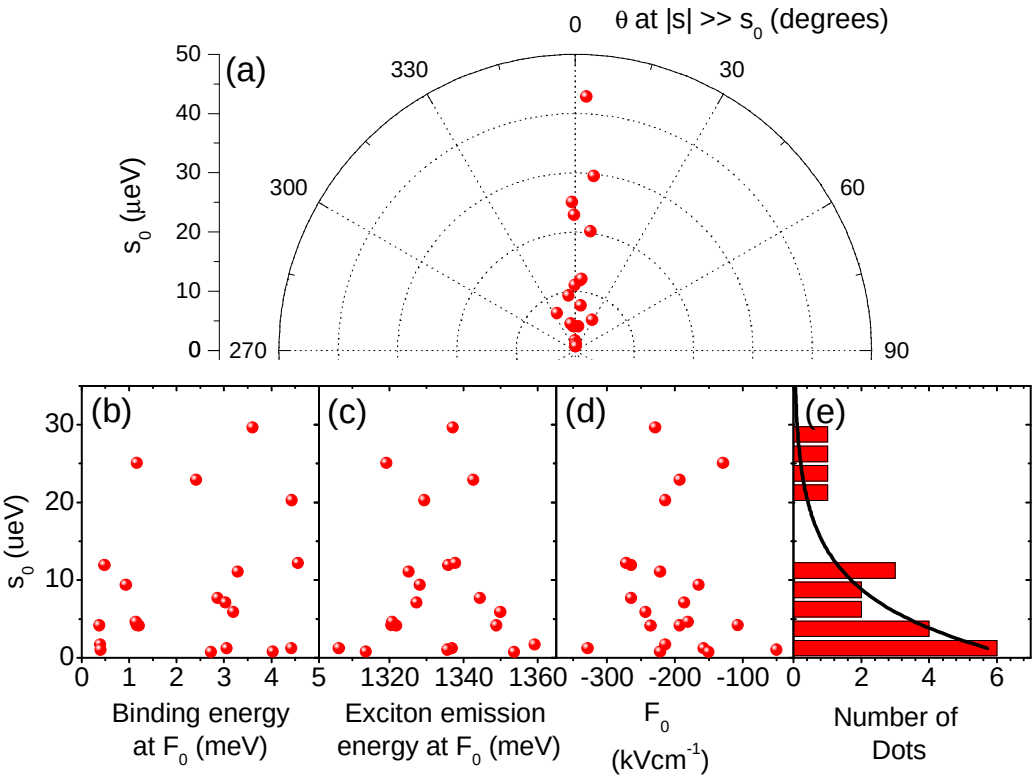

Figure 4.6: QD ensemble study. (a) Orientation of the eigenstates, θ_0, far from the anticrossing as a function of s_0. (b),(c) s_0 as a function of binding energy and exciton emission energy at the anticrossing. (d) s_0 as a function of the electric field at the anticrossing, F_0. (e) histogram of s_0 for the ensemble.

$|0\rangle$ and $|X_2\rangle \rightarrow |X_1\rangle$ transition, at F_0 (figure 4.6b); the exciton emission energy, defined as the mean energy of the $|X_1\rangle \rightarrow |0\rangle$ transition, at F_0 (figure 4.6c); and the value of electric field needed to minimise the FSS, F_0 (figure 4.6d). Any relationship linking these parameters is not significant relative to the scatter of the values throughout the ensemble. Note that the apparent structure of the points in their distribution along the x-axis is an artifact of the range of emission energy and the spread of $|s|$ for different QDs. Only those QDs which emit from the neutral transitions with wavelengths between $\sim$ 930-945 nm were studied, as this corresponds with the cavity mode of the planar structure. In addition, the anticrossing can not be observed in all QDs, as emission from those with a large value of $|s|$ at zero electric field is quenched before the minimum is reached. Variation of the MBE growth conditions during QD deposition can create samples with a lower mean $|s|$ at zero electric field, as seen in [49]. Such a sample would allow the anticrossing to be observed in a larger proportion of the QDs.

Figure 4.6e shows a histogram of s_0 for the ensemble, the data is fit with an exponential function as a guide however more data points are required to confirm the distribution. Small values of s_0 are more common than large values and several of the QDs have $s_0 < 1\mu$eV, which is below the smallest linewidths that have been reported in similar QDs[51] making this work attractive for the production of entangled photon pairs.

4.5 Entangled photon pair emission

Entangled photon pairs have been observed from a QD which, in the absence of an applied electric field, has $|s| > 50\mu$eV [41]. This magnitude of FSS is too large for entanglement between the two neutral biexciton cascade photons to be observed (see section 2.8). However, with the application of $F_0 = -240$ kV cm^{-1} the FSS is minimised to $s_0 = 1.4\mu$eV, which is well below that required to observe entangled photon pair emission[52, 53, 54] with standard APDs. In this section an analysis of second-order pair correlation measurements recorded by Anthony Bennett and Mark Stevenson, in

which the two photons from the neutral biexciton cascade are observed to be entangled, is presented.

4.5.1 Measurement of entanglement

Second-order pair correlation measurements are used to observe entanglement between the two photons emitted by the neutral biexciton cascade. Recall from section 3.3.5 that the second-order pair correlation function

$$g^{(2)}_{P1,P2}(\tau) = \frac{\langle I_1(t) I_2(t+\tau)\rangle}{\langle I_1(t)\rangle\langle I_2(t+\tau)\rangle}, \tag{4.9}$$

is proportional to the probability that the resulting two-photon state is $|P1\ P2\rangle$. For example, $g^{(2)}_{\alpha,\alpha}(\tau)$ is proportional to the probability that the photons emitted by the neutral biexciton cascade are in state $|\alpha\alpha\rangle$, corresponding to the transitions $|X_2\rangle \rightarrow |X_1^{\alpha}\rangle \rightarrow |0\rangle$.

Measurement of entanglement between the two photons is made using three pairs of co- and cross-polarised second-order pair correlation functions: One in the linear basis parallel to the orientation of the eigenstates, $\{\alpha, \beta\}$; one in the linear basis at 45° to the eigenstates, labeled $\{\alpha_{45}, \beta_{45}\}$; and one in the left and right circularly polarised basis, labeled as $\{L, R\}$.

The use of such measurements to observe entanglement can be understood by considering the expected results of the second-order pair correlations in the three bases. Consider the two-photon wavefunction in the idealised case of $|s| = 0$, as seen in equation 2.17. This is the maximally entangled Bell state given by

$$|\Psi^+\rangle = \frac{1}{\sqrt{2}}\left(|\alpha\alpha\rangle + |\beta\beta\rangle\right), \tag{4.10}$$

which can be expressed in each of the three polarisation bases as

$$|\Psi^+\rangle = \frac{1}{\sqrt{2}}\left(|\alpha\alpha\rangle + |\beta\beta\rangle\right) = \frac{1}{\sqrt{2}}\left(|\alpha_{45}\alpha_{45}\rangle + |\beta_{45}\beta_{45}\rangle\right) = \frac{1}{\sqrt{2}}\left(|RL\rangle + |LR\rangle\right). \tag{4.11}$$

Second-order pair correlation measurements of this wavefunction will show that co-polarised photon pairs are emitted in the $\{\alpha, \beta\}$ and $\{\alpha_{45}, \beta_{45}\}$ bases.

Thus, for values of τ corresponding to both photons being emitted from the same cascade event, peaks are expected in $g^{(2)}_{\alpha,\alpha}(\tau)$ and $g^{(2)}_{\alpha_{45},\alpha_{45}}(\tau)$ but not in $g^{(2)}_{\alpha,\beta}(\tau)$ or $g^{(2)}_{\alpha_{45},\beta_{45}}(\tau)$. The measurements in the $\{L, R\}$ basis will show cross-polarised photon pairs are emitted, and thus $g^{(2)}_{R,L}(\tau)$ will show a peak which is not present in $g^{(2)}_{R,R}(\tau)$.

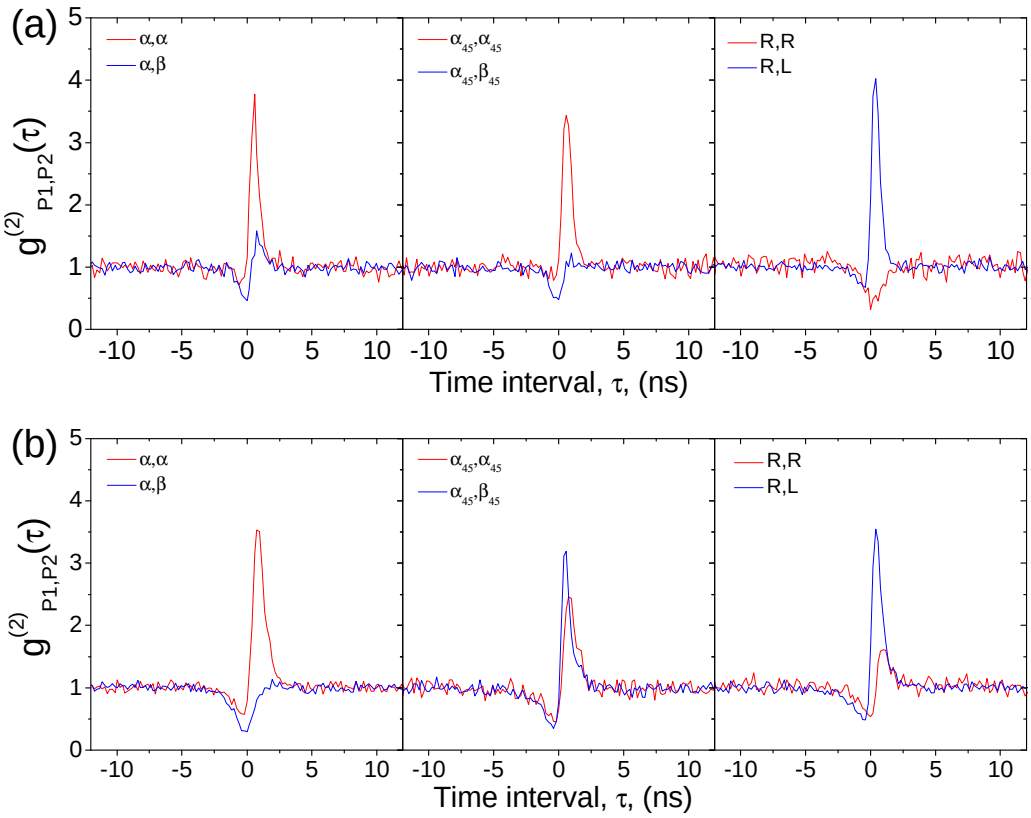

Figure 4.7: Second-order pair correlations for the same QD when $|s| = 1.5\mu$eV (a) and when $|s| = 10\mu$eV (b). This is achieved by varying the vertical electric field as described in the main text. Red (blue) lines show co-polarised (cross-polarised) measurements. The legends indicate the polarisation $(P1, P2)$ of the photons used to trigger the state and stop inputs. The data has been normalised to the average value of $g^{(2)}_{P1,P2}(\tau)$ for $|\tau| \gg 0$ for clarity.

Contrast this with the case of a QD with very large $|s|$ which, as explained in section 2.8, appears to emit classically correlated photon pairs. The two-photon wavefunction of the photon pairs emitted from such a QD have equal

probability of being detected in state $|\alpha\alpha\rangle$ or $|\beta\beta\rangle$, which expressed in terms of the other polarisation bases gives the following:

$$\begin{aligned}
|\alpha\alpha\rangle &= \tfrac{1}{2}\left(|\alpha_{45}\alpha_{45}\rangle + |\alpha_{45}\beta_{45}\rangle + |\beta_{45}\alpha_{45}\rangle + |\beta_{45}\beta_{45}\rangle\right) \\
|\alpha\alpha\rangle &= \tfrac{1}{2}\left(|RR\rangle + |RL\rangle + |LR\rangle + |LL\rangle\right) \\
|\beta\beta\rangle &= \tfrac{1}{2}\left(|\beta_{45}\alpha_{45}\rangle - |\alpha_{45}\beta_{45}\rangle - |\beta_{45}\alpha_{45}\rangle + |\beta_{45}\beta_{45}\rangle\right) \\
|\beta\beta\rangle &= \tfrac{1}{2}\left(-|RR\rangle + |RL\rangle + |LR\rangle - |LL\rangle\right).
\end{aligned} \tag{4.12}$$

Second-order pair correlation measurements of these wavefunctions will yield very different results to those of the entangled case. Measurements in the $\{\alpha, \beta\}$ basis will detect co-polarised photon pairs as in the case of the entangled wavefunction. However, measurements in the $\{\alpha_{45}, \beta_{45}\}$ and $\{R, L\}$ bases will show a statistical mix of both co- and cross-polarised pairs, with peaks observed in in all four of the correlations.

Figures 4.7a and 4.7b show the second-order pair correlation measurements for the QD when $|s| = s_0 = 1.4\mu$eV and when $|s| = 10\mu$eV, respectively. This is achieved by varying the electric field. For the case of $|s| = 1.4\mu$eV there is an increased probability of detecting co-polarised photons and a reduced probability of detecting cross-polarised photons in both the linear bases, whilst the opposite is true in the circular basis. This is the expected result from equation 4.11. However, when $|s|$ is increased to the larger value of $|s| = 10\mu$eV the entanglement can no longer be resolved by the temporal resolution of the detectors and the system appears to emit classically correlated photon pairs, which are better described by equation 4.12.

4.5.2 Fidelity of entanglement

The fidelity of the emitted two-photon state to the Bell state given in equation 4.11 can be quantitatively assessed using the degree of polarisation correlation, denoted $C_{\{\alpha,\beta\}}$, $C_{\{\alpha_{45},\beta_{45}\}}$, and $C_{\{R,L\}}$ for each of the three polarisation bases described above. The degree of polarisation correlation ranges from -1 to 1 and quantifies the probability of the neutral biexciton cascade emitting

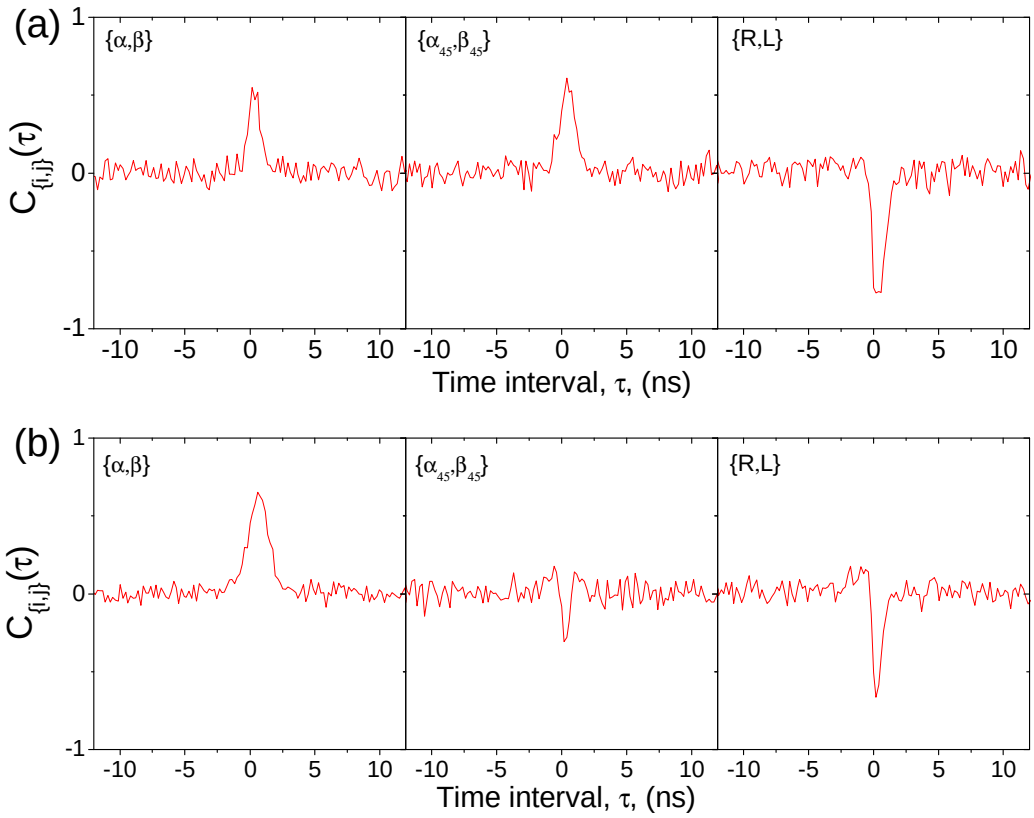

Figure 4.8: Degree of polarisation correlation in the three polarisation bases used to asses the entanglement of photon pairs emitted by the neutral biexciton cascade. (a) Data for when $|s| = 1.4\mu$eV. (b) Data for when $|s| = 10\mu$eV.

either co- or cross-polarised photon pairs. A value of $C_{\{i,j\}} = 0$ corresponds to the polarisation of the two photons being completely uncorrelated, as would be the case if the polarisation of each of the photons was random and independent. Negative values of $C_{\{i,j\}}$ correspond to an increased probability of cross-polarised emission, with $C_{\{i,j\}} = -1$ corresponding to the two photons always being cross-polarised. For positive values of $C_{\{i,j\}}$, there is an increased probability of the two photons being co-polarised, with $C_{\{i,j\}} = +1$ indicating that the emission is always co-polarised.

The degree of polarisation correlation in a given polarisation basis is calculated from the corresponding pair of second-order pair correlation mea-

surements, and is given by

$$C_{\{i,j\}} = \frac{g^2_{i,i}(\tau) - g^2_{i,j}(\tau)}{g^2_{i,i}(\tau) + g^2_{i,j}(\tau)} \tag{4.13}$$

Where $g^2_{i,i}(\tau)$ is the co-polarised pair correlation measurement and $g^2_{i,j}(\tau)$ is the cross-polarised pair correlation measurement. The degree of polarisation correlation calculated from the pair correlations presented above is shown for the three basis states in figure 4.8.

As can be seen from equation 4.11, the ideal entangled state has $C_{\{\alpha,\beta\}} = C_{\{\alpha_{45},\beta_{45}\}} = 1$ and $C_{\{R,L\}} = -1$. As discussed in [54], the fidelity to the Bell state given by equation 2.17 is

$$f^+ = \frac{1}{4}\left(C_{\{\alpha,\beta\}} + C_{\{\alpha_{45},\beta_{45}\}} - C_{\{R,L\}} + 1\right) \tag{4.14}$$

with uncorrelated emission resulting in $f^+ = 0.25$ and polarisation correlated pairs, as described by equation 4.12, yielding $f^+ = 0.5$. Values of f^+ above 0.5 indicate entanglement between the two photons.

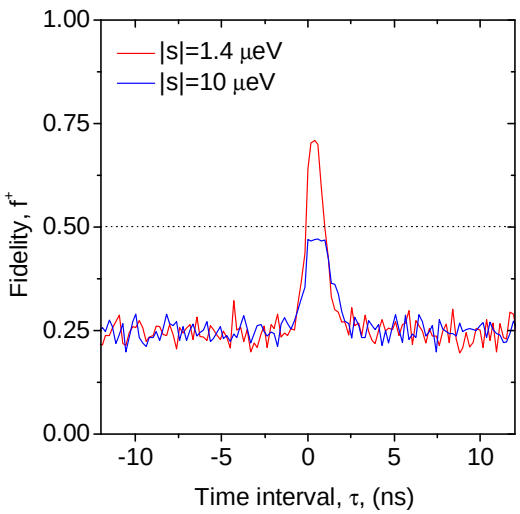

Figure 4.9: Fidelity of the emitted state to the Bell state $|\Psi^+\rangle$ for a QD tuned to two different values of $|s|$ as indicated in the legend. The classical threshold is indicated with a dashed horizontal line.

Figure 4.9 shows the fidelity of the emitted two-photon state as a function of the two values of $|s|$. When $|s| = 1.4\mu$eV the fidelity is significantly larger than 0.5, clearly showing entanglement between the photons. However, when $|s| = 10\mu$eV the fidelity drops to under 0.5, as the entanglement can no longer be detected.

4.6 Conclusion

A vertical electric field has been used to tune the fine structure splitting of QDs in diode devices fabricated from three different wafers, allowing $|s|$ to be tuned over a wide range on the order of 100μeV. The rate of the shift in $|s|$ has been observed to be linear, with all QDs in a given wafer shifting at a similar rate. Furthermore, it has been qualitatively shown that the rate of the shift can be manipulated via alteration of the conditions during MBE growth.

When the sign of s is inverted, the two exciton eigenstates are observed to go through an anticrossing. This behaviour is well described by a simple coherent coupling model. The coherent coupling of the eigenstates imposes a minimum $|s| = s_0$, below which the magnitude of the FSS can not be reduced. In addition, hybridization of the exciton states induces rotation in the orientation of the eigenstates, which is manifested by a corresponding rotation in the axes of linear polarisation of the photons emitted from the neutral biexciton cascade. Entangled pair emission has been observed from a QD with $s_0 = 1.4\mu$eV and control of the fidelity demonstrated.

Possible extensions to this work include conducting a detailed study of the effects of the MBE growth conditions on the tuning rate of $|s|$ or investigating the origin of the coupling between the eigenstates and the factors which influence the value of s_0.

Chapter 5

Control of the neutral exciton fine-structure via simultaneous application of electric and magnetic fields

5.1 Introduction

The effects of magnetic field on the neutral exciton states in single QDs have been the subject of much research[33, 15, 32]. As discussed in section 2.8, it is desirable to be able to reduce the fine-structure splitting (FSS, s) of the exciton state ($|X_1\rangle$). It has been shown that the application of a magnetic field can be used to tune the value of the FSS, allowing a reduction in $|s|$. For example, in references [32, 33] a magnetic field applied in the plane of the sample, perpendicular to the growth direction, is used to vary the FSS via manipulation of the coupling between the bright (m=±1) and dark (m=±2) exciton states. Thus the application of a magnetic field offers the potential of an additional tuning mechanism which can be used in conjunction with the vertical electric field method detailed in chapter 4.

Recall that although the application of vertical electric field allows a very large tuning range, coherent coupling between the two exciton eigenstates

imposes a minimum value, s_0, below which the FSS can not be reduced. However, recent experimental and theoretical work has explored the possibility of reducing s_0 via the use of two independent tuning mechanisms simultaneously[55, 56]. It has been proposed that the application of two orthogonal strain fields[55] can reduce s_0 to below 0.1μeV in typical InGaAs/GaAs QDs. Of particular relevance to the work presented in this chapter is that of Trotta *et al.*[56], who tune the FSS of single QDs using the simultaneous application of a vertical electric field and manipulation of the strain field in the plane of the QDs. These two tuning mechanisms allow them not only to vary $|s|$, but also to vary s_0. Consequently, they are able to eliminate the FSS entirely from all QDs in their study. However, using their method it is only possible to eliminate the FSS at one unique combination of electric and strain fields; thus the range of emission energies over which there is a high degree of entanglement between the emitted photon pairs is severely restricted. The work presented in this chapter overcomes this limitation, via the use of a tuning mechanism which allows the energy of emission at the point of maximum entanglement to be varied over a wide range.

In this chapter the effects on the FSS of simultaneous application of a magnetic field in conjunction with a vertical electric field are investigated. Firstly, the known effects of magnetic field on the energy splitting of the neutral exciton states are introduced and discussed. Two different magnetic field orientations are considered: Faraday geometry, where the field is orientated parallel with the sample growth direction; and Voigt geometry, where the field is orientated perpendicular to the growth direction. Measurements in each of these geometries are then presented. Faraday geometry is used to investigate the effects of electric field on the Zeeman splitting between the two exciton eigenstates ($|X_1^{\alpha,\beta}\rangle$). Voigt geometry measurements, in which the FSS is tuned by simultaneous application of both an electric and magnetic field, are then presented and discussed. Finally, a scheme for the emission of wavelength-tunable entangled photon pairs is proposed.

5.2 Fine-structure of the neutral exciton states in magnetic field

The effects of magnetic field on the neutral exciton states are investigated using the same diode devices as studied in the previous chapter, details of which can be found in section 3.2.1. In order to apply a magnetic field the devices are mounted in a cryostat which is inserted into the bore of a superconducting magnet. The bore allows optical access to the samples and thus the devices can be studied using the techniques described in chapter 3.

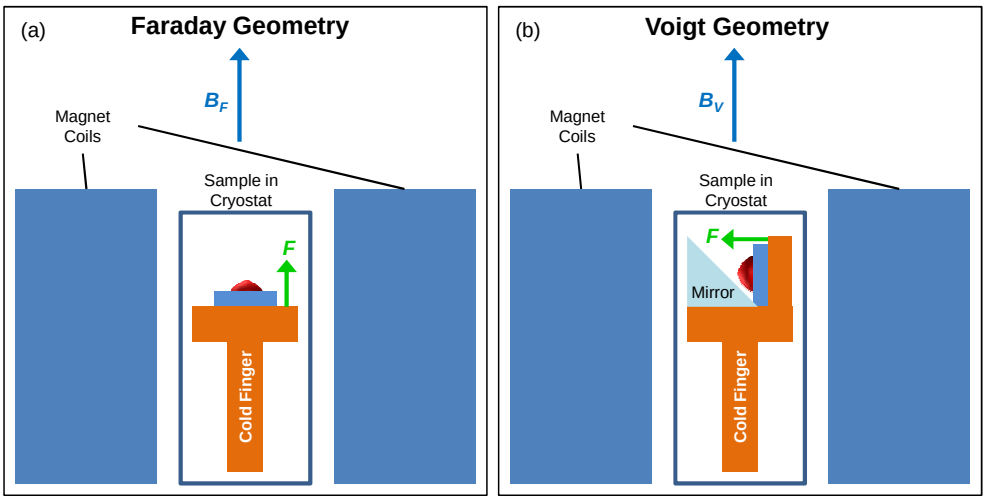

Figure 5.1: Geometry of Faraday and Voigt configurations. In both configurations optical access is achieved down the axis of the magnet bore. The orientation of the magnetic field, B_F or B_V, is indicated with a blue arrow and that of the electric field, F, is shown with a green arrow.

Two different magnetic field orientations have been studied by changing the cold finger on which the sample is mounted. A magnetic field parallel with the growth direction is applied by mounting the sample horizontally on a standard flat cold finger, this configuration is known as Faraday geometry and is shown in figure 5.1a. To apply a magnetic field perpendicular to the growth direction the sample is mounted vertically on a modified cold finger as shown in figure 5.1b, this configuration is known as Voigt geometry. When mounted in the Voigt configuration a 45° mirror is placed on the modified

cold finger in order to allow optical access to the sample surface.

In the Faraday configuration the electric and magnetic fields are parallel with each other and the optical axis. In the Voigt configuration the sample is rotated by 90° so that the electric and magnetic fields are perpendicular to each other. Thus the electric field remains parallel with the optical axis, however the magnetic field is perpendicular to the optical axis.

The behaviour of the exciton states is different for each of the two magnetic field orientations. A detailed analysis of the effects of both orientations of magnetic field on the neutral and charged exciton states of single QDs can be found in [15]. However, a brief overview of the effects on the bright exciton states of relevance to the work in this thesis is included in this section.

5.2.1 Faraday geometry

A Faraday geometry magnetic field, B_F, both alters the energy levels of the neutral exciton states and induces hybridization of the bright states. This hybridization causes photons emitted by transitions involving the neutral states to have circular polarisation. The Zeeman splitting between the two eigenstates results in an increase in the energy difference between the two exciton eigenstates. This leads to an energy splitting in the circular basis, $s_{\{R,L\}}$, which sums in quadrature with the FSS at zero magnetic field. The total energy splitting between the two neutral eigenstates in a Faraday field is given by

$$s\left(B_F\right) = \sqrt{s\left(0\right)^2 + \left(g_X^{\perp}\mu_B B_F\right)^2} = \sqrt{s_{\{\alpha,\beta\}}^2 + s_{\{R,L\}}^2}, \tag{5.1}$$

where $s\left(0\right) \equiv s_{\{\alpha,\beta\}}$ is the FSS in the absence of a magnetic field, which is the splitting in the linear eigenstate basis as described in section 2.6.2; $g_X^{\perp}$ is the component of the effective exciton g-factor which is parallel to the magnetic field. Where the effective exciton g-factor is given by the sum of the g-factors of the constituent electron and hole such that $|g_X| = |g_e| + |g_h|$; μ_B is the Bohr magneton; and $g_X^{\perp}\mu_B B_F \equiv s_{\{R,L\}}$ is the splitting in the circular basis due to the magnetic field.

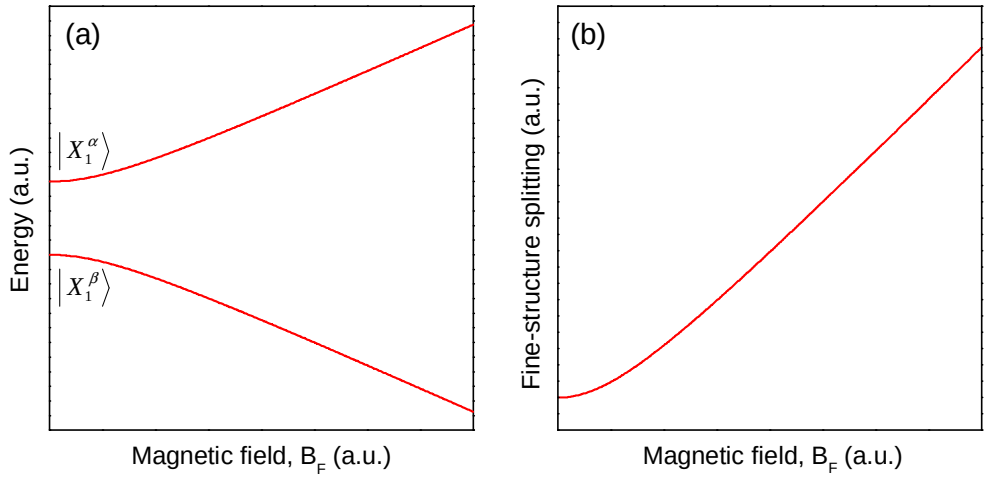

Figure 5.2: Effects of a Faraday magnetic field. (a) Energy of the neutral exciton states as a function of Faraday field magnitude. (b) Energy splitting between the neutral states as a function of Faraday field magnitude.

Figure 5.2 shows the typical behaviour of the neutral exciton energy levels, and the energy difference between them, as a function of an applied Faraday field. As can be seen by inspection of equation 5.1, the FSS is initially proportional to B_F^2 for small B_F, however at larger fields where $s_{\{\alpha,\beta\}} \ll s_{\{R,L\}}$ the FSS increases linearly with B_F with a gradient of $|g_X^\perp|\mu_B$.

Note that the extra circular component of the splitting due to a Faraday field serves only to increase the total FSS. Therefore, Faraday geometry is not appropriate for further study of the anticrossings presented in section 4.4 or for tuning the FSS to allow the observation of entangled photon pairs. However, measurements in this geometry are still of interest for fully characterising the behaviour of the neutral states under the application of simultaneous electric and magnetic fields.

5.2.2 Voigt geometry

A Voigt geometry magnetic field does not induce hybridization of the bright states and so preserves the linear polarisation of photons emitted from the neutral transitions. In this geometry, the magnetic field causes hybridization

between the bright and dark states, which has two interesting effects. Transitions involving the dark states are able to couple to photons, leading to two extra spectral lines in the neutral QD emission. However, for the QDs used for this work the intensity of these lines is very low and they are not studied in detail. Furthermore, the mixing of the bright and dark states adds an additional component to the FSS. Unlike in the case of a Faraday field, this component is in the linear eigenstate basis and so effectively acts to vary the magnitude of the FSS. Thus a Voigt magnetic field can be used to tune s in a similar manner to the vertical electric field method detailed in chapter 4. Hence the Voigt configuration allows the simultaneous application of two independent FSS tuning mechanisms.

The FSS in the presence of a Voigt magnetic field, B_V, is well approximated by

$$s\left(B_V\right) = s\left(0\right) + \kappa B_V^2, \tag{5.2}$$

where κ, which differs between QDs, is a parameter which depends on the in-plane anisotropy of the QD and the g-factors of the confined carriers which make up the exciton. This approximation assumes that B_V is small and that higher order terms in B_V can be neglected.

Equation 5.2 has been observed to well describe QDs similar to those studied in this thesis, at the field magnitudes available, in a study presented in reference [32]. In this study it is found that the Voigt field can either increase or reduce the magnitude of the FSS depending on the relative signs of $s\left(0\right)$ and κ. If these two parameters have the same sign then $|s|$ is increased however if the parameters have different sign $|s|$ is reduced, as can be seen from equation 5.2. Both $s\left(0\right)$ and κ are dependent on the QD in-plane anisotropy and so vary between QDs.

Figure 5.3 shows the energy of the neutral exciton states, along with the FSS, as a function of B_V. This figure shows the behaviour when $s\left(0\right) > 0$ and $\kappa > 0$ so $|s|$ is increased. For all of the QDs studied in this work κ is observed to have positive sign, however $s\left(0\right)$ can be tuned by varying an applied electric field as described in section 4.3.

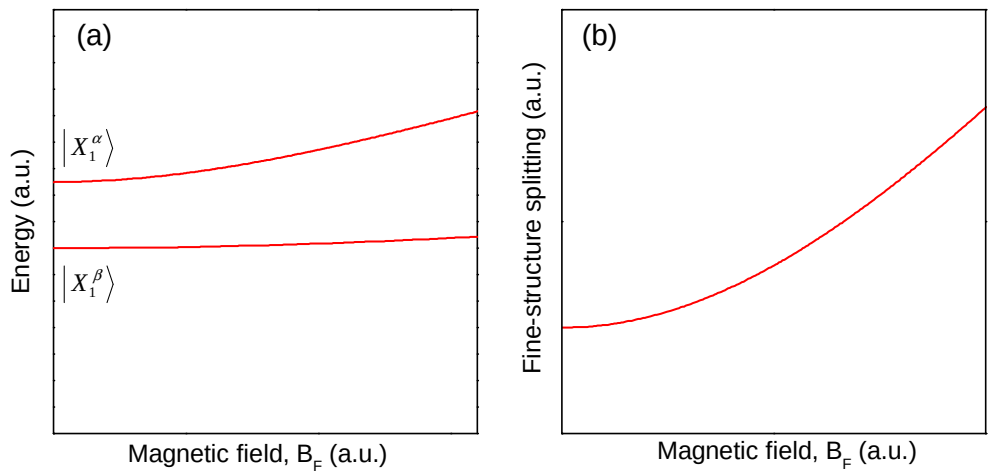

Figure 5.3: Effects of a Voigt magnetic field if $s(0)$ and κ both have positive sign. (a) Energy levels of the neutral exciton states as a function of Voigt field magnitude. (b) Fine-structure splitting as a function of Voigt field magnitude.

5.3 Faraday g-factor as a function of electric field

A magnetic field interacts with the spin of the exciton state via the Zeeman effect, the strength and nature of which are determined by the product of the magnetic field with the g-factor tensor of the qubit. The effects of electric field on the g-factor of confined carriers have been the subject of much research [57, 58, 59, 60, 61], motivated by the desire to influence the Zeeman interaction without requiring variation of the magnetic field. In Faraday geometry the energy splitting between the exciton eigenstates is dominated by the Zeeman component. In this section, the behaviour of the out-of-plane exciton g-factor, $g_X^\perp$, is investigated as a function of electric field.

The sample is mounted in Faraday geometry, as shown in figure 5.1a, and cooled to $\sim$ 5 K to allow photoluminescence (PL) spectroscopy measurements of the QD emission as a function of electric and magnetic field. In this configuration the electric and magnetic fields are both parallel with the growth direction of the sample. A continuous wave laser operating at 850 nm is used to excite the sample via the above-band regime described in

section 2.5. Low excitation power is used to avoid polarisation of the nuclear field via hyperfine interaction between the nuclei and the optically created carriers. The PL measurements are acquired using modified versions of the experimental arrangements shown in 3.4b-c, in which a quarter-waveplate is inserted in front of the sample. As the splitting due to the Zeeman interaction is in the circular basis, the quarter-waveplate allows selection of the decay path from which emitted photons are mapped onto the linear polarisation which is transmitted through the polarisation optics into the spectrometer.

As shown in equation 5.1, the Zeeman splitting is given by

$$s_{\{R,L\}} = g_X^{\perp} \mu_B B_F, \tag{5.3}$$

and so varies linearly with B_F with a gradient of $g_X^{\perp}\mu_B$. At the magnetic field magnitudes studied in this work the Zeeman splitting is large enough to be easily resolved by the spectrometer. Therefore, the quarter-waveplate is set to allow emission from both decay paths into the spectrometer simultaneously. The Zeeman splitting is then extracted by fitting Lorentzian functions to each of the peaks in the emission spectra.

Figure 5.4a shows the emission from the two neutral transitions, $|X_2\rangle \rightarrow |X_1\rangle$ and $|X_1\rangle \rightarrow |0\rangle$, in the absence of a magnetic field and with a magnetic field of $B_F = 1$ T. The Zeeman splitting as a function of B_F is shown in figure 5.4b, along with a linear fit to the data from which the effective exciton g-factor, $g_X^{\perp}$, is extracted.

The value of $g_X^{\perp}$ as a function of electric field is shown in figure 5.5. The g-factor is observed to be remarkably robust to changes in the applied electric field, with $g_X^{\perp} = 3.22 \pm 0.15$ across the entire range of over 200 kV cm^{-1}. This is in contrast to the recent study by Jovanov *et al.*[61], in which the effective g-factor is observed to vary 250% over a range of a few tens of kV cm^{-1}. Jovanov *et al.* used larger, lower Indium content QDs in which the carriers are subjected to a weaker confinement potential than the QDs studied in this thesis. QD shape and Indium concentration have been shown to be important factors in determining the g-factors of confined carriers[62, 63]. In addition, the increased confinement potential of the QDs studied in this thesis results

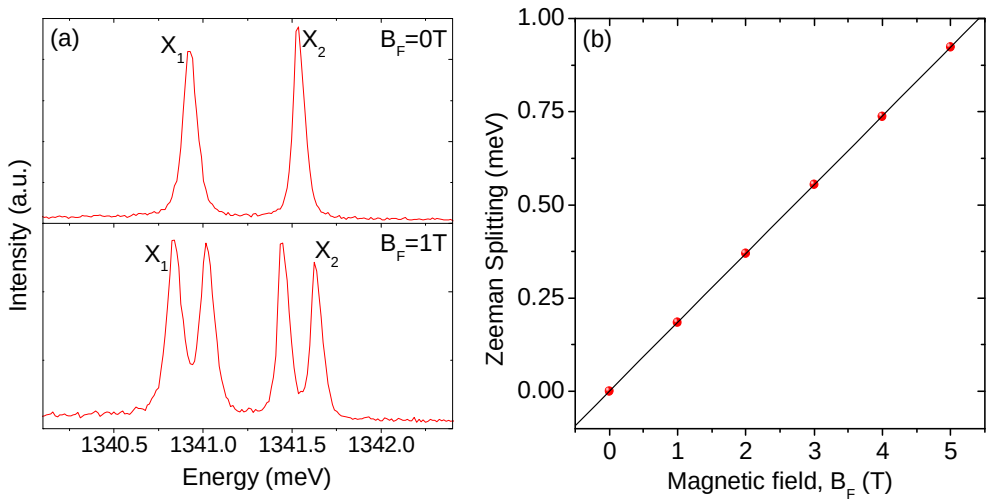

Figure 5.4: Effects of Zeeman splitting. (a) PL spectra of the neutral emission from an example QD at magnetic fields of $B_F = 0$ T and $B_F = 1$ T, the Zeeman splitting can clearly be resolved. The peaks are labeled according to the initial state of the corresponding transition. (b) Zeeman splitting as a function of B_F. The black line is a linear fit from which an effective exciton g-factor of $g_X^{\perp} = 3.19 \pm 0.01$ is extracted

in less redistribution of the confined carriers' wavefunctions in response to an electric field. This qualitatively explain the difference between the results observed here and those of Jovanov *et al.*, however further work is required before any firm conclusions can be made.

5.4 Magnetic and electric tuning of the fine-structure splitting

The effects of the simultaneous application of electric and magnetic fields on the FSS can be investigated when the sample is mounted in the Voigt geometry configuration shown in figure 5.1. In this configuration both the magnetic field, B_V, and electric field, F, tune the FSS in the linear basis. Recall from section 4.4 that the behaviour of the FSS is well described by a coherent coupling model. In this model the FSS as a function of electric field

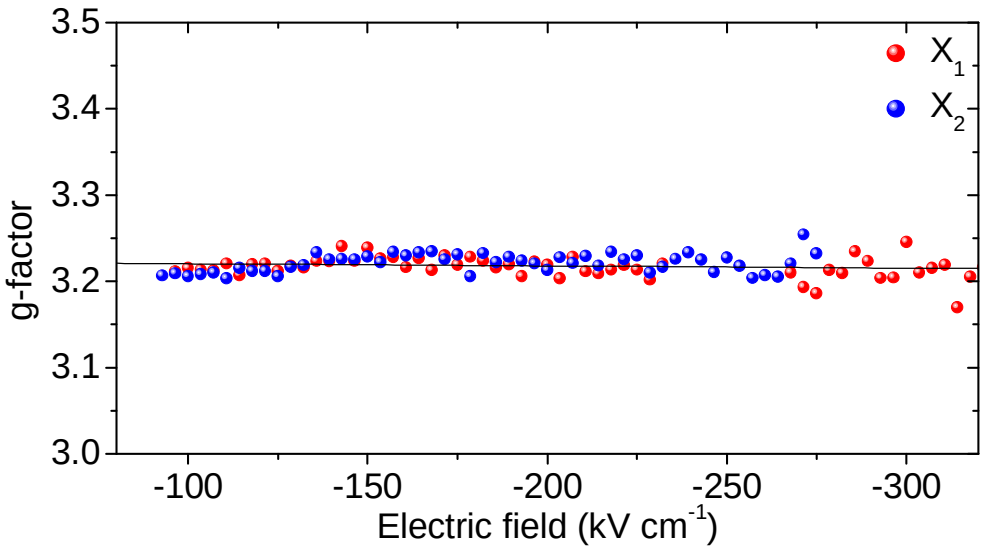

Figure 5.5: Effective exciton g-factor as a function of electric field. Values obtained from fits to the $|X_1\rangle \rightarrow |0\rangle$ transition are shown in red, and those from the $|X_2\rangle \rightarrow |X_1\rangle$ transition are shown in blue. The solid black line is a linear fit to the data.

is given by

$$|s| = \sqrt{\gamma^2 \left(F - F_0\right)^2 + s_0^2}, \tag{5.4}$$

where γ is the rate at which s varies with electric field in the absence of coupling effects, F_0 is the electric field required to minimise $|s|$, and s_0 is the minimum value to which $|s|$ can be tuned. In this section the effects of simultaneous application of a Voigt magnetic field with the electric field are investigated.

As in chapter 4, the FSS as a function of electric field is measured using the technique described in section 3.4, with the bias applied to the sample used to set the electric field for each measurement. This procedure is repeated for a range of different values of B_V in order to investigate the effects of a Voigt magnetic field. Figure 5.6a shows several measurements of $|s|$ as a function of electric field, each measured with a different value of B_V, for an example QD. The anticrossing behaviour observed in the absence of a magnetic field persists when a Voigt field is applied. Each data set is fit with

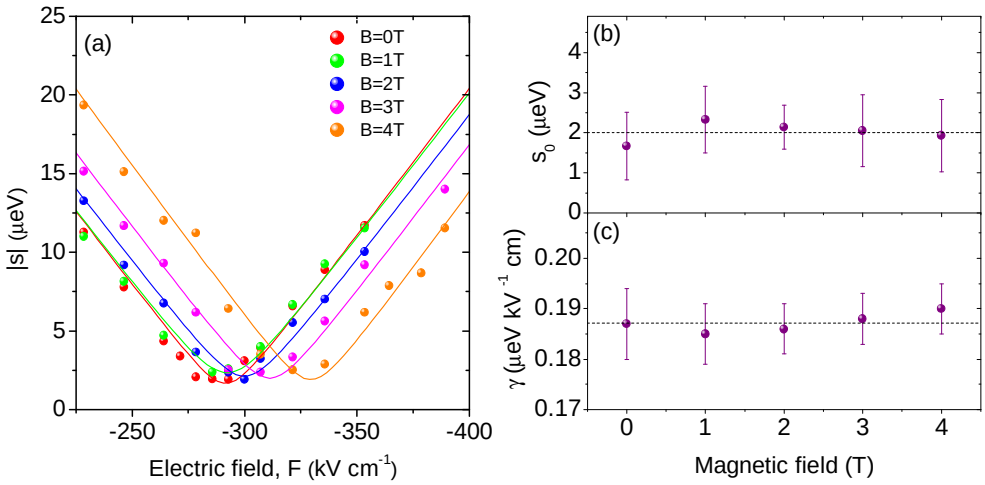

Figure 5.6: Effects of electric and Voigt magnetic field on the fine-structure splitting. (a) Magnitude of FSS as a function of electric field for five different values of B_V. (b)-(c) Minimum FSS (s_0) and tuning rate of s with electric field (γ) as a function of Voigt magnetic field. These values are extracted from the fits shown in (a), the length of the error bars correspond to one standard error from the fit. Dashed horizontal lines indicate the mean of all five data points.

equation 4.8 from the model detailed in section 4.4.

Several interesting observations can be made from these measurements. Figures 5.6b-c show the values of s_0 and γ, which are extracted from the fits to the data in figure 5.6a, as a function of B_V. The values of these parameters are independent of the applied Voigt magnetic field, within the measurement resolution. Recall from section 4.3 that γ is given by the difference in permanent z dipole moment between the two exciton eigenstates. Thus figure 5.6c implies that this difference is not changed by the application of a Voigt magnetic field. The fact that s_0 does not vary with B_V indicates that the strength of the coupling between the two exciton eigenstates is not affected by a Voigt magnetic field. This result is sensible because it is known that a Voigt magnetic field does not induce mixing between the two bright exciton states.

Interestingly, the value of F_0 is dependent on the Voigt magnetic field. This dependence manifests itself as an increasing translation along the x-axis of the data sets shown in figure 5.6a as B_V is increased. This behaviour can

be explained by considering the additional contribution to the FSS induced by the Voigt magnetic field, along with the observation that the coupling strength is independent of this field. As the Voigt magnetic field adds an additional component of κB_V^2 to the FSS the magnitude of F required to minimise s is increased. The value of F_0 is thus dependent on B_V and is given by

$$F_0\left(B_V\right) = F_0\left(0\right) - \frac{\kappa}{\gamma} B_V^2. \tag{5.5}$$

Where $F_0\left(0\right)$ is the value of F_0 in the absence of a magnetic field and the second term in this equation is the change in electric field required to remove the extra FSS induced by B_V. Figure 5.7a shows F_0 as a function of B_V. The data points are extracted figure 5.6a. The solid line shows a fit of equation 5.5 to the data, with a value of $\kappa = 0.45 \pm 0.02$ μeV T^{-2}.

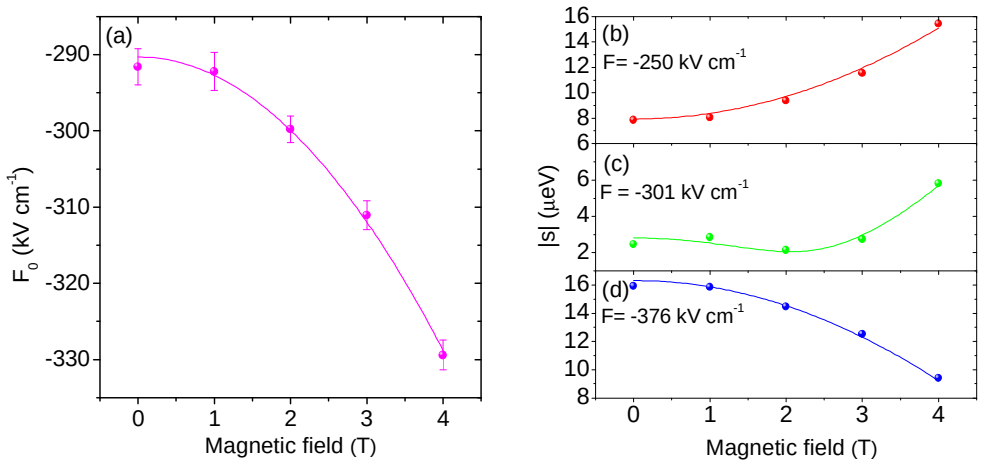

Figure 5.7: Effects of Voigt magnetic field on F_0 and $|s|$. (a) The electric field at which $|s|$ is minimised, F_0, as a function of Voigt magnetic field, B_V. The data points are extracted from fits to the data in figure 5.6. The solid line is a fit using equation 5.5. (b)-(d) $|s|$ as a function of B_V for three different fixed electric fields.

The behaviour of $|s|$ as a function of simultaneous electric and Voigt magnetic field is found by substitution of equation 5.5 into equation 5.4.

This gives

$$|s\,(F, B_V)\,| = \sqrt{\gamma^2 \left(F - \left(F_0\,(B_V = 0) - \frac{\kappa}{\gamma} B_V^2\right)\right)^2 + s_0^2}, \qquad (5.6)$$

which reduces to equation 5.2 in the limit of fixed F and $s_0 = 0$.

Figures 5.7(b)-(d) show $|s|$ as a function of B_V for three different values of F. The solid lines are calculated for each electric field using equation 5.6, with the values of γ, κ, s_0, and F_0 extracted from the data in figure 5.6. When $F = -250$ kV cm^{-1}, as in figure 5.7b, $s\,(B_V = 0)$ has positive sign. Thus as s is increased by the Voigt magnetic field $|s|$ is also increased. However, when $F = -376$ kV cm^{-1}, as in figure 5.7d, $s\,(B_V = 0)$ is negative. At this field the increase in s due to the Voigt magnetic field results in a reduction of $|s|$. Figure 5.7c shows an example of an electric field where B_V inverts the sign of s, note that s does not pass through zero as $|s|$ can not be reduced below $s_0 \simeq 2.0$.

5.5 Towards wavelength-tunable entangled emission

As shown in section 4.5, entanglement between the two photons emitted from the neutral biexciton cascade can be observed when $|s|$ is tuned to be close to zero. In this section measurements of a QD with $s_0 \sim 0.6\mu$eV are presented. This value of s_0 is below the threshold required to generate entangled photon pairs. Furthermore, with the application of a Voigt magnetic field, the electric field at which $|s| = s_0$ can be varied. Thus the energy of the emitted photons when $|s| = s_0$ is varied, allowing the creation of a source which emits entangled photon pairs with tunable emission energy.

Figure 5.8a shows the emission from the neutral biexciton cascade of the QD as a function of energy and electric field when $B_V = 0$. The parabolic Stark-shift of the emission with increasing $|F|$ is clearly visible. Figure 5.8b shows $|s|$ as a function of electric field for six different values of B_V, along with fits to the data using equation 5.6. As seen above in figure 5.8, and

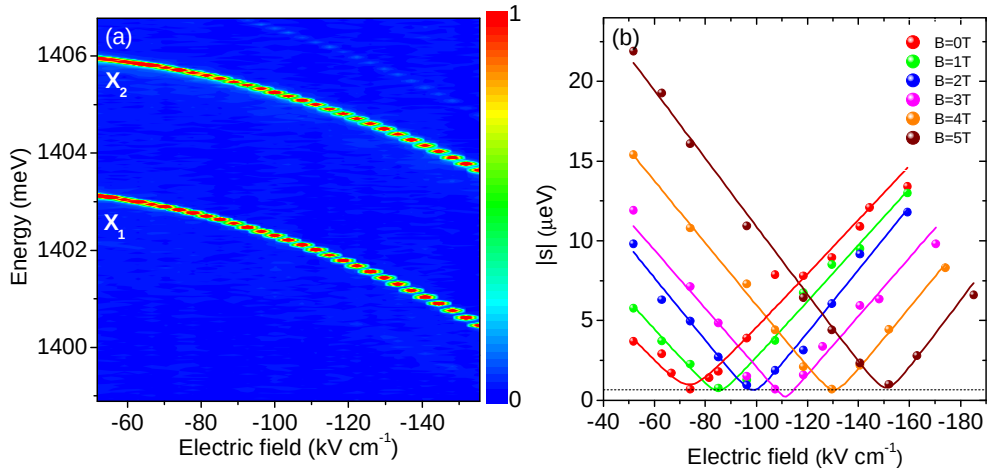

Figure 5.8: Emission energy and fine-structure splitting as a function of electric and magnetic field. (a) Emission intensity as a function of energy and electric field when $B_V = 0$. The two neutral emission peaks are labeled with the initial state of the corresponding transition. (b) FSS as a function of electric field for six different values of Voigt magnetic field. Solid lines are fits with equation 5.6.

quantified by equation 5.5, the data sets translate along the x-axis as B_V is increased. However, the value of s_0 remains constant, as can be seen in figure 5.9a. Thus, this QD can emit photon pairs with a high fidelity to the maximally entangled Bell state, $|\Psi^+\rangle$, at a range of electric fields, providing that B_V is set to the appropriate value.

Recall from section 4.3 that the Stark shift in the emission energy of a given QD transition is dependent on the permanent z dipole moment and polarisability, denoted p and β respectively, of the states involved and is given by

$$E = E_0 - pF + \beta F^2. \tag{5.7}$$

The fidelity to $|\Psi^+\rangle$ of the two-photon state emitted by the neutral biexciton cascade is maximised when $|s| = s_0$. Therefore, maximal entanglement between the two photons is observed when $F = F_0$. Figure 5.9b shows the energy of photons emitted from the two neutral transitions at $F = F_0$ for several different values of B_V. Over the 5 T range of B_V available in this work, the $|X_2\rangle \rightarrow |X_1\rangle$ and $|X_1\rangle \rightarrow |0\rangle$ transitions show a tuning range of

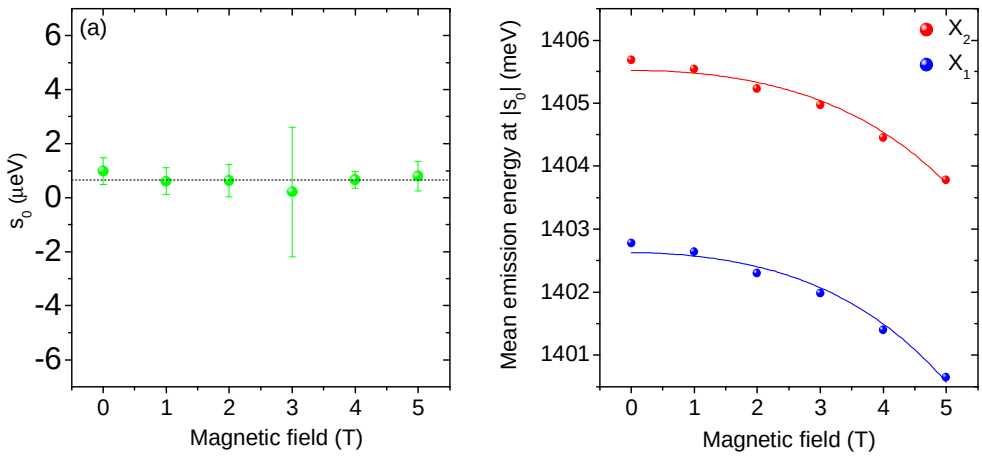

Figure 5.9: Data showing the potential to create a tunable-energy entangled pair source. (a) Minimum fine-structure splitting as a function of Voigt magnetic field. (b) Emission energy of the $|X_2\rangle \rightarrow |X_1\rangle$ (red spheres) and $|X_1\rangle \rightarrow |0\rangle$ (blue spheres) at $F = F_0$ as a function of Voigt magnetic field. Solid lines show fits as described in the main text.

1.9 meV and 2.1 meV, respectively.

The emission energy of each transition when $F = F_0$ can be calculated as a function of B_V via substitution of equation 5.5 into equation 5.7 to give

$$E = E_0 - p\left(F_0(B_V = 0) - \frac{\kappa}{\gamma}B_V^2\right) + \beta\left((F_0(B_V = 0) - \frac{\kappa}{\gamma}B_V^2\right)^2. \quad (5.8)$$

The solid lines in figure 5.9b show fits to the data using this equation, with the Stark shift parameters extracted from figure 5.8a and the values of E_0, $F_0(B_V = 0)$, and γ extracted from the data in figure 5.8b. These fits yield $\kappa = 0.52 \pm 0.2$ μeV T^{-2} for this QD.

The tuning range over which the energy of the entangled photons can be varied is restricted by two parameters: the maximum electric field that can be applied without quenching the optical activity of the QD; and the maximum available magnitude of B_V which can be applied. In the work presented in this thesis, the tuning range is limited by the latter, as the maximum field strength that could be generated was $B_V = 5$ T. However, it is interesting to consider the maximum tuning range which would be possible if larger B_V

could be applied.

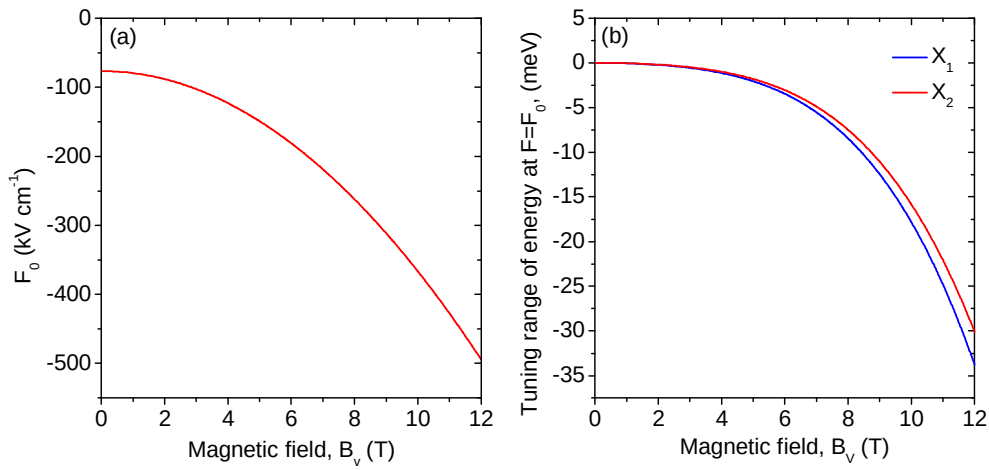

Figure 5.10: Calculation of the maximum energy tuning range for the QD studied in this section. (a) Electric field required to minimise $|s|$, and thus maximise the fidelity of entanglement of the two-photon state emitted by the neutral biexciton cascade, as a function of B_V. (b) Energy by which the emission from the two neutral transitions is tuned as a function of B_V.

Optical emission of the devices studied in this work is typically quenched when $|F| > 500$ kV cm^{-1}. Figure 5.10a shows the calculated value of F_0 as a function of B_V, using equation 5.5, for the QD studied in this section. From this it can be seen that a magnetic field of up to $B_V = 12$ T can be applied before $|F_0|$ becomes large enough to quench the emission. Figure 5.10b shows the energy by which the entangled emission is tuned as a function of B_V, which is found by calculating $E(B_V) - E(0)$ using equation 5.8. The maximum tuning range, which is achievable with a magnet capable of applying 12 T, is 30.1 meV and 33.8 meV for the $|X_2\rangle \rightarrow |X_1\rangle$ and $|X_1\rangle \rightarrow |0\rangle$ transitions, respectively.

Thus, the application of a magnetic field in the plane of the sample, in conjunction with an electric field in the growth direction, is a promising technique for the generation of energy-tunable entangled photon pairs. The key to this tuning mechanism is the fact that s_0, which varies between QDs, is independent of the applied Voigt magnetic field. However, whilst this allows the fidelity to the $|\Psi^+\rangle$ state to be constant across a large energy range,

the value of the fidelity is determined by the value of s_0. As a result, this method requires the selection of special QDs which have appropriately small values of s_0. However, the two recent studies which use the simultaneous application of two different tuning methods[55, 56] both report the ability to reduce or eliminate s_0. These studies achieve manipulation of s_0 via the application of strain fields to the QDs, but they do not demonstrate the ability to significantly tune the emission energy when $|s| = s_0$. This raises the possibility that combining an applied strain field with the electric and magnetic fields used in this chapter could allow control of s_0, whilst also enabling the energy of emission when $|s| = s_0$ to be tuned. This approach has the potential to remove the requirement of searching through many QDs in order to identify those with suitable values of s_0, and as such could allow any typical InGaAs QD to be used as an energy-tunable entangled photon pair emitter.

5.6 Conclusion

The effects of simultaneous application of electric and magnetic fields on the energy structure of the bright neutral transitions has been investigated. Measurements in two different magnetic field geometries have been conducted. Faraday geometry measurements have allowed investigation of the out-of-plane g-factor of the exciton; and Voigt geometry measurements have been used to investigate the effects of magnetic field on the FSS of the exciton state.

The out-of-plane g-factor has been shown to be independent of an electric field applied parallel to the growth direction, in contrast to previous experimental and theoretical studies of other QDs with different composition. However, only the g-factor component which is parallel to the sample growth direction has been studied. A promising extension to this work would be to investigate the in-plane g-factor as a function of electric field.

The effects of a Voigt geometry magnetic field on the FSS tuning mechanism demonstrated in the previous chapter have been presented. The Voigt

magnetic field is found to affect only the value of the electric field at which the FSS is minimised, and not the strength of the coupling between the exciton states, or the rate at which the FSS is tuned by the electric field. This allows the combination of simultaneous electric and magnetic fields to be used to tune the energy of the neutral emission at which the FSS is minimised. Thus, if this tuning technique is applied to a QD with sufficiently small s_0, it is possible to create an energy-tunable entangled photon pair source. An interesting extension to this work would be to incorporate an additional tuning mechanism via mounting the sample on a piezo-electric layer to facilitate the application of a strain field. This extra tuning parameter would perhaps allow the value of s_0 to be varied via altering the coupling strength between the two bright neutral exciton eigenstates.

Chapter 6

Effects of nuclear field fluctuations and dynamic electric field on the exciton eigenstates in single quantum dots

6.1 Introduction

The previous chapters have concentrated on the neutral biexciton cascade and the generation of entangled photon pairs from QD emitters. This chapter focuses on the temporal properties of the exciton state. This state is of interest because a single exciton stored within a QD provides a viable spin system for use as a solid-state qubit. Also, the evolution of the exciton state is governed by the energy difference between the two eigenstates, allowing further examination of the fine-structure splitting via time resolved measurements of the $|X_1\rangle \rightarrow |0\rangle$ transition. Thus, the effects on the stored exciton of the fluctuating nuclear field[64], and of a dynamically varied vertical electric field[20], can be investigated.

Single spins in semiconductor materials have generated significant interest

due to their potential applications in the fields of quantum computing and spintronics[65, 66, 67, 68, 69]. Carriers confined inside QDs interact with their environment via, amongst other effects, hyperfine interaction with the nuclear magnetic field of the lattice atoms[70]. These interactions can lead to reduction in solid-state qubit coherence times, however they also enable methods for qubit manipulation[71]. This has motivated much research into controlling the nuclear field, most notably via optical pumping of the nuclei into particular spin states[72, 73].

In addition, the optically active nature of the QDs studied here allows for an interface between photonic and solid-state qubits, with potential applications in hybrid quantum computing schemes[74]. Such a scheme would allow the advantages of each qubit system to be combined. Photons, with fast propagation speeds and long coherence times, are well suited for the transmission of quantum information[75, 76]; whilst solid-state qubits are usually more convenient to manipulate due to their stronger interaction with external fields and their environment.

In this chapter the exciton spin-state is initialised via a spin-preserving quasi-resonant excitation scheme and then manipulated by application of a dynamic electric field. The effect of the fluctuating nuclear field on the exciton state is investigated and shown to influence both the initialisation, and the subsequent evolution, of the exciton's spin. A phase-shift gate, capable of performing a single qubit rotation on photonic qubits, is demonstrated.

6.2 Temporal evolution of exciton superposition states

The temporal properties of the exciton state have been studied in several different QDs. One QD with an exceptionally small s_0 of $\sim 0.4\mu$eV is studied in detail, as the subtle effects of the nuclear magnetic field become more apparent at small $|s|$. This QD is embedded inside a P-I-N diode, as described in section 3.2. The diode has lateral dimensions of 35×60 μm, which is smaller than the 360×360 μm devices studied in the previous chapters. The

reduced capacitance of the smaller area device leads to a faster response to changes in the applied electric field. This is beneficial for studying the system under the dynamic conditions explored in this chapter.

6.2.1 State initialisation

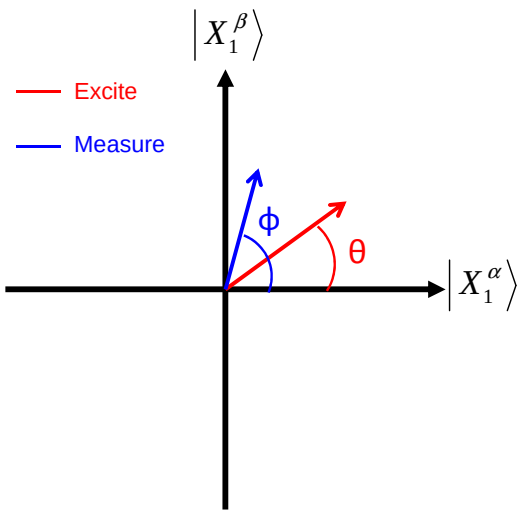

Figure 6.1: Diagram showing the orientation of the excitation and measurement axes, relative to the exciton eigenstates, for the case of excitation in the linear polarisation bases. The angle θ determines the state which is initialised and angle ϕ selects the state to be measured.

The QD is initialised into the $|X_1\rangle$ state using the quasi-resonant excitation scheme described in section 2.5, which drives only the $|0\rangle \rightarrow |X_1\rangle$ transition. The phonon-assisted excitation regime maps the polarisation of the excitation photon onto the spin of the resulting exciton[77, 20]. This allows the QD to be initialised into either of the $|X_1^{\alpha,\beta}\rangle$ eigenstates or into a superposition state. Consider an excitation photon with linear polarisation orientated at an angle θ to the exciton eigenstates as shown in figure 6.1. The projection of such a photon into the eigenstate basis ($\{\alpha, \beta\}$) is given by

$$|\Psi_{\text{in}}\rangle = \cos\theta|\alpha\rangle + \sin\theta|\beta\rangle, \tag{6.1}$$

and the corresponding wavefunction of the resulting exciton is

$$|\Psi_{X_1}(t)\rangle = \cos\theta|X_1^{\alpha}\rangle \exp\left(\frac{-iE_{\alpha}t}{\hbar}\right) + \sin\theta|X_1^{\beta}\rangle \exp\left(\frac{-iE_{\beta}t}{\hbar}\right). \tag{6.2}$$

Thus via variation of the linear polarisation of the excitation photon, θ, it is possible to initialise the exciton into any superposition of the two spin eigenstates in the linear bases.

6.2.2 Temporal measurements of fine-structure splitting

It is useful to consider the initialisation process described above as a direct mapping between the polarisation of the photon represented on the Poincaré sphere and the spin of the exciton represented on the Bloch sphere. This mapping is depicted in figure 6.2 with the eigenstate axis of the Bloch sphere orientated vertically. Using this analogy, and considering only excitation with a linearly polarised photon as in the example above, the spin-state is created in the plane of the linear bases states. The projection onto the eigenstate axis is determined by θ, as shown in figure 6.2a.

Whilst the exciton remains in the QD it evolves according to equation 6.2. If $\theta = m\frac{\pi}{2}$, where m is an integer, an eigenstate is initialised and the system is stationary. For other values of θ a superposition state is created and a phase difference accumulates between the two eigenstate components at a rate of $\frac{E_{\alpha}-E_{\beta}}{\hbar}$. This causes a precession, with angular frequency $\frac{s}{\hbar}$, of the spin-state around the eigenstate axis of the Bloch sphere.

As can be seen from figure 6.2b, the projection of the spin-state into each of the superposition bases ($\{\alpha_{45}, \beta_{45}\}$ and $\{R, L\}$) varies sinusoidally as the state precesses. When the exciton radiatively decays its spin at that time is mapped onto the polarisation of the emitted photon, as shown in figure 6.2c. The resulting intensity of the emission measured along a linear polarisation axis at an angle ϕ to the eigenstates, as shown in figure 6.1, is given by

$${}_{\phi}\langle\Psi_{\text{out}}|\Psi_{\text{out}}\rangle_{\phi} = \left[a_{\theta,\phi} + b_{\theta,\phi}\cos\left(\frac{st}{\hbar}\right)\right]\exp\left(-\frac{t}{\tau_r}\right), \tag{6.3}$$

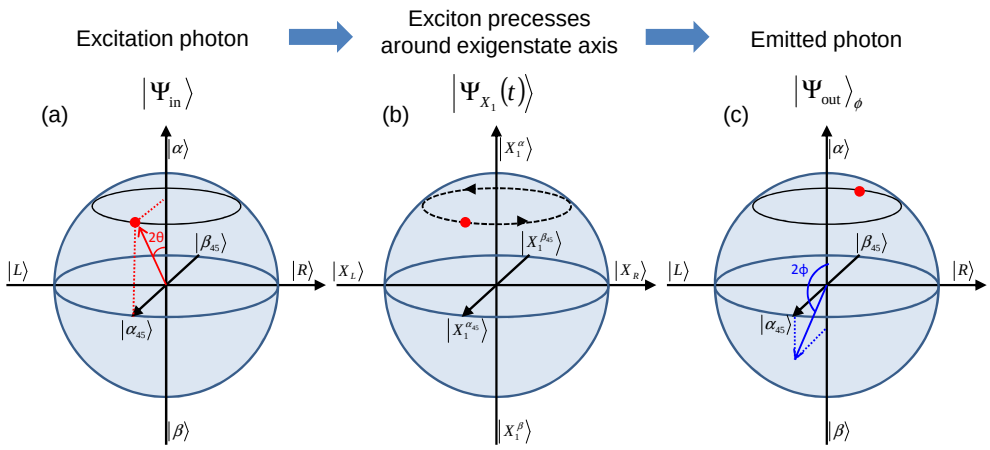

Figure 6.2: Visual representation of the photon → exciton → photon process. The linear polarisation of the excitation photon maps onto the spin state of the created exciton. The exciton then precesses around the eigenstate axis. The spin state of the exciton when it recombines is mapped onto the polarisation of the emitted photon, which is measured along a polarisation axis defined by angle ϕ.

where τ_r is the radiative decay time of the $|X_1\rangle$ state. The parameters $a_{\theta,\phi}$ and $b_{\theta,\phi}$, which are constant for a given combination of θ and ϕ, are given by

$$\begin{aligned} a_{\theta,\phi} &= \cos^2(\theta)\cos^2(\phi) + \sin^2(\theta)\sin^2(\phi) \\ b_{\theta,\phi} &= 2\cos(\theta)\sin(\theta)\cos(\phi)\sin(\phi). \end{aligned} \tag{6.4}$$

Polarised time-resolved spectroscopy, as detailed in section 3.3, will thus yield a signal which varies sinusoidally with an envelope defined by the radiative lifetime of the exciton within the QD. The amplitude and visibility of the oscillations are given by $b_{\theta,\phi}$ and $|\frac{b_{\theta,\phi}}{a_{\theta,\phi}}|$ respectively. Maximum visibility is observed when both exciting and measuring a maximum superposition state, i.e. when θ and ϕ are both equal to an odd integer multiple of $\frac{\pi}{4}$, which corresponds to measuring the system in the $\{\alpha_{45}, \beta_{45}\}$ basis. From the intensity oscillations it is possible to extract $|s|$, this is achieved by fitting the data with equation 6.3 as shown in figure 6.3a. Figure 6.3b shows $|s|$ as a function of electric field measured using this time-resolved technique, along with the corresponding values obtained from the spectral method detailed in

section 3.4. The two measurement methods are in good agreement.

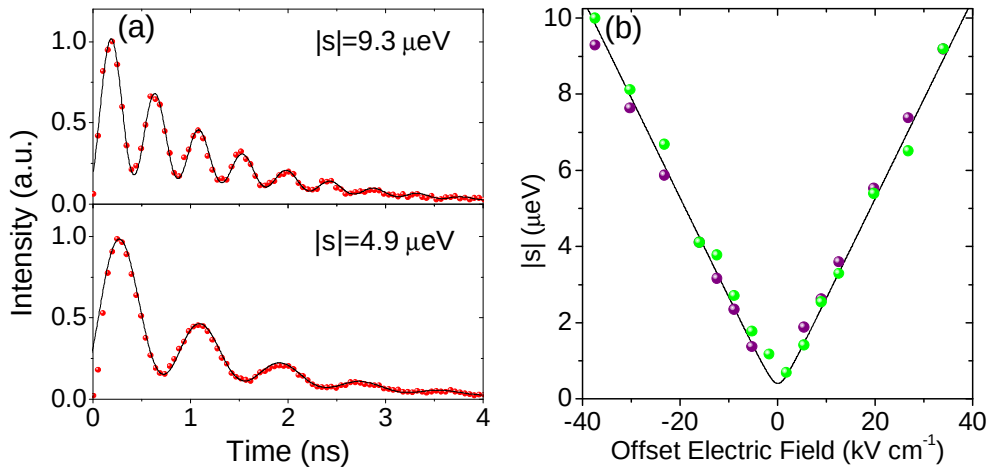

Figure 6.3: Temporal measurements of the fine structure splitting. (a) Polarisation resolved time-resolved PL measurements for two different values of $|s|$. The exciton state is initialised into a maximum superposition state and the resulting emission is polarisation filtered to select emission from the same superposition state. Red spheres are data points and the blacks line are the fits, described in the main text, from which $|s|$ can be extracted. (b) Fine structure splitting as a function of electric field measured in the spectral domain (green spheres) and extracted from fits to the time-resolved PL data (purple spheres). The solid line is a fit to the data using equation 4.8.

Note that although the above discussion considers the example of initialisation and measurement in the linear bases, it is also possible to perform the same measurements in the circularly polarised basis. Circularly polarised photons initialise the exciton into either state $|X_L\rangle$ or $|X_R\rangle$. Polarised time-resolved spectroscopy measurements in the circular basis are proportional to the projection of the spin-state onto the circular axis of the Bloch sphere. Thus, oscillating behaviour, as in the linear case explain above, is observed as the spin-state precesses around the eigenstate axis.

6.3 Fluctuating nuclear field

For this work, the nuclei field is modeled as an effective magnetic field with varying magnitude, described by a normal distribution, and a randomly vary-

ing orientation. Although this method of analysis neglects the quantum nature of the interaction, it is sufficient to explain the effects observed in this study. This is because the exciton interacts with a bath of thousands of nuclei, the resultant field of which approximates the simple model used here.

As detailed in section 5.2, magnetic field induces an additional splitting between the exciton eigenstates. The fluctuating nuclear magnetic field thus adds a time-varying component to the fine-structure splitting. It is convenient to consider the Faraday and Voigt components of the nuclear field separately. Recall that the Faraday component, B_F, introduces a splitting in the circular basis, $s_{\{R,L\}} = g_X^{\perp}\mu_B B_F$, such that

$$s = \sqrt{s_{\{\alpha,\beta\}}^2 + s_{\{R,L\}}^2}, \tag{6.5}$$

where $s_{\{\alpha,\beta\}}$ is the splitting in the eigenstate basis, which is observed via the polarised PL spectroscopy measurements (see section 3.4) throughout the previous chapters. The extra circular component of the splitting also leads to a rotation in the orientation of the eigenstates (θ_0 from section 2.7) which, as described in section 4.4, is dependent on $|s|$.

Recall also that the Voigt component, B_V, introduces an additional linear splitting with a magnitude that is well approximated by κB_V^2. As the in-plane g-factor of the exciton is much lower than that for out-of-plane magnetic fields, κ is small, of the order 1μeV T^{-2}[52, 32, 15]. This results in the contribution to $s_{\{\alpha,\beta\}}$ due to B_V being negligible at the small field magnitudes generated by the nuclei. The remainder of this section concentrates on the effects of the Faraday component.

From equation 6.5 it can be seen that the circular splitting can only increase the total fine-structure splitting. The spectral measurement technique used in the previous chapter can observe only the projection of the splitting into the linear basis. Thus, in principle, the temporal measurements of $|s|$ should yield a larger value than those measured spectrally. However, the orientation of B_F is random and fluctuates over a timescale of milliseconds[78], whilst the measurements are typically integrated over several minutes. The time-averaged $s_{\{R,L\}}$ is thus much smaller than $g_{X\parallel}\mu_B B_F$, and in practice the

difference between the spectral and temporal measurements of $|s|$ is smaller than the measurement noise, as shown in figure 6.3.

6.3.1 Free induction decay

The effect of fluctuations in $s_{\{R,L\}}$ can be observed in the evolution of the degree of polarisation of the emission as a function of vertical electric field. The degree of polarisation is analysed in the two linear bases, $\{\alpha, \beta\}$ and $\{\alpha_{45}\beta_{45}\}$, and the circular basis, $\{R, L\}$, in a similar manner to section 4.5. The degree of polarisation in a basis $\{i, j\}$ is given by

$$C_{\{i,j\}}(t) = \frac{I_{i,i}(t) - I_{i,j}(t)}{I_{i,i}(t) + I_{i,j}(t)}, \tag{6.6}$$

where $I_{i,i}(t)$ and $I_{i,j}(t)$ are the intensity of the co- and cross-polarised time-resolved spectroscopy measurements, respectively.

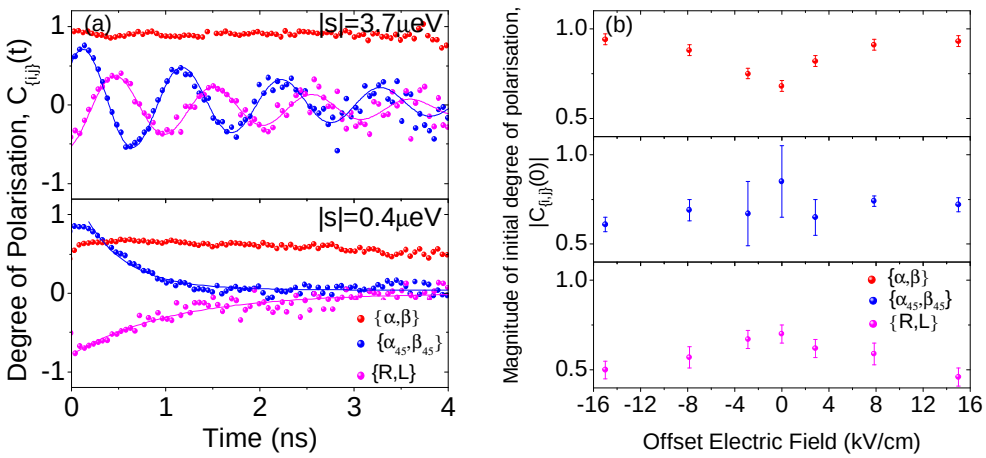

Figure 6.4: Degree of polarisation. (a) Degree of polarisation as a function of time for the same QD at two different values of electric field. Top pane has $|s| = 3.7\mu$eV, bottom pane has $|s| = s_0 = 0.4\mu$eV. (b) Magnitude of the initial degree of polarisation as a function of vertical electric field, offset by the field required to tune the QD to $|s| = s_0$.

Figure 6.4a shows the degree of polarisation as a function of time, measured in each of the three bases, for the same QD at two different electric

fields and thus different $|s|$. In the top pane $|s| = 3.7\mu$eV, which as can be seen from figure 6.3b is far from the anticrossing; in the bottom pane $|s| = s_0 = 0.4\mu$eV. At both electric fields the $\{\alpha, \beta\}$ basis, which is aligned with the exciton eigenstates, maintains a high degree of polarisation throughout the measurement. This is expected as the eigenstates do not evolve in time. However, the two superposition bases show different behaviour at each electric field.

Far from the anticrossing, the degree of polarisation measured in the superposition bases oscillates in time. This is due to the precession of the exciton state around the eigenstate axis on the Bloch sphere, which results in a sinusoidal variation in the projection of the spin state onto each of the superposition bases. The data is well described by a function of the form $\propto \sin\left(\frac{|s|(t-t_0)}{\hbar}\right) \exp\left(\frac{-t}{\tau_{\mathrm{FID}}}\right)$, where t_0 gives the phase of the oscillations and τ_{FID} describes the decay time of the oscillations as discussed below. Fits with this function are shown as solid lines in the top pane of figure 6.4.

At the anticrossing these oscillations can not be observed. This is because for small $|s|$ the period of the oscillations is increased and becomes comparable to τ_{FID}, causing the system to behave as an overdamped oscillator. Exponential fits, shown as solid lines in the bottom pane, are in good agreement with the data.

Two other differences between the behaviour of the system at the two electric fields are also apparent. The timescale over which the degree of polarisation decays (τ_{FID}) is shorter when $|s| = 0.4\mu$eV than when $|s| = 3.7\mu$eV. In addition, the initial degree of polarisation, $C_{\{i,j\}}(0)$, for each of the measurement bases is different at the two values of $|s|$. Figure 6.4b shows $|C_{\{i,j\}}(t = 0)|$, for the three measurement bases, as a function of electric field offset by the field required to tune $|s|$ to s_0. The degree of polarisation with which the eigenstate basis can be initialised shows a dip at the anticrossing, however that of the two superposition bases shows an increase in this region. These observations can be explained by considering the effects of the fluctuating circular splitting ($s_{\{R,L\}}$), which are analogous to phenomena observed in nuclear magnetic resonance measurements[79, 80] as described below.

NMR measurements probe an ensemble of spins as they precess around an applied magnetic field. The signal obtained from measuring the projection of the spins along a direction perpendicular to the applied magnetic field displays oscillations which decay away in a process called "free induction decay" (FID). The decay in the transverse plane, which is the component most relevant to the work presented here, is referred to as "T_2" decay. This component of the decay is caused by the different spins precessing at different rates due to spin-spin interaction and environmental factors, such as local variation in the magnetic field or susceptibility.

In this work, a single spin state is initialised many times and the resulting emission when the exciton decays is integrated over several minutes to build up the measurement. The timescale of the radiative decay of the exciton is on the order of nanoseconds, however the nuclear field fluctuations occur over a timescale of milliseconds. This means that, although approximately constant whilst each individual exciton is stored in the QD, the value of B_F fluctuates throughout the timescale of the measurement. The value of B_F alters $|s|$ and θ_0 and thus it affects both the rate and orientation of the precession of the exciton state around the Bloch sphere. This leads to a temporal averaging of many spin precession rates over each measurement, resulting in effects similar to the spatial averaging in NMR measurements[64]. Both the initial degree of polarisation and the subsequent evolution observed in figure 6.4 can be qualitatively explained by considering these effects.

Initialisation of an eigenstate requires good alignment between the polarisation of the excitation photon and the eigenstate orientation. Far from the anticrossing the orientation of the eigenstates is not significantly affected by fluctuations in $|s|$ (see section 4.4). Therefore the initial degree of polarisation in the $\{\alpha, \beta\}$ basis is maximised away from the anticrossing. Conversely, at $|s| = s_0$ the orientation of the eigenstates is most sensitive to fluctuations in $|s|$, resulting in a reduction of the degree of polarisation with which the $\{\alpha, \beta\}$ basis can be initialised as observed.

The superposition states are less sensitive to the orientation of the excitation photon. However, as they precess around the eigenstate axis of the Bloch sphere they are sensitive to the temporal jitter in the excitation time

caused by the finite linewidth of the transition. The effects of the temporal jitter are less apparent at smaller values of $|s|$ due to the reduced rate of precession. Therefore, the degree of polarisation with which the superposition states can be initialised is maximised at $|s| = s_0$ as observed.

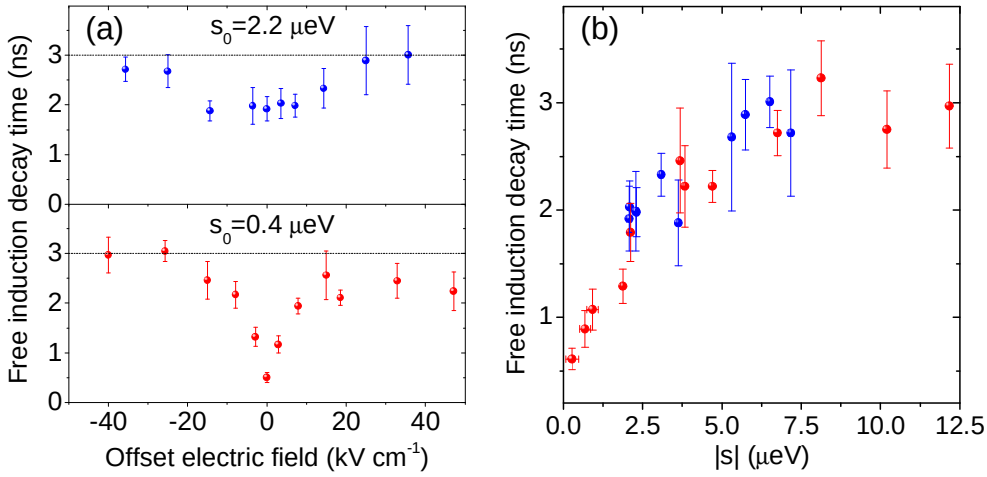

Figure 6.5: Free induction decay of the degree of polarisation as a function of electric field and $|s|$. (a) FID time as a function of electric field for two QDs with different values of s_0. Dashed horizontal lines indicate the FID time due to random spin scattering which is independent of the value of $|s|$. (b) The FID times from (a) are plotted as a function of $|s|$.

Figure 6.5 shows the free induction decay time, τ_{FID}, of the linear superposition state as a function of electric field, and as a function of $|s|$, for two QDs with different values of s_0. Interestingly, τ_{FID} has contributions from two different mechanisms. When $|s|$ is larger than $\sim 4\mu$eV, $\tau_{\text{FID}} \sim 3$ ns. This suggests that for $|s|$ in this region the effect of the fluctuating circular splitting is negligible compared to random spin-scattering between the two eigenstates (which is analogous to the T_2^* decay time in NMR). However for smaller values of $|s|$, the contribution from the nuclear field is more significant and dominates the decay time, leading to a reduction in τ_{FID} near the anticrossing for QDs with small enough s_0 for this to become observable. Within experimental, error τ_{FID} as a function of $|s|$ is the same for both QDs which suggests that it is independent of the coupling strength between the

two eigenstates. The origin of this effect can be explained by considering the contribution which $s_{\{R,L\}}$ makes to the total fine structure splitting. As can be seen from equation 5.1, the circular splitting sums in quadrature with the linear splitting ($s_{\{\alpha,\beta\}}$). The linear splitting is not dependent on the fluctuating nuclear field so when $s_{\{\alpha,\beta\}}$ is large, which is the case for $|s|$ far from s_0, the fluctuations in $s_{\{R,L\}}$ do not cause significant changes in $|s|$. Conversely, when $s_{\{\alpha,\beta\}}$ is small, the fluctuations in $s_{\{R,L\}}$ cause large relative changes in $|s|$, which results in large fluctuations in the trajectory that the exciton takes as it precesses around the Bloch sphere. Consequently, when $|s|$ is small the increased fluctuations in the measured trajectory cause the observed FID time to be reduced. A detailed numerical model offering a more quantitative explanation of these observations can be found in [64]. Note that the effects described in this section are due to the temporal integration of many trajectories around the Bloch sphere and would not be present in a "single-shot" measurement of the exciton state.

6.4 Dynamic manipulation of exciton states

In addition to the random fluctuations due to the effects of the nuclear field, $|s|$ can also be controllably varied in time by the application of a time-varying vertical electric field. Recall from equation 6.2 that the two eigenstate components of a superposition develop a phase difference at a rate of $\frac{s}{\hbar}$. Thus, the total phase difference accumulated is given by

$$\Theta = \int_0^t \frac{s(t)}{\hbar}\,\mathrm{d}t \tag{6.7}$$

and so can be controlled by varying s, allowing the implementation of a phase-shift gate.

This is achieved by applying a dc electric field to tune $|s|$ to $\sim 5\mu$eV and initialising the exciton in a maximum superposition state which proceeds to precess around the the Bloch sphere. An additional 500 ps Gaussian-shaped electric field pulse is then applied 250 ps after the initialisation via a signal

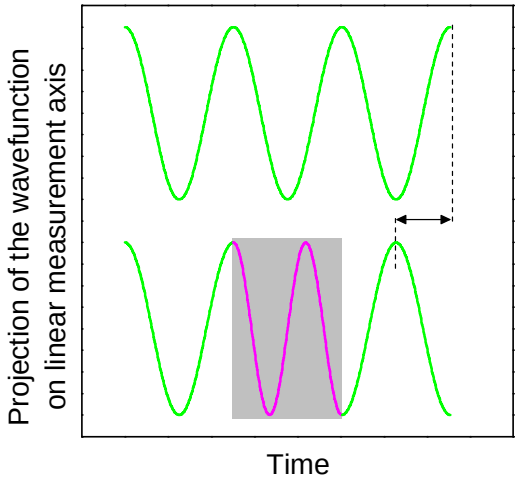

Figure 6.6: The projection of the exciton wavefunction onto a linear measurement axis as a function of time. In the bottom curve a gate pulse is applied, indicated by the grey box. The oscillation frequency is increased during this pulse and a phase difference, relative to the un-gated curve shown above, develops. A horizontal arrow indicates the induced phase offset due to the gate.

generator which is synchronised to the laser clock signal. Whilst this gate pulse is applied $|s|$ is increased and so the state precesses at a faster rate. This results in the accumulation of a phase difference relative to if the gate pulse were not applied, as shown schematically in figure 6.6.

6.4.1 Single qubit rotation

The above method for dynamically varying $|s|$ allows a controlled phase-shift to be applied to the exciton state whilst it is stored in the QD. This phase shift is transferred to the emitted photon when the exciton recombines, thus a single qubit rotation is performed whilst the qubit is stored in the QD.

As can be seen from equation 6.7, the induced phase shift is proportional to the area of the gate pulse. Figure 6.7a shows the induced phase shift as a function of the gate amplitude for a fixed pulse width of 500 ps as described above. At a gate amplitude of ~ 1.6 V a π phase-shift is observed. Figure 6.7b shows the intensity of co- and cross-polarised time-resolved spectroscopy measurements with and without a π phase shift. The intensity drops during

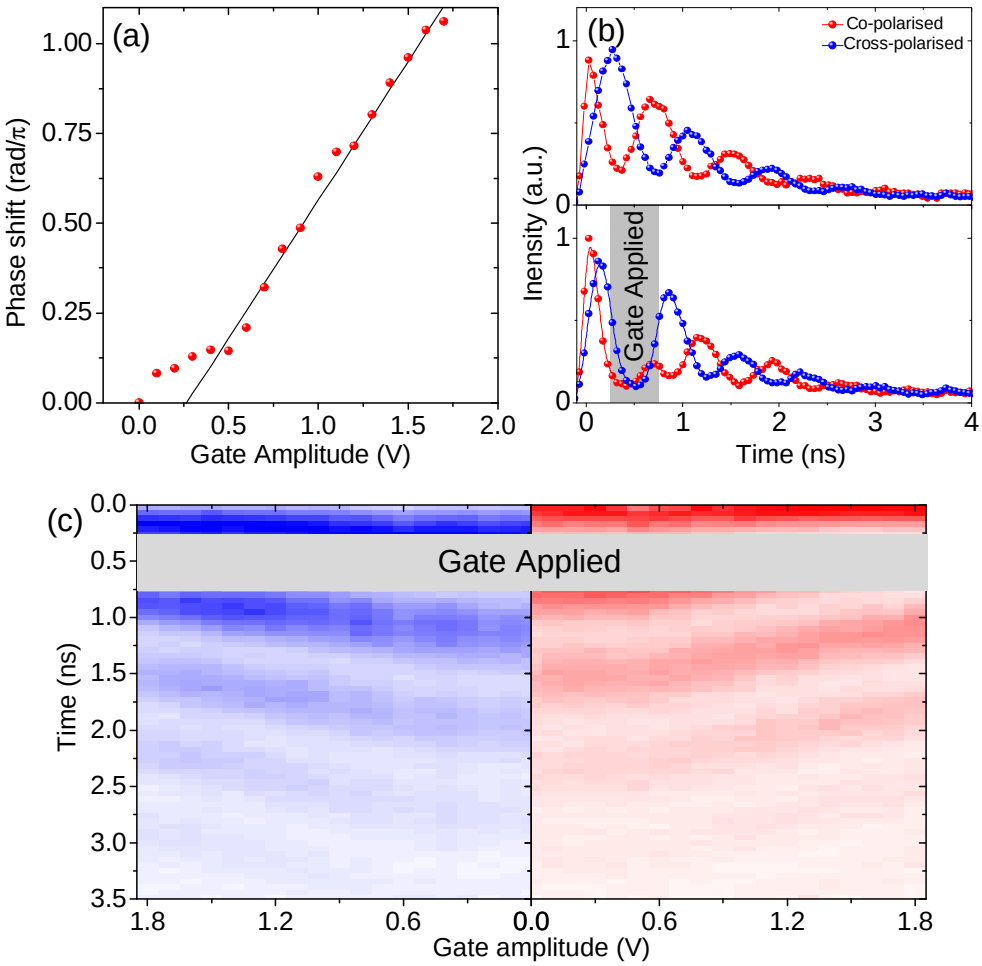

Figure 6.7: Phase-shift gate allowing single qubit rotations. (a) Phase shift as a function of gate amplitude. (b) co- and cross-polarised time-resolved spectroscopy measurements without (top) and with (bottom) an induced π phase shift. (c) Time-resolved spectroscopy measurements as a function of gate amplitude, the co- and cross-polarised data is coloured red and blue respectively.

the gate as the emission is Stark shifted out of the measured spectral range. After the gate the induced phase shift is clearly visible. Time-resolved spectroscopy measurements as a function of gate amplitude are shown for co- and cross-polarised emission in figure 6.7c.

This phase shift gate operates far from the anticrossing in the regime where the orientation of the eigenstates is not sensitive to variations in $|s|$. This allows the rate of precession about a fixed axis to be manipulated, facilitating a controlled rotation of the qubit as demonstrated. An alternate method of qubit control in which the eigenstate orientation and $|s|$ are manipulated is possible when operating close to $|s| = s_0$. In addition to a phase rotation of a superposition state, this method also allows mapping between the eigenstates. Details of this method can be found in [20].

6.5 Conclusion

The temporal evolution of the exciton state has been investigated, and the effect of the fluctuating field has been observed in time-resolved spectroscopy measurements in a manner analogous to FID in NMR measurements. The ability to initialise an exciton into an eigenstate or superposition state depends on $|s|$, with the fidelity of initialisation highest at $|s| \gg s_0$ for eigenstates but highest for superpositions at $|s| = s_0$. This work is also relevant to the generation of entangled photon pairs from the neutral biexciton cascade discussed in chapters 4 and 5, where the exciton state is prepared by the decay of the biexciton state rather than directly initialised as in this chapter. The temporal measurements presented here stress that even for large values of $|s|$ entanglement may still be observed. This is possible as long as the resulting evolution of the exciton state can be resolved and τ_{FID} is not shorter than the radiative lifetime of the exciton state. Thus as τ_{FID} is reduced for $|s| <\sim 4\mu$eV, it may not always be beneficial to minimise the fine-structure splitting.

A hybrid phase shift gate, capable of performing single qubit rotations, has been demonstrated via dynamic manipulation of $|s|$ with a pulsed vertical

electric field. Improvements to this gate could be achieved by using diode devices with smaller areas to decrease the time taken to respond to changes in the applied electric field, allowing more operations to be performed within the radiative lifetime of the stored exciton. In addition, scaling of this hybrid photonic-spin scheme could be achieved in the near future via the use of site-positioned QDs[81] and multiple local gates.

Chapter 7

Controlled-NOT gate operating with single photons

7.1 Introduction

The neutral exciton state has been studied in detail throughout this thesis. This chapter presents a demonstration of a basic optical quantum computing component using photons emitted from the $|X_1\rangle \rightarrow |0\rangle$ transition.

Photonic quantum computing schemes require non-classical light sources to initialise the system into the correct input state. The error-rate of state initialisation has significant consequences on the scalability of a computing scheme. If the probability of correctly initialising a qubit is P_i then the probability of correctly initialising N qubits is P_i^N. Clearly if $P_i < 1$ this introduces an error with a probability which rapidly grows as the number of qubits in the input state is increased. Thus, deterministic input state preparation is an important prerequisite for scalability. For example, the promising scheme for linear optics quantum computing proposed by Knill, Laflamme, and Milburn[82] requires single photon sources capable of supplying on-demand photons into well-defined optical modes. More recently, there have been several proposed protocols to reduce the resource overhead required to build an optical computer via the use of many-qubit entangled input states known as cluster states[83, 84, 85]. Although the use of such

cluster states simplifies the operations required to implement computing processes, the creation of these states still requires the ability to initialise photons on-demand in well-defined states.

There has been much experimental progress on few-qubit gates using probabilistic sources, such as optically pumped parametric down-conversion crystals[86, 87, 88, 89]. However, these sources are governed by Poissonian statistics which introduces an inherent error-rate due to multi-photon emission, precluding systems of many gates.

There exists a range of possible triggered single photons sources, including molecules[90, 91], trapped ions[92], and colour centers in diamond[93, 94]. The work presented here uses a single semiconductor QD[95]. The use of QDs is particularly promising as they can be integrated directly with semiconductor waveguide devices and take advantage of well developed industrial semiconductor processing technologies.

In this chapter, an all-semiconductor photonic controlled-NOT (CNOT) gate, operating with single photons, is presented. This work is the first demonstration of an optical two-qubit gate operating with a QD single photon source. In addition, the light-source, gate circuitry, and detectors are all realised with semiconductor technology. As such, this work represents a significant advancement towards the creation of a fully integrated system for scalable optical quantum computing.

First the gate operation, and its implementation using optical waveguide circuitry, is introduced. The emission properties of the photon source are then presented. The gate operation is analysed and the main factors affecting the performance are discussed. Feasible improvements, which in the near future will allow further development of this solid-state optical quantum computing platform, are also discussed.

7.2 The CNOT gate

The CNOT gate is the simplest two-qubit gate and an important building block for quantum computing. When combined with single qubit opera-

tions, which in optical computing can be achieved simply by passing photons through waveplates to induce phase rotations, the CNOT gate allows mapping between any two states in the available Hilbert space. Multiple CNOT gates can construct a universal gate capable of performing any quantum operation.

7.2.1 NOT operation

In contrast to bits, qubits can be in superposition states, which have a mixture of components from each of the possible basis states. In this work, the qubits have two possible basis states, $|0\rangle$ and $|1\rangle$, so the quantum state of each qubit is given by

$$\Psi = \alpha|0\rangle + \beta|1\rangle \equiv \begin{bmatrix} \alpha \\ \beta \end{bmatrix} \tag{7.1}$$

with $\alpha^*\alpha + \beta^*\beta = 1$. The NOT operation interchanges the places of the basis state components such that

$$\mathbf{NOT}\{\alpha|0\rangle + \beta|1\rangle\} = \alpha|1\rangle + \beta|0\rangle. \tag{7.2}$$

The NOT operation can be represented in matrix form, where $\mathbf{X}$ denotes the NOT operator , as

$$\mathbf{X}\Psi = \begin{bmatrix} 0 & 1 \\ 1 & 0 \end{bmatrix} \begin{bmatrix} \alpha \\ \beta \end{bmatrix} = \begin{bmatrix} \beta \\ \alpha \end{bmatrix}. \tag{7.3}$$

7.2.2 CNOT operation

The CNOT gate requires a two-qubit input state comprised of a control and target qubit, denoted Ψ_C and Ψ_T respectively, and performs the NOT operation on Ψ_T conditional on the value of Ψ_C. To investigate the effects

of the quantum CNOT operation, consider the two input qubits,

$$\begin{aligned}\Psi_C &= \alpha_C|0\rangle + \beta_C|1\rangle \\ \Psi_T &= \alpha_T|0\rangle + \beta_T|1\rangle.\end{aligned} \tag{7.4}$$

The two-qubit input state for the CNOT gate can then be written as

$$|\Psi_C\Psi_T\rangle = \alpha_C\alpha_T|0\rangle|0\rangle + \alpha_C\beta_T|0\rangle|1\rangle + \beta_C\alpha_T|1\rangle|0\rangle + \beta_C\beta_T|1\rangle|1\rangle. \tag{7.5}$$

It is useful to recast the input state in terms of the two-qubit basis states, $|00\rangle, |01\rangle, |10\rangle, |11\rangle$. The input state is then given by

$$\Psi^{\text{in}} = a|00\rangle + b|01\rangle + c|10\rangle + d|11\rangle \equiv \begin{bmatrix} a \\ b \\ c \\ d \end{bmatrix}, \tag{7.6}$$

where $a = \alpha_C\alpha_T$, $b = \alpha_C\beta_T$, $c = \beta_C\alpha_T$, and $d = \beta_C\beta_T$. The action of the CNOT operation can then be represented in matrix form, with $\mathbf{C}$ denoting the CNOT operator, as

$$\mathbf{C}\Psi^{\text{in}} \equiv \begin{bmatrix} 1 & 0 & 0 & 0 \\ 0 & 1 & 0 & 0 \\ 0 & 0 & 0 & 1 \\ 0 & 0 & 1 & 0 \end{bmatrix} \begin{bmatrix} a \\ b \\ c \\ d \end{bmatrix} = \begin{bmatrix} a \\ b \\ d \\ c \end{bmatrix}. \tag{7.7}$$

In principle, the CNOT gate can operate on any superposition state, however the simplest way of characterising the gate operation is with the logical basis states:

$$\Psi^{\text{in}} = |\Psi_C\Psi_T\rangle = |00\rangle, |01\rangle, |10\rangle, |11\rangle. \tag{7.8}$$

Substitution of these states into equation 7.7 shows that the effect of the CNOT gate is to flip the state of Ψ_T if $\Psi_C = 1$ and leave the state unchanged

if $\Psi_C = 0$.

For an ideal CNOT gate the truth table is the same as the operation matrix, **C**, as each input maps to only one output. For an experimentally realised CNOT gate the truth table can be obtained by measuring the probability of each output state for each of the four input states. Due to gate errors, it is possible that each input state can map to more than one output state, so each truth table element must be normalised by the total intensity of all the output states corresponding to the same input state.

7.3 CNOT operation with a waveguide network

The CNOT circuitry is a direct implementation of that proposed by Ralph *et al.*[96]. A detailed explanation of the operation of the waveguide network can be found in reference [96], however an outline of the operating principles is included here to aid understanding of the experimental results.

7.3.1 Optical circuitry

The optical circuitry is realised using a silica-on-silicon waveguide, shown in figure 7.1a. The waveguides are designed by Dave Ellis and manufactured by a commercial company. Light is guided along the optical modes created by a refractive index contrast between different doping concentrations in the silica layer. The circuit uses directional couplers to perform the function of beamsplitters. Directional couplers bring two optical modes close together such that evanescent coupling occurs between them. The coupling strength and time are controlled by the spacing between the modes and the length of the coupler. By careful selection of these properties a directional coupler can act as a beamsplitter, such that light entering from an input is split between the two outputs with a known ratio. The network presented in this chapter consists of $\frac{1}{2}$ and $\frac{1}{3}$ couplers, as shown schematically in figure 7.1b where each coupler is labeled with its effective reflectivity.

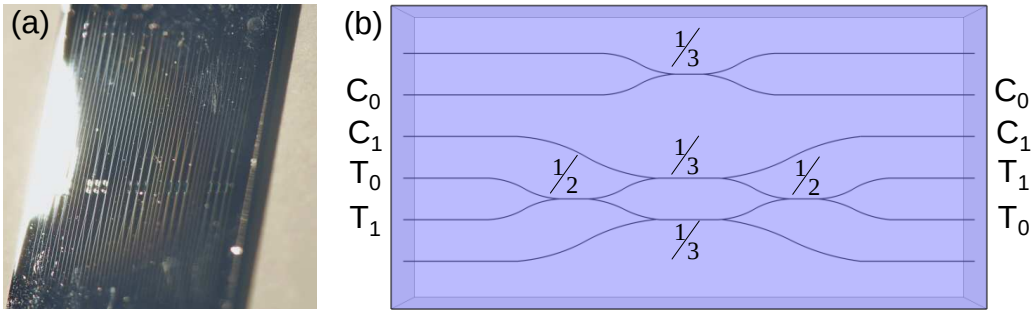

Figure 7.1: Optical circuitry. (a) Photograph of the waveguide chip, intense illumination allows the waveguides to be seen. (b) Schematic diagram of waveguide network, the path inputs and outputs are labeled with the corresponding state and the couplers are labeled with their reflectivity.

In addition, isolated test couplers, nominally identical to those which make up the network, are fabricated adjacent to the CNOT circuitry. These allow the coupling ratios, which depend on the physical dimensions of the coupler and are thus defined during fabrication, to be experimentally verified. Measurements of the coupler reflectivities were performed by Dave Ellis. For each of the two kinds of coupler, laser light was coupled into an input and the relative intensity of the two outputs measured to find the effective reflectivity. At the source wavelength, the coupling ratios in the network used for this work are $R_{1/3} = 0.345$ and $R_{1/2} = 0.495$.

7.3.2 Operating principle

The waveguide network functions with path-encoded qubits, where the state of the qubit is mapped onto the path it takes through the waveguide. As shown in figure 7.1b, each qubit has two input and two output paths labeled C_i and T_i for the control and target qubits respectively. The subscripts ($i =$ 0 or 1) indicate the basis state of the qubit to which the paths correspond. Here we consider only inputs composed from logical basis states, given in equation 7.8, where each qubit has a single photon in one path and zero photons in the other. For example, to input the state $|\Psi_C \Psi_T\rangle = |00\rangle$ two photons must simultaneously enter the waveguide with one in path C_0 and

one in path T_0.

The two $\frac{1}{2}$ couplers form a Mach-Zehnder interferometer (MZI), the $\frac{1}{3}$ coupler in the upper MZI arm allows interaction between the two qubits, and the other two $\frac{1}{3}$ couplers serve to balance the output intensities. The gate relies on single photon interference through the MZI and two-photon interference between the two qubit photons.

The MZI is balanced such that a single target photon, in the absence of any interaction with the control qubit, exits the waveguide in the same state that it enters. Two photon interference between the control and target qubits in the upper arm of the MZI has the effect of a π phase shift, resulting in the target qubit swapping modes and leaving the MZI in the opposite state to which it entered. Thus, the NOT operation is performed on Ψ_T if $\Psi_C = 1$, and the target state is unchanged if $\Psi_C = 0$, as required.

The CNOT gate operates in the coincidence basis, such that only events where photons are simultaneously detected in both a target and control output path are considered. This is achieved in practice via time resolved correlation measurements between control and target output paths, where coincidence events are recorded as a function of the time interval, τ, between the two photons. The gate operation is fully assessed with 16 correlation measurements, as for each of the 4 input states there are 4 possible output states.

7.3.3 Expected correlations

The time-averaged output intensity into each of the coincidence states can be calculated from the individual intensities expected from each output path. The individual intensities at each output path are calculated for each input state by considering all possible trajectories the two photons can take as they traverse the waveguide. Table 7.1 shows the probability of a photon exiting in each output path for every input path pair.

The time-averaged probability of a correlation event between any two outputs is then calculated from the product of the individual output probabilities. Table 7.2 shows the probability of measuring a correlation between

		Output Path			
		C_0	C_1	T_0	T_1
Input Paths	C_0, T_0	$\frac{1}{3}$	$\frac{1}{3}$	$\frac{1}{3}$	0
	C_0, T_1	$\frac{1}{3}$	$\frac{1}{3}$	0	$\frac{1}{3}$
	C_1, T_0	0	$\frac{2}{3}$	$\frac{2}{3}$	$\frac{1}{3}$
	C_1, T_1	0	$\frac{2}{3}$	$\frac{1}{3}$	$\frac{2}{3}$

Table 7.1: Probability of a photon being in a given output path for each of the four input path pairs required to encode the four logical input states.

the four possible output path pairs for each of the input path pairs.

		Output Paths			
		C_0, T_0	C_0, T_1	C_1, T_0	C_1, T_1
Input Paths	C_0, T_0	$\frac{1}{9}$	0	$\frac{1}{9}$	0
	C_0, T_1	0	$\frac{1}{9}$	0	$\frac{1}{9}$
	C_1, T_0	0	0	$\frac{4}{9}$	$\frac{2}{9}$
	C_1, T_1	0	0	$\frac{2}{9}$	$\frac{4}{9}$

Table 7.2: Probability of a coincidence event between the output path pairs, with any value of τ, for each of the input path pairs.

Only those events in which $|\tau|$ is within a 1.95 ns window centered on zero are used to assess the gate operation, as these events correspond to when two photons from the same excitation cycle enter the waveguide simultaneously. The probability of a coincidence event in this window between output pairs for each input pair is shown in table 7.3. By comparison between table 7.3 and the CNOT operation matrix in equation 7.7, it can be seen that the waveguide network implements the CNOT operation with a probability of $\frac{1}{9}$.

7.3.4 Experimental operation

So far the operation of an ideal CNOT gate has been discussed, however in reality experimental imperfections introduce errors which affect the gate operation. The most significant sources of error are the visibility of single-photon interference, $V^{(1)}$, the visibility of two-photon interference, $V^{(2)}$, and

		Output Paths			
		C_0, T_0	C_0, T_1	C_1, T_0	C_1, T_1
Input Paths	C_0, T_0	$\frac{1}{9}$	0	0	0
	C_0, T_1	0	$\frac{1}{9}$	0	0
	C_1, T_0	0	0	0	$\frac{1}{9}$
	C_1, T_1	0	0	$\frac{1}{9}$	0

Table 7.3: Probability of a coincidence event, involving two photons from the same input state, in each output pair for every input pair.

the non-ideal coupler ratios inside the waveguide network. Whilst multi-photon emission from the QD is also a potential source of error, the probability of a multi-photon emission event from the emitter used in this work is so low (see 7.4.3) that it can be neglected. In addition, as the gate is measured in the coincidence basis, emitter and detector inefficiencies do not cause errors but serve only to reduce the rate at which correlation events are accumulated. In this subsection the effects of imperfect single-photon and two-photon interference on the gate operation are discussed.

Single-photon interference is a consequence of wave-particle duality. When a single photon encounters a beamsplitter it does not exit from a single output, as would be expected for a particle. It instead exits from both outputs simultaneously in a superposition between the two possible output paths, as would be expected for a wave. However, if the output from which the photon leaves is measured, for example by coupling each output into one of two APDs, the photon will only ever be detected in one exit path at any one time; the act of measuring the outcome from the beamsplitter collapses the superposition wavefunction into one of the eigenstate paths. The MZI in the waveguide network uses this property of single photons to ensure their correct trajectory through the optical circuitry. The single target photon enters the first $\frac{1}{2}$ coupler and leaves in a superposition between the two arms of the MZI. At the second $\frac{1}{2}$ coupler the two paths are combined and interference occurs between the two portions of the superposition wavefunction. If the two arms of the MZI are phase-matched then destructive interference occurs between the portions of the wavefunctions which would lead to the photon

changing path, and constructive interference occurs between the portions of the wavefunctions which result in the photon leaving in the same path. For example, if the photon is initially in input path T_0 the interference between the portions of the wavefunction in each MZI arm results in the photon always leaving the MZI in the T_0 output path. The operation of the MZI is characterised by $V^{(1)}$, which is the probability that photons entering the MZI leave in the same path which they entered. The value of $V^{(1)}$ is largely due to how well phase-matched the two arms of the MZI are and is thus a property of the waveguide, which is defined during fabrication. If $V^{(1)} < 1$ then the operation of the MZI is non-ideal, meaning that target photons can leave from the wrong path due to incorrect single-photon interference.

Two-photon interference can occur if two indistinguishable photons meet at a beamsplitter. In the absence of any interference effects there are four possible outcomes, two with the photons leaving from the same output and two with the photons leaving from different outputs. However, if the wavefunctions of the two photons are indistinguishable then destructive interference occurs between the two outcomes which result in photons leaving from different outputs and the two photons will always leave the beamsplitter from the same output. The two-photon interference process which occurs at the $\frac{1}{3}$ coupler in the upper arm of the MZI is characterised by $V^{(2)}$; if $V^{(2)} = 1$ then the photons always leave in the same path, if $V^{(2)} = 0$ then there is no interference and the probability that the photons leave in the same path is reduced to $\frac{1}{2}$. The value of $V^{(2)}$ is a property of both the waveguide and the emitter, as it depends on both the spatial overlap of the photons inside the waveguide and on the indistinguishability of the photons. As the interference takes place inside a directional coupler, it is the temporal properties and distinguishability of the photons which imposes the limit on $V^{(2)}$. The interaction of the exciton with the solid-state environment leads to decoherence, limiting the degree of indistinguishability of the emitted photons. If $V^{(2)} < 1$ then interaction between the control and target qubits is not guaranteed, which causes errors when the input control qubit has state $\Psi_C = 1$.

When these parameters are taken into account the CNOT matrix opera-

tor, **C**, given in equation 7.7 becomes

$$\mathbf{C} = \begin{bmatrix} V^{(1)} & 1-V^{(1)} & 0 & 0 \\ 1-V^{(1)} & V^{(1)} & 0 & 0 \\ 0 & 0 & 2(1-V^{(2)})+(1-V^{(1)}) & V^{(1)} \\ 0 & 0 & V^{(1)} & 2(1-V^{(2)})+(1-V^{(1)}) \end{bmatrix} \tag{7.9}$$

and the corresponding truth table for the CNOT gate is given in table 7.4

		Output State			
		$\|00\rangle$	$\|01\rangle$	$\|10\rangle$	$\|11\rangle$
Input State	$\|00\rangle$	$V^{(1)}$	$1-V^{(1)}$	0	0
	$\|01\rangle$	$1-V^{(1)}$	$V^{(1)}$	0	0
	$\|10\rangle$	0	0	$\frac{2(1-V^{(2)})+(1-V^{(1)})}{2(1-V^{(2)})+1}$	$\frac{V^{(1)}}{2(1-V^{(2)})+1}$
	$\|11\rangle$	0	0	$\frac{V^{(1)}}{2(1-V^{(2)})+1}$	$\frac{2(1-V^{(2)})+(1-V^{(1)})}{2(1-V^{(2)})+1}$

Table 7.4: Truth table for waveguide implemented CNOT gate, taking into account the visibility of single photon and two-photon interference.

To understand the origins of equation 7.9 it is necessary to consider the combined effects of $V^{(1)}$ and $V^{(2)}$. In order to do this it is useful to consider matrix **C** as four 2×2 submatrices. The top right and bottom left submatrices are trivial, as the CNOT operation does not change the state of the control qubit. All elements of the top right submatrix are zero, as when $\Psi_C = |0\rangle$ there are no coincidences involving $\Psi_C = |1\rangle$. Similarly for the bottom left submatrix; no coincidences involving $\Psi_C = |0\rangle$ occur when $\Psi_C = |1\rangle$.

The top left submatrix depends only on $V^{(1)}$, as for these elements $\Psi_C = |0\rangle$ and the two qubit photons do not interfere with each other. The on-diagonal elements of the top left submatrix correspond to cases where the target qubit is unchanged by the gate. This happens so long as the target qubit correctly exits the MZI, which occurs with probability $V^{(1)}$. The off-diagonal elements of the top left submatrix correspond to cases where the target photon leaves the MZI from the incorrect path, which occurs with probability $1 - V^{(1)}$.

The bottom right submatrix depends on both $V^{(1)}$ and $V^{(2)}$. The on diagonal elements have contributions from two mechanisms. Cases where two-photon interference results in both photons merging into the same path reduce the value of these elements. When two-photon interference does not occur, which happens with probability $(1 - V^{(2)})$ the resulting error contributes to these elements. In addition, events when the target qubit ends up in the wrong output path due to imperfect single-photon interference, which occurs with probability $1 - V^{(1)}$, also contribute to these elements. The off diagonal elements rely on the target qubit leaving the MZI in the correct path and so are given by $V^{(1)}$.

7.4 Photon source

The photon source is a single InAs QD embedded inside a 1.5 μm diameter pillar microcavity. QDs are well suited as single photon emitters due to their discrete energy level structure and easy integration with semiconductor optical cavities. In the work presented here, the photons are emitted by the $|X_1\rangle \rightarrow |0\rangle$ transition. Embedding the QD inside a microcavity yields two advantages. Purcell enhancement[21] reduces the radiative lifetime, relative to the coherence time, of excitons within the QD. This increases the degree of indistinguishability of the emitted photons leading to an increase in $V^{(2)}$, which as can be seen from table 7.4 improves the performance of the gate. In addition, collimation of the emission due to coupling between the transition and the fundamental cavity mode significantly increases collection efficiency.

The planar structure of the microcavity, grown via molecular beam epitaxy, consists of 17 (25) periods of GaAs/AlGaAs distributed Bragg reflector above (below) a one-wavelength thick GaAs cavity centered on a layer of self-assembled InAs quantum dots. Reactive ion etching was used to define pillars, examples of which can be seen in Figure 7.2.

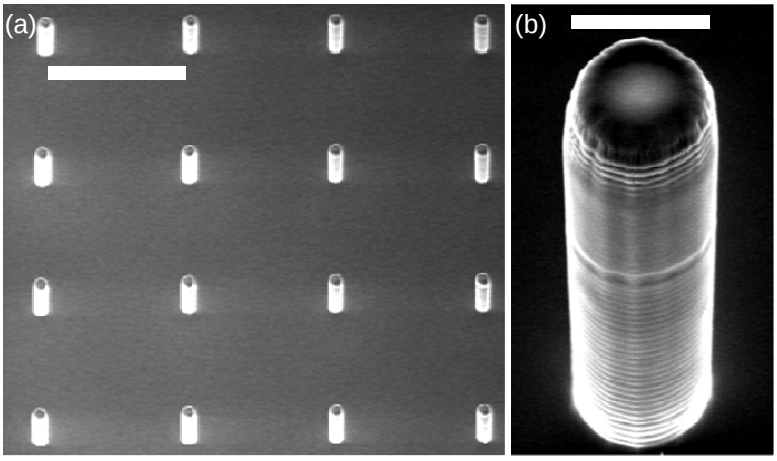

Figure 7.2: SEM images of micropillar cavities. (a) Section of an array of pillars, scale bar is 20μm. (b) Single SEM pillar of the nominal size used in the CNOT measurement, scale bar is 1.5μm.

7.4.1 Initialisation of the two-photon input state

The pillar is cooled to a temperature of $\sim$ 5 K by a continuous flow of liquid helium. The QD is optically pumped by a 1364meV pulsed mode-locked laser operating with a repetition frequency of 80Mhz, which drives the $|0\rangle \rightarrow |X_1\rangle$ transition via the quasi-resonant excitation scheme described in section 2.5. To ensure indistinguishability of the emitted photons, polarisation filtering is used to select emission from just one of the exciton eigenstates. The quasi-resonant excitation scheme maps the polarisation of the excitation photon onto the spin of the resulting exciton, as discussed in section 6.2. This allows selective excitation of a single eigenstate, increasing the internal efficiency of the source relative to other excitation schemes that excite both of the eigenstates.

The CNOT input state requires two photons, one for each of the control and target qubits, both of which are emitted from the same QD. The experimental configuration used to achieve this is shown in figure 7.3. An unbalanced Michelson interferometer is used to split each pulse from the pump laser into two pulses separated by 1.95ns. Thus each repetition of the laser excites the QD twice in quick succession. The resulting QD emission

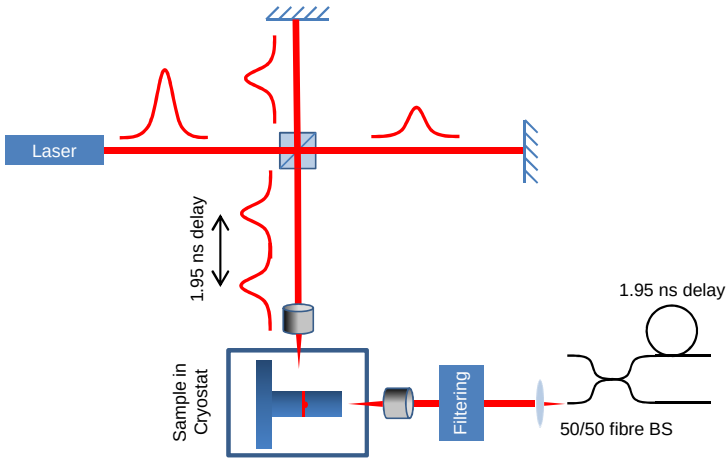

Figure 7.3: Configuration used to generate the two-photon input state.

is spectrally filtered to select photons from the $|X_1\rangle \rightarrow |0\rangle$ transition, which are coupled into a $\frac{1}{2}$ fiber beamsplitter. A 1.95 ns delay is placed in one of the beamsplitter output ports. If the first photon takes the delayed path and second the un-delayed path the two photons leave the output ports simultaneously, as required for the CNOT input state. This method has a $\frac{1}{4}$ probability of creating the desired state, however in principle two synchronised single photon sources could allow deterministic state preparation.

7.4.2 Source characterisation

In order to benefit from the improved indistinguishability and increased collection efficiency associated with embedding the emitter inside a cavity, the exciton transition of the QD must be coupled to the HE_{11} cavity mode. This requires the wavelength of the emission and the position of the QD to match that of the mode. The self-assembled Stranski-Krastanov growth of the quantum dots allows no lateral control of the QD position and results in an ensemble of QD sizes and thus emission wavelengths. In addition to being coupled to the HE_{11} mode, the exciton transition must emit at a wavelength within the range for which the optical circuitry is designed. For a given planar structure, the wavelength of the HE_{11} mode depends on the diameter of

the pillar. To increase the yield of samples with appropriately coupled quantum dots, and to accommodate processing variations in the pillar diameter, each device consists of 800 pillars with nominal design diameters of 1.00 – 2.75 μm.

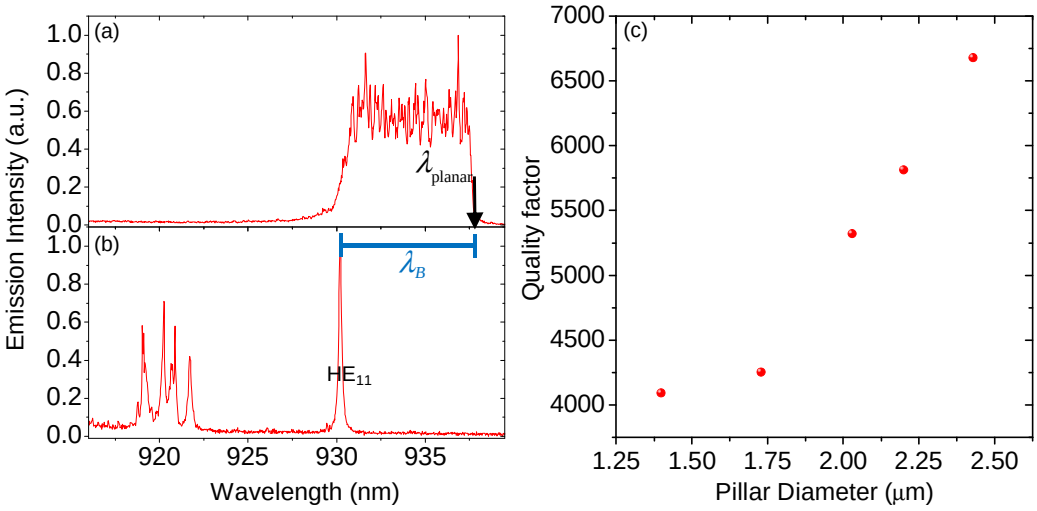

Figure 7.4: The pillars are characterised using PL spectroscopy. (a) PL emission from a large unpatterned area of the sample shows the planar cavity. The planar cavity cut-off wavelength, labeled λ_{planar}, gives the wavelength of vertical emission. (b)μ-PL spectrum from a single pillar microcavity with a diameter of 1.5μm. The HE_{11} mode, which collimates the vertical emission, is labeled. The blueshift, λ_B, of the HE_{11} mode relative to the vertical emission from the planar cavity is due to the lateral confinement provided by the pillar walls and is dependent on the pillar diameter.(c) Q-factor as a function of pillar diameter for the pillars used in this work.

The pillars are characterised using μ-PL measurements, from which the wavelength of the HE_{11} mode, λ_{11}, can be measured. Figure 7.4 shows μ-PL measurements from an unetched planar region of the wafer and from a microcavity with diameter $\sim 1.5\mu$m. The wavelength of the vertical emission from the planar cavity, λ_{planar}, is higher than λ_{11} due to a blueshift of the mode caused by the lateral confinement of the microcavity. The blueshift, given by $\lambda_B = \lambda_{\text{planar}} - \lambda_{11}$, can be used to calculate the actual diameter of

a pillar from

$$D = \sqrt{\frac{18.7}{\lambda_B}}, \tag{7.10}$$

where D is the diameter in μm and λ_B is in units of nm. This relationship has been empirically demonstrated by David Unitt[97] , and is consistent with SEM measurements. The actual diameter of the microcavities is typically smaller than the nominal design diameter due to lateral etching which occurs as the pillars are defined. The pillar used in this chapter had a nominal design diameter of 2.5 μm, however SEM images of the pillar yield a diameter of ~ 1.5 μm due to lateral etching effects. This measured diameter is consistent with the measured blueshift of 7.685 nm, which from equation 7.10 gives a diameter of 1.56 μm.

The quality factor, Q, is given by

$$Q = \frac{\lambda_{11}}{\Delta\lambda}, \tag{7.11}$$

where $\Delta\lambda$ is the full width at half maximum of the HE_{11} mode, and can be measured experimentally by fitting the HE_{11} mode with a Lorentzian peak. Figure 7.4c shows Q, averaged over several randomly chosen pillars of each nominal size, as a function of diameter for the sample used in this work.

The pillar used in this work had a diameter of 1.5 μm and a quality factor of $Q \sim 9000$. This pillar was selected for its exceptionally high quality factor which, as can be seen from figure 7.4c, was significantly higher than average for its diameter. The pillar contains a QD with a $|X_1\rangle \rightarrow |0\rangle$ transition that emits at a wavelength of 931 nm, which is resonant with the HE_{11} cavity mode of the pillar. Time resolved spectroscopy of the transition, shown in figure 7.5a, shows that the radiative lifetime of excitons within the QD is $\tau_R = 106$ ps. A measurement of the transition linewidth using etalon spectroscopy is shown in figure 7.5b. From the width of a Lorentzian fit to the data a coherence time of $\tau_C = 148$ ps is extracted.

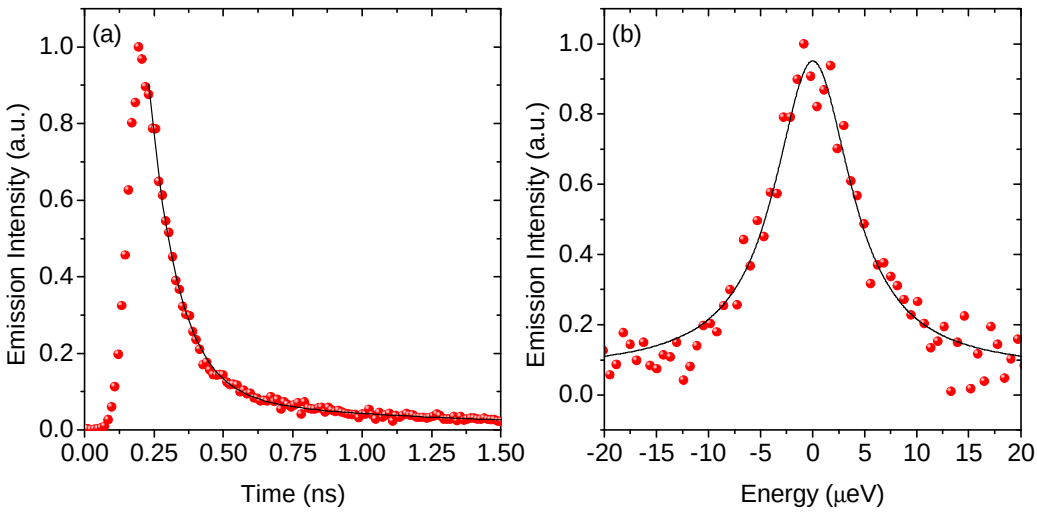

Figure 7.5: Measurements of radiative lifetime and coherence time. (a) Emission intensity of the exciton transition as a function of time. The solid black line is a double exponential fit to the data, from which a radiative lifetime of $\tau_R = 106$ ps is extracted. (b) Emission intensity of the exciton transition as a function of energy, measured using a piezo controlled etalon. The energy is offset by the mean emission energy. The black solid line shows a Lorentzian fit to the data, from which a coherence time of $\tau_C = 148$ ps is extracted.

7.4.3 Indistinguishable single photon emission

The photon source must meet two requirements: (1) single photon emission is necessary, as multiple photons simultaneously entering the control or target paths prevents correct gate operation; (2) the two input photons must have a high degree of indistinguishability in order to maximise the two-photon interference between the target and control qubits.

As described in section 3.3.5, measurements of the source's 2nd-order autocorrelation function, $g^{(2)}(\tau)$, were used to confirm the single photon nature of the emission. Figure 7.6b shows $g^{(2)}(\tau)$ for the pillar used in this work when the QD is excited directly by a pulsed laser operating at 80 MHz. This measurement yields $g^{(2)}(0) = 0.013 \pm 0.004$, indicating that under standard pulsed excitation there is a significant suppression of multi-photon emission. Figure 7.6d shows $g^{(2)}(\tau)$ when the pillar is excited twice in quick succession under the conditions described in section 7.4.1. From this measurement it is possible to obtain the probability of multi-photon emission in either of the two emission events required to create the CNOT input state, g. The residual between the data and a double Lorentzian fit to the peaks at $\tau = \pm 1.95$ nm yields $g = 0.0063 \pm 0.0005$, confirming the single photon nature of the photon source under CNOT operation conditions. Both of these measurements were performed using a $\frac{1}{2}$ waveguide coupler nominally identical to those inside the CNOT circuitry.

The visibility of two-photon interference, $V^{(2)}$, is measured using a Hong-Ou-Mandel[98] (HOM) interferometer, implemented using a 50/50 fibre beam-splitter and a $\frac{1}{2}$ waveguide coupler as shown in figure 7.7a. As the spatial overlap of the paths inside the waveguide coupler is excellent, the value of $V^{(2)}$ is limited by the distinguishability of the photons. This is dependent on the ratio τ_C/τ_R and thus an inherent property of the source under a given excitation regime. Figure 7.7b shows the HOM correlation. The cluster of five peaks centered at $\tau = 0$, labeled A-E, correspond to events where both detected photons are from the same excitation cycle. The peaks within each cluster are separated by $\tau_{\text{p}} = 1.95$ ns, which is the time interval between the two photons emitted each excitation cycle. If the first photon takes the un-

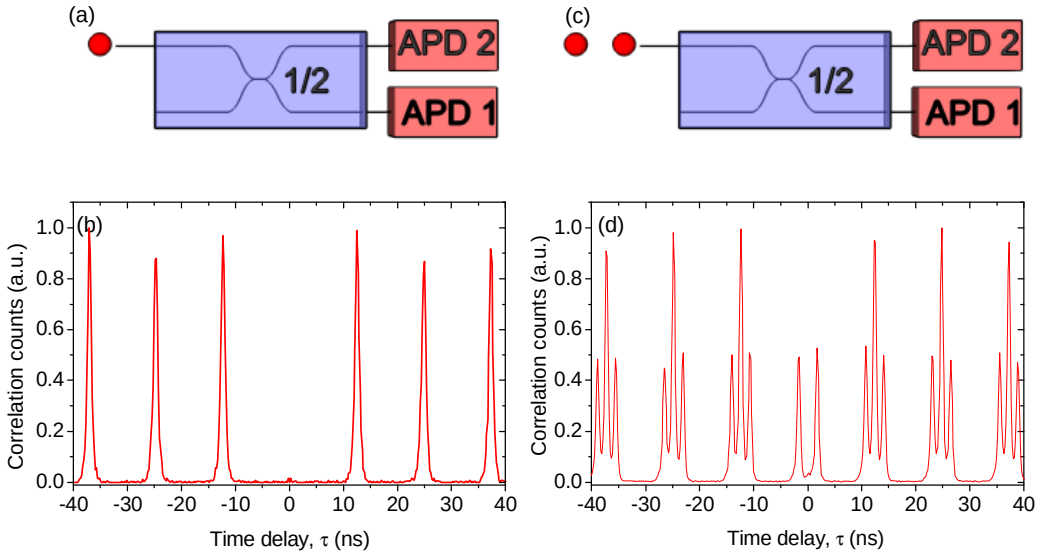

Figure 7.6: Confirmation of single photon emission. (a)-(b) Pulsed second-order autocorrelation measurement yields a $g^{(2)}(0) = 0.013 \pm 0.004$. (c)-(d) Pulsed autocorrelation measurement under the excitation conditions for CNOT state preparation yields a probability of multi-photon emission in either emission event of $g = 0.0063 \pm 0.0005$.

delayed path and the second takes the delayed path they arrive at the APDs separated by $2\tau_{\mathrm{p}}$, resulting in peaks A and E. If both photons take the same path into the waveguide they arrive at the APDs separated by τ_{p}, resulting in peaks B and D. If both photons enter the waveguide simultaneously they can interfere at the $\frac{1}{3}$ coupler in the upper MZI arm. Two-photon interference causes both photons to leave the coupler in the same output path[98], preventing a photon being simultaneously detected at each APD if $V^{(2)} = 1$. The relative area of peak C compared to that of peaks B and D is used to calculate $V^{(2)} = 1$, via

$$V^{(2)} = 1 - \frac{\Omega_C}{\frac{1}{2}\left(\Omega_B + \Omega_D\right)} \tag{7.12}$$

where Ω_i corresponds to the area of peak i. A value of $V^{(2)} = 0.72 \pm 0.05$ is obtained for the pillar used in this work. This is comparable with the highest $V^{(2)}$ reported for single photon semiconductor sources.

7.5 Demonstration of an optical CNOT gate

7.5.1 Experimental configuration

The waveguide is mounted into a coupling rig to allow fibre arrays to be butt-coupled to the input and output paths, with single-mode fiber used to couple into the waveguide and multi-mode fiber used to collect from the waveguide outputs. The two-photons for the input state are created as described in section 7.4.1. One photon is coupled into a target input path and the other is coupled into a control input path, which allows any of the basis state inputs given in equation 7.8 to be realised. A diagram of the experimental configuration is shown in figure 7.8.

For each input state, four time-resolved correlation measurements are acquired simultaneously between control and target output paths, one for each of the possible basis states. Analysis of these correlation measurements allows the operation of the CNOT gate to be assessed.

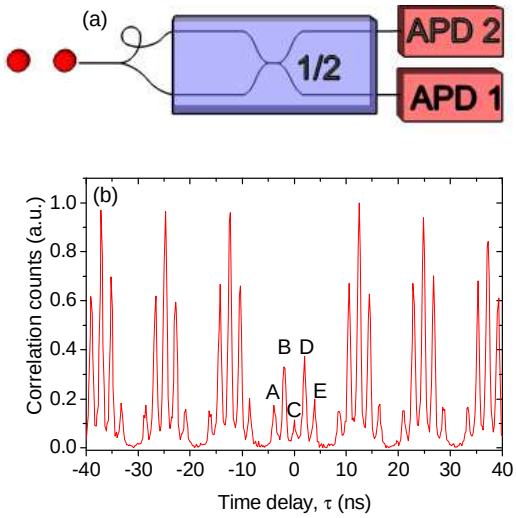

Figure 7.7: Measurement of photon indistinguishability. (a) Hong-Ou-Mandel interferometer implemented with a 50/50 fibre beamsplitter and a $\frac{1}{2}$ directional coupler. A delay fibre is inserted before one of the waveguide inputs to allow consecutive photons to meet and interfere at the coupler. (b) A pulsed two-photon interference measurement, under the excitation conditions used for the CNOT input state preparation. The number of counts in each of the labeled peaks, integrated over the central 600 ps of each peak, are $A = 170$, $B = 354$, $C = 100$, $D = 375$, $E = 183$. This gives a visibility of two-photon interference of $V^{(2)} = 0.72 \pm 0.05$.

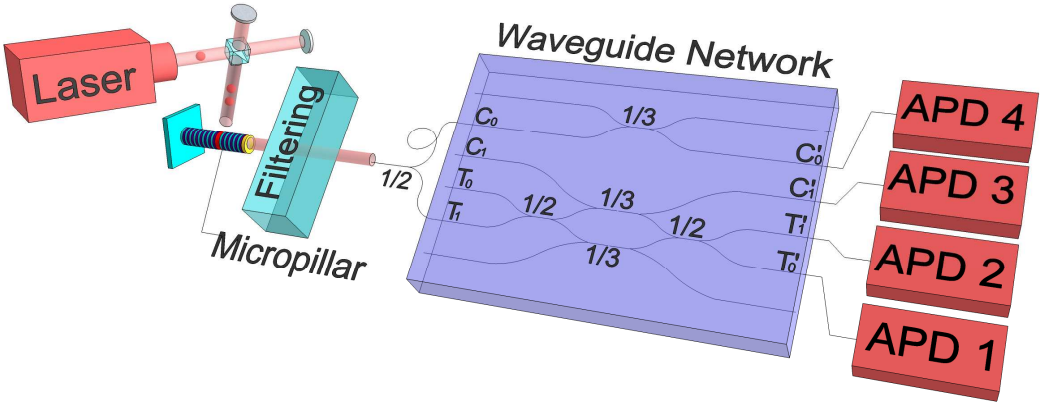

Figure 7.8: Experimental configuration for measurement of the CNOT gate. An unbalanced Michelson interferometer and a delay line allow the creation of the two-photon input state. The input state is selected by setting the path that each of the photons is coupled into. Each waveguide output is coupled into an APD via multi-mode fibre, this allows time-resolved correlation measurements to be acquired.

7.5.2 Correlation measurements

The experimentally obtained correlation measurements are shown in figure 7.9. From the relative areas of the peaks in the $\langle 00|00\rangle$ and $\langle 00|01\rangle$ correlations a visibility of single-photon interference of $V^{(1)} = 0.97$ is extracted. The $\langle 10|10\rangle$ and $\langle 11|11\rangle$ correlations show two photon interference measurements similar to the Hong-Ou-Mandel measurement shown in figure 7.7, however the suppression of the central $\tau = 0$ peak is determined not only by the value of $V^{(2)}$ but also by other properties of the waveguide network, specifically the non-ideal coupler reflectivies and non-unity value of $V^{(1)}$. To extract the value of $V^{(2)}$ within the waveguide network the expected correlation measurements are modeled. The predicted form of the correlation curves, which were calculated by Adrian Chan, are shown in figure 7.9 as solid black lines. These curves were calculated via consideration of all the possible paths that the photons can take through the waveguide network, with the probability of each path adjusted to account for the experimentally determined coupler reflectivities and single-photon interference visibility. The width of the peaks are obtained via a convolution with the combined detector response function

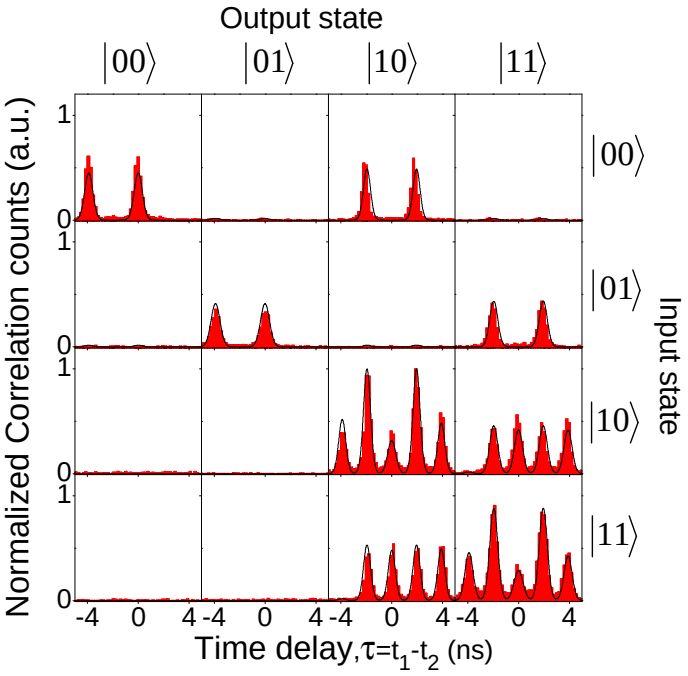

Figure 7.9: Correlation measurements used to assess the function of the CNOT gate. Each pane shows the measurement for a single input and output combination. Measured data is shown as filled red bars. The solid black curves show the predicted form of the correlations calculated as described in the main text. The peaks centered at $\tau = 0$ correspond to events when two photons entered the waveguide simultaneously and are used to construct the truth table.

of the two detectors involved in each correlation. For the $\langle 10|10\rangle$ and $\langle 11|11\rangle$ correlations the peaks at $\tau = 0$, which depend on two-photon interference effects, are calculated using a wavepacket overlap approach similar to that of Legero *et al.*[99, 51], in which the temporal properties of the photons and the waveguide imperfections are considered. The data agrees well with predicted curves calculated with the measured values of $V^{(1)}$, $R_{1/3}$, and $R_{1/2}$, and with a value for two-photon interference visibility of $V^{(2)} = 0.67$, which is consistent with the value obtained using an isolated $\frac{1}{2}$ coupler (see figure 7.7).

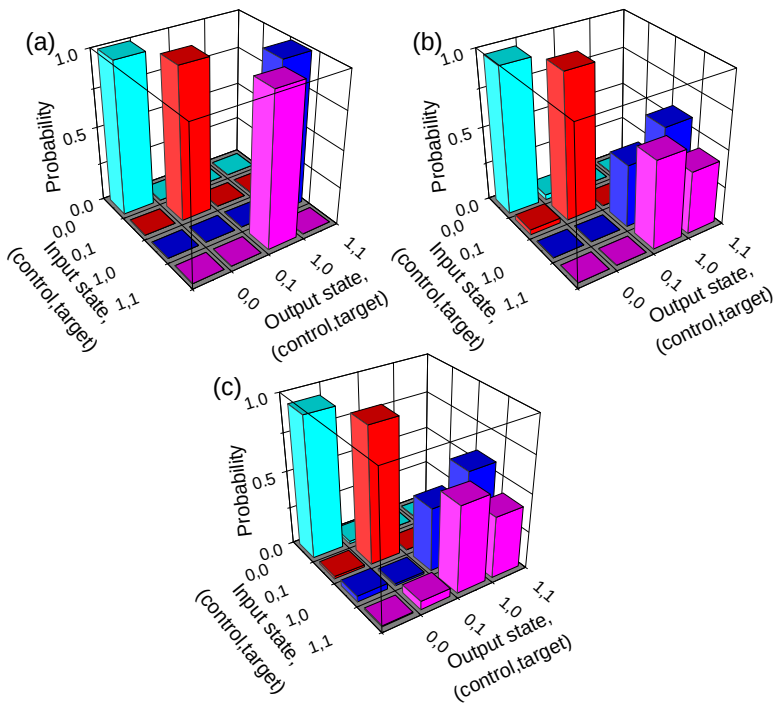

Figure 7.10: Truth tables (a) for an ideal CNOT gate, (b) calculated from the predicted correlation curves, for the CNOT gate realised experimentally, (c) for the measured CNOT gate operation.

7.5.3 Success probability

A truth table for the CNOT gate is constructed from the correlation measurements using the coincidence peaks (centered at $\tau = 0$), as those peaks correspond to events when the input state is correctly prepared. Figure 7.10 shows the measured truth table, along with a predicted truth table calculated using the experimentally realised values of $V^{(1)}$ and $V^{(2)}$, and the truth table of an ideal CNOT gate.

Each element of the measured truth table is given by the area of the coincidence peak in the corresponding correlation measurement, normalised by the total area of the coincidence peaks in all the correlation measurements for the same input state. As seen at the end of section 7.2.2, after this normalisation the elements give the probability of mapping between each input and output state. The success probability for an input state is given

by the truth table element in the associated row which corresponds to the correct output state.

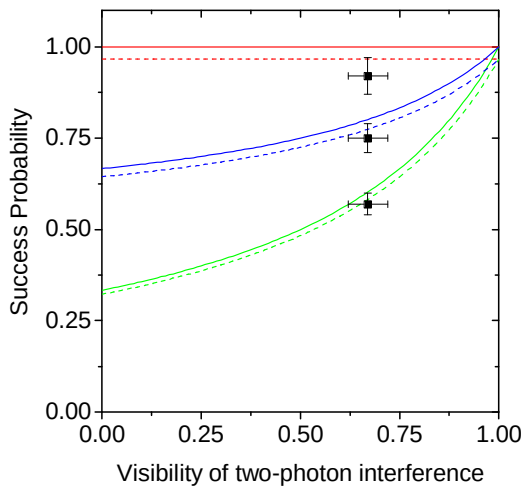

Figure 7.11: Success probability as a function of two-photon interference visibility for an ideal CNOT network (solid lines) and the experimentally realised network (dashed lines). The input states with $\Psi_C = 1$ are shown in green, those for input states with $\Psi_C = 0$ are shown in red. The average values across all inputs are shown in blue. The experimentally achieved values are plotted as black squares, with the errorbar length determined by Poissonian counting errors.

The predicted truth table is calculated from table 7.4. Note that this method of analysis neglects the effects of non-ideal coupler reflectivies. It is possible to include these effects by constructing the predicted truth table from the calculated curves shown in figure 7.9. This was done by Adrian Chan and the results vary by less than 1% from those obtained using the simpler analysis presented here.

Figure 7.11 shows the success probability as a function of $V^{(2)}$ for the case of an ideal CNOT waveguide (solid lines) and the experimentally realised waveguide with $V^{(1)} = 0.97$ (dashed lines). The experimentally achieved success probabilities are shown as black squares and are in good agreement with the calculated values. When the truth table is calculated from the area of the entire coincidence peak, integrated over a window of 1.95 ns, the success probability averaged over all inputs is 71%. Taking a narrower window of 0.6 ns increases the average success probability to 75% whilst preserving 60%

of the coincidence counts. In principle, performing the measurement using detectors with faster response times could further improve the measured success rate. However, it is clear that the key to improving the performance of the gate is to increase the value of $V^{(2)}$. The main factor limiting $V^{(2)}$ in this work is the degree of photon indistinguishability, which is largely determined by the ratio of the radiative decay time and coherence time, τ_C/τ_R, of the exciton within the QD.

The quasi-resonant excitation scheme used for this work results in residual decoherence caused by the interaction of the exciton with the solid-state environment. However, the use of coherent Raman excitation schemes[100, 101] can potentially lead to increased coherence time. In addition, recent resonance fluorescence measurements[102] have been shown to transfer the coherence properties of the excitation laser to the exciton photon, leading to coherence times which approach that of the driving laser.

7.6 Conclusion

An optical CNOT gate operating with single photons from an optically pumped QD has been demonstrated. The photon source has been characterised to confirm single photon emission and assess the degree of indistinguishability between the emitted photons. The gate performance has been analysed, revealing the visibility of two-photon interference to be the main limiting factor. This work is a demonstration of key principles required to develop a scalable platform for optical quantum computing. True single photon sources based on semiconductor materials offer the potential of deterministic state preparation in a miniturised package well suited for scaling with current fabrication techniques. The feasibility of such a scheme has been shown. The challenge is now to improve the efficiency of the photon sources and detectors and to increase the integration between the required components.

Extensions of this work include using multiple synchronised single photon sources to enable deterministic preparation of multi-photon input states. Also feasible with current technology is to modify the waveguide to accept

superposition input states. This could be achieved with the addition of extra Mach-Zehnder interferometers on the control and target inputs. The two output paths of each interferometer would become the two input paths for each of the control and target qubits. Variation of the phase difference between the arms of each interferometer would then allow control of the superposition states which traverse the gate.

Chapter 8

Conclusion

This thesis describes work towards the development of components for optical quantum computing using single semiconductor QDs. The neutral transitions have been studied in particular detail, both as a means to generate and interact with non-classical light states and in order to explore the potential of confined excitons as solid-state qubits.

Single QDs have been studied in two different device structures: diodes, which allow the application of large electric fields; and pillar microcavities, which enhance the temporal and coherence properties of the emitted photons via coupling between the neutral transitions and the cavity mode.

Methods of manipulating the energy structure of the neutral states involving the application of electric and magnetic fields have been investigated. This has resulted in a method for reducing the fine-structure splitting in QDs in order to allow entanglement between the two photons emitted from the neutral biexciton cascade to observed. In addition, a technique for the creation of an energy-tunable entangled photon emitter has been proposed and shown to be feasible with current technology.

The temporal properties of the neutral exciton state have also been investigated. This has allowed the implementation of a solid-state phase gate, via the application of a dynamic electric field to controllably vary the fine-structure splitting (FSS, s).

Finally, the neutral exciton transition has been used to generate indistin-

guishable single photons for use in an all-semiconductor photonic two-qubit gate. This represents an important step towards a fully integrated photonic quantum computing platform.

8.1 Summary of results

8.1.1 Emission of entangled photon pairs

Much of this thesis is concerned with the neutral biexciton cascade, as the two photons emitted by this process form an entangled photon pair. In the absence of any FSS these two photons are emitted into a Bell state, which is independent of time and so well suited to many applications which require a known input state, such as photonic logic circuits. However, finite FSS introduces a time evolving phase between the two entangled states. This necessitates the ability to temporally resolve the state in order to use the entanglement as a resource. The rate of the phase evolution is proportional to the magnitude of the FSS and for $|s|$ larger than a few μeV it becomes difficult to resolve. Therefore it is desirable to be able to reduce the value of $|s|$.

An electric field, applied parallel to the sample growth direction, has been used to tune the value of $|s|$. The planar structure of the diodes is designed to allow a large range of electric field to be applied whilst preserving the optical activity of the QDs. This allows $|s|$ to be varied over a wide range on the order of hundreds of μeV using this technique. Remarkably, all QDs in a given wafer are observed to have the same rate of change of $|s|$ with electric field.

As $|s|$ is reduced, coherent coupling between the two exciton eigenstates results in the observation of an anticrossing as the states are inverted. This imposes a lower limit, s_0, below which the FSS can not be reduced using this tuning method. The value of s_0 varies between QDs. One QD, which has $|s| > 50$ μeV in the absence of an electric field, has been tuned to have $|s| = s_0 = 1.4$ μeV. Entangled photon pairs have been observed from this QD, with the fidelity of the emitted two-photon state to the ideal Bell state

found to be dependent on $|s|$ as expected.

The effects of an applied magnetic field on the FSS have also been explored. It is found that a magnetic field does not affect the value of s_0, but does change the electric field required to tune a QD to $|s| = s_0$. Consequently, the energy of emission from the neutral transitions when $|s| = s_0$ is dependent on the magnitude of the magnetic field. This allows the potential creation of an energy-tuneable source of entangled photon pairs via simultaneous application of electric and magnetic fields. Calculations show that such a source could have a tuning range of several tens of meV with the application of a modest magnetic field on the order of 10 T.

8.1.2 Control of the exciton state

The neutral exciton state is of interest to the work in this thesis due to the potential of confined excitons to provide an optically accessible spin system for use as a solid-state qubit. The coherent mapping between the polarisation of a photon and the spin state of the created exciton has been used in order to initialise such a qubit. This is interesting as it demonstrates the potential to use the interaction between photonic qubits and nanostructures as a bridge between optical and solid-state quantum computing schemes. Such an interface has applications in the creation of a hybrid computation regime, in which the benefits of each qubit system can be combined so as to mitigate some of the drawbacks of each individual mode of computation.

The exciton state has been studied as a function of time, allowing the fluctuating nuclear field to be probed. The nuclear field was found to influence the rate at which the spin state of a confined exciton processes around the Bloch sphere, via the addition of a time-fluctuating component to the FSS.

Dynamic manipulation of the FSS was achieved via the application of a time varying electric field. This has been used as a method to implement a controlled phase rotation of the exciton state, which is then transferred to the emitted photon when the exciton radiatively decays. Thus a phase shift has been applied to a photonic qubit, by first writing the qubit state

to the spin of an exciton and then performing the rotation operation in the solid-state before the exciton recombines.

8.1.3 Demonstration of an integrated photonic logic circuit

A single QD embedded inside a pillar microcavity has been used as an on-demand single photon source to generate the input state for an integrated photonic controlled-NOT gate. The neutral exciton transition was used to emitted single photons, whilst the coupling of this transition to the cavity mode of the pillar increased the indistinguishability of the emitted photons.

This work is the first demonstration of a two-qubit gate using on-demand single photons, and as such is currently the closest to the seminal proposal for linear optical quantum computing by Knill, Laflamme, and Milburn[82]. In addition, all the components for this gate are realised using semiconductor technology. As such this work represents a significant step towards a scalable quantum computing platform in the solid-state.

8.2 Future work

The work in this thesis has developed several components which have applications in the field of quantum computing. Much work remains, however, before a viable large scale optical quantum computation scheme can be implemented.

Following on from this thesis, it would be interesting to extend the FSS tuning method to include a third tuning mechanism in addition to the electric and magnetic fields considered here. A promising mechanism would be a piezo induced strain field, as recent studies have reported that variation of the strain field can result in the elimination of the coupling between the exciton eigenstates and thus allow $|s|$ to be tuned to zero. As well as increasing the degree of useable entanglement between the two photons emitted by the neutral biexciton cascade, the ability to tune any QD to $|s| = 0$ would remove the requirement to "cherry pick" QDs with small s_0 for use in quantum

optics applications. This increase in device yield would be an important step towards the scaling up of methods which require QDs for the creation non-classical light states.

Another possible avenue for further research would be to further investigate the g-factors of the carriers within a QD as a function of electric field. In particular, the component that lies in the plane of the sample has not been investigated in this thesis. In principle, this component can be measured via probing the emission from the charged exciton states.

Finally, there are several ways in which the two-qubit photonic gate presented in this work could be developed to enhance its performance. The photon source and detector could be integrated directly into the waveguide circuitry, which would allow further miniturisation of the system. Also, in the work presented here a single QD is used to provide both photons for the two-photon input state, which is achieved with a probability of $\frac{1}{4}$. An interesting extension would be to incorporate two synchronised single photon sources, which would allow deterministic initialisation of the input state. Such deterministic input state generation is required in order to efficiently operate circuits consisting of many gates, thus this would be an important step closer to the creation of a scalable optical quantum computer.

References

[1] P. Michler, editor. *Single Semiconductor Quantum Dots*. Springer Berlin Heidelberg, 2009.

[2] D. Bimberg, M. Grundmann, and N. N. Ledenstov. *Quantum Dot Heterostructures*. John wiley & Sons, 1999.

[3] C. Kittel. *Introduction to solid state physics*. John wiley & Sons, 2004.

[4] J. R. Hook and H. E. Hall. *Solid state physics*. John wiley & Sons, 1991.

[5] J. Stangl, V. Holy, and G. Bauer. Structural properties of self-organized semiconductor nanostructures. *Rev. Mod. Phys.*, 76:725–783, 2004.

[6] H. A. Herman and H. Sitter. Molecular beam epitaxy: Fundamentals and current status. *Springer*, 1989.

[7] D. Leonard, M. Krishnamurthy, C. M. Reaves, S. P. Denbaars, and P. M. Petroff. Direct formation of quantum-sized dots from uniform coherent islands of InGaAs surfaces. *Appl. Phys. Lett.*, 63:3203, 1993.

[8] Z. Yuan, B. E. Kardynal, R. M. Stevenson, A. J. Shields, C. J. Lobo, K. Cooper, N. S. Beattie, D. A. Ritchie, and M. Pepper. Electrically driven single-photon source. *Science*, 295(5552):102–105, January 2002.

[9] C. L. Salter, R. M. Stevenson, I. Farrer, C. A. Nicoll, D. A. Ritchie, and A. J. Shields. An entangled-light-emitting diode. *Nature*, 465(7298):594–597, June 2010.

[10] J. R. Gell, M. B. Ward, R. J. Young, R. M. Stevenson, P. Atkinson, D. Anderson, G. A. C. Jones, D. A. Ritchie, and A. J. Shields. Modulation of single quantum dot energy levels by a surface-acoustic-wave. *Appl. Phys. Lett.*, 93(8):081115–3, August 2008.

[11] R. P. G. McNeil, M. Kataoka, C. J. B. Ford, C. H. W. Barnes, D. Anderson, G. A. C. Jones, I. Farrer, and D. A. Ritchie. On-demand single-electron transfer between distant quantum dots. *Nature*, 477(7365):439–442, September 2011.

[12] F. Adler, M. Geiger, A. Bauknecht, F. Scholz, H. Schweizer, M. H. Pilkuhn, B. Ohnesorge, and A. Forchel. Optical transitions and carrier relaxation in self assembled InAs/GaAs quantum dots. *J. Appl. Phys.*, 80(7):4019–4026, October 1996.

[13] R. Heitz, M. Grundmann, N. N. Ledentsov, L. Eckey, M. Veit, D. Bimberg, V. M. Ustinov, A. Yu. Egorov, A. E. Zhukov, P. S. Kop'ev, and Zh. I. Alferov. Multiphonon-relaxation processes in self-organized InAs/GaAs quantum dots. *Appl. Phys. Lett.*, 68(3):361–363, January 1996.

[14] D. Strauch and B. Dorner. Phonon dispersion in GaAs. *J. Phys.:Condens. Matter*, 2:1457, 1990.

[15] M. Bayer, G. Ortner, O. Stern, A. Kuther, A. A. Gorbunov, A. Forchel, P. Hawrylak, S. Fafard, K. Hinzer, T. L. Reinecke, S. N. Walck, J. P. Reithmaier, F. Klopf, and F. Schafer, F.fer. Fine structure of neutral and charged excitons in self-assembled In(Ga)As/(Al)GaAs quantum dots. *Phys. Rev. B*, 65(19):195315–, May 2002.

[16] F. Patella, S. Nufris, F. Arciprete, M. Fanfoni, E. Placidi, A. Sgarlata, and A. Balzarotti. Tracing the two- to three-dimensional transition in the inas/gaas(001) heteroepitaxial growth. *Phys. Rev. B*, 67(20):205308–, May 2003.

[17] Tomoya Inoue, Takashi Kita, Osamu Wada, Mitsuru Konno, Toshie Yaguchi, and Takeo Kamino. Electron tomography of embedded semiconductor quantum dot. *Appl. Phys. Lett.*, 92(3):031902–3, January 2008.

[18] M. Grundmann, O. Stier, and D. Bimberg. InAs/GaAs pyramidal quantum dots: Strain distribution, optical phonons, and electronic structure. *Phys. Rev. B*, 52(16):11969–11981, October 1995.

[19] R. M. Stevenson, A. J. Hudson, A. J. Bennett, R. J. Young, C. A. Nicoll, D. A. Ritchie, and A. J. Shields. Evolution of entanglement between distinguishable light states. *Phys. Rev. Lett.*, 101(17):170501–, October 2008.

[20] A. Boyer de la Giroday, A. J. Bennett, M. A. Pooley, R. M. Stevenson, N. Skold, N.ld, R. B. Patel, I. Farrer, D. A. Ritchie, and A. J. Shields. All-electrical coherent control of the exciton states in a single quantum dot. *Phys. Rev. B*, 82(24):241301–, December 2010.

[21] E. M. Purcell. Measurement of magnetic resonance absorption by nuclear moments in a solid. *Phys. Rev.*, 69:681, 1946.

[22] M. Fox. *Quantum Optics: An Introduction.* Oxford University Press, 2006.

[23] A. J. Bennett, R. B. Patel, J. Skiba-Szymanska, C. A. Nicoll, I. Farrer, D. A. Ritchie, and A. J. Shields. Giant stark effect in the emission of single semiconductor quantum dots. *Appl. Phys. Lett.*, 97(3):031104–3, July 2010.

[24] V. Zwiller, T. Aichele, and O. Benson. Quantum optics with single quantum dot devices. *New Journal of Physics*, 6(1):96–, 2004.

[25] A. J. Bennett, P. Atkinson, P. See, M. B. Ward, R. M. Stevenson, Z. L. Yuan, D. C. Unitt, D. J. P. Ellis, K. Cooper, D. A. Ritchie, and A. J. Shields. Single-photon-emitting diodes: a review. *Phys. Stat. Sol. (b)*, 243(14):3730–3740, 2006.

[26] J. S. Orfanidis. *Electromagnetic waves and antennas*. Rutgers University, 2002.

[27] O. Benson, C. Santori, M. Pelton, and Y. Yamamoto. Regulated and entangled photons from a single quantum dot. *Phys. Rev. Lett.*, 84(11):2513–2516, March 2000.

[28] S. Seidl, M. Kroner, A. Hogele, K. Karrai, R. J. Warburton, A. Badolato, and P. M. Petroff. Effect of uniaxial stress on excitons in a self-assembled quantum dot. *Appl. Phys. Lett.*, 88(20):203113–3, May 2006.

[29] Ranber Singh and Gabriel Bester. Lower bound for the excitonic fine structure splitting in self-assembled quantum dots. *Phys. Rev. Lett.*, 104(19):196803–, May 2010.

[30] Garnett W. Bryant, M. Zielinski, Natalia Malkova, James Sims, W. Jaskolski, and Javier Aizpurua. Effect of mechanical strain on the optical properties of quantum dots: Controlling exciton shape, orientation, and phase with a mechanical strain. *Phys. Rev. Lett.*, 105(6):067404–, August 2010.

[31] Ming Gong, Weiwei Zhang, Guang-Can Guo, and Lixin He. Exciton polarization, fine-structure splitting, and the asymmetry of quantum dots under uniaxial stress. *Phys. Rev. Lett.*, 106(22):227401–, May 2011.

[32] R. M. Stevenson, R. J. Young, P. See, D. G. Gevaux, K. Cooper, P. Atkinson, I. Farrer, D. A. Ritchie, and A. J. Shields. Magnetic-field-induced reduction of the exciton polarization splitting in inas quantum dots. *Phys. Rev. B*, 73(3):033306–, January 2006.

[33] M. Bayer, A. Kuther, A. Forchel, A. Gorbunov, V. B. Timofeev, F. Schafer, J. P. Reithmaier, T. L. Reinecke, and S. N. Walck. Electron and hole g factors and exchange interaction from studies of the

exciton fine structure in $In_{0.60}Ga_{0.40}As$ quantum dots. *Phys. Rev. Lett.*, 82(8):1748–, February 1999.

[34] G. Jundt, L. Robledo, A. Hogele, S. Falt, and A. Imamoglu. Observation of dressed excitonic states in a single quantum dot. *Phys. Rev. Lett.*, 100(17):177401–, April 2008.

[35] A. Muller, W. Fang, J. Lawall, and G. S. Solomon. Creating polarization-entangled photon pairs from a semiconductor quantum dot using the optical stark effect. *Phys. Rev. Lett.*, 103(21):217402–, November 2009.

[36] K. Kowalik, O. Krebs, A. Lemaitre, B. Eble, A. Kudelski, P. Voisin, S. Seidl, and J. A. Gaj. Monitoring electrically driven cancellation of exciton fine structure in a semiconductor quantum dot by optical orientation. *Appl. Phys. Lett.*, 91(18):183104–3, October 2007.

[37] B. D. Gerardot, S. Seidl, P. A. Dalgarno, R. J. Warburton, D. Granados, J. M. Garcia, K. Kowalik, O. Krebs, K. Karrai, A. Badolato, and P. M. Petroff. Manipulating exciton fine structure in quantum dots with a lateral electric field. *Appl. Phys. Lett.*, 90(4):041101–3, January 2007.

[38] M. M. Vogel, S. M. Ulrich, R. Hafenbrak, P. Michler, L. Wang, A. Rastelli, and O. G. Schmidt. Influence of lateral electric fields on multiexcitonic transitions and fine structure of single quantum dots. *Appl. Phys. Lett.*, 91(5):051904–3, July 2007.

[39] S. Marcet, K. Ohtani, and H. Ohno. Vertical electric field tuning of the exciton fine structure splitting and photon correlation measurements of gaas quantum dot. *Appl. Phys. Lett.*, 96(10):101117–3, March 2010.

[40] K. Kowalik, O. Krebs, P. Senellart, A. Lemaitre, B. Eble, A. Kudelski, J. Gaj, and P. Voisin. Stark spectroscopy of coulomb interactions in individual InAs/GaAs self-assembled quantum dots. *physica status solidi (c)*, 3(11):3890–3894, 2006.

[41] A. J. Bennett, M. A. Pooley, R. M. Stevenson, M. B. Ward, R. B. Patel, A. Boyer de la Giroday, N. Skold, I. Farrer, C. A. Nicoll, D. A. Ritchie, and A. J. Shields. Electric-field-induced coherent coupling of the exciton states in a single quantum dot. *Nat Phys*, 6(12):947–950, December 2010.

[42] A. J. Williamson and A. Zunger. InAs quantum dots: Predicted electronic structure of free-standing versus GaAs-embedded structures. *Phys. Rev. B*, 59(24):15819–15824, June 1999.

[43] O. Stier, M. Grundmann, and D. Bimberg. Electronic and optical properties of strained quantum dots modeled by 8-band k.p theory. *Phys. Rev. B*, 59(8):5688–5701, February 1999.

[44] J. J. Finley, M. Sabathil, P. Vogl, G. Abstreiter, R. Oulton, A. I. Tartakovskii, D. J. Mowbray, M. S. Skolnick, S. L. Liew, A. G. Cullis, and M. Hopkinson. Quantum-confined stark shifts of charged exciton complexes in quantum dots. *Phys. Rev. B*, 70(20):201308–, November 2004.

[45] J. A. Barker and E. P. O'Reilly. Theoretical analysis of electron-hole alignment in InAs-GaAs quantum dots. *Phys. Rev. B*, 61(20):13840–, May 2000.

[46] R. P. Feynman, R. B. Leighton, and M. Sands. *The Feynman Lectures on Physics*, volume 1. Addison-Weasley, 1963.

[47] G. Khitrova, H. M. Gibbs, M. Kira, S. W. Koch, and A. Scherer. Vacuum rabi splitting in semiconductors. *Nat Phys*, 2(2):81–90, February 2006.

[48] E. A. Stinaff, M. Scheibner, A. S. Bracker, I. V. Ponomarev, V. L. Korenev, M. E. Ware, M. F. Doty, T. L. Reinecke, and D. Gammon. Optical signatures of coupled quantum dots. *Science*, 311(5761):636–639, February 2006.

[49] R. J. Young, R. M. Stevenson, A. J. Shields, P. Atkinson, K. Cooper, D. A. Ritchie, K. M. Groom, A. I. Tartakovskii, and M. S. Skolnick. Inversion of exciton level splitting in quantum dots. *Phys. Rev. B*, 72(11):113305–, September 2005.

[50] S. Seidl, B.D. Gerardot, P.A. Dalgarno, K. Kowalik, A.W. Holleitner, P.M. Petroff, K. Karrai, and R.J. Warburton. Statistics of quantum dot exciton fine structure splittings and their polarization orientations. *Physica E: Low-dimensional Systems and Nanostructures*, 40(6):2153–2155, April 2008.

[51] R. B. Patel, A. J. Bennett, I. Farrer, C. A. Nicoll, D. A. Ritchie, and A. J. Shields. Two-photon interference of the emission from electrically tunable remote quantum dots. *Nat Photon*, 4(9):632–635, September 2010.

[52] R. M. Stevenson, R. J. Young, P. Atkinson, K. Cooper, D. A. Ritchie, and A. J. Shields. A semiconductor source of triggered entangled photon pairs. *Nature*, 439(7073):179–182, January 2006.

[53] R Hafenbrak, S M Ulrich, P Michler, L Wang, A Rastelli, and O G Schmidt. Triggered polarization-entangled photon pairs from a single quantum dot up to 30 k. *New Journal of Physics*, 9(9):315–, 2007.

[54] A. J. Hudson, R. M. Stevenson, A. J. Bennett, R. J. Young, C. A. Nicoll, P. Atkinson, K. Cooper, D. A. Ritchie, and A. J. Shields. Coherence of an entangled exciton-photon state. *Physical Review Letters*, 99(26), 2007.

[55] J. Wang, M. Gong, G. Guo, and L. He. Eliminating the fine structure splitting of excitons in self-assembled InAs/GaAs quantum dots via combined stresses. *Appl. Phys. Lett.*, 101(6):063114–4, August 2012.

[56] R. Trotta, E. Zallo, C. Ortix, P. Atkinson, J. D. Plumhof, J. van den Brink, A. Rastelli, and O. G. Schmidt. Universal recovery of the energy-

level degeneracy of bright excitons in ingaas quantum dots without a structure symmetry. *Phys. Rev. Lett.*, 109(14):147401–, October 2012.

[57] Y. Kato, R. C. Myers, D. C. Driscoll, A. C. Gossard, J. Levy, and D. D. Awschalom. Gigahertz electron spin manipulation using voltage-controlled g-tensor modulation. *Science*, 299(5610):1201–1204, February 2003.

[58] J. Pingenot, C. E. Pryor, and M. E. Flatte. Method for full bloch sphere control of a localized spin via a single electrical gate. *Appl. Phys. Lett.*, 92(22):222502–3, June 2008.

[59] F. Klotz, V. Jovanov, J. Kierig, E. C. Clark, D. Rudolph, D. Heiss, M. Bichler, G. Abstreiter, M. S. Brandt, and J. J. Finley. Observation of an electrically tunable exciton g factor in InGaAs/GaAs quantum dots. *Applied Physics Letters*, 96(5):053113, 2010.

[60] R. S. Deacon, Y. Kanai, S. Takahashi, A. Oiwa, K. Yoshida, K. Shibata, K. Hirakawa, Y. Tokura, and S. Tarucha. Electrically tuned g tensor in an InAs self-assembled quantum dot. *Phys. Rev. B*, 84(4):041302–, July 2011.

[61] V. Jovanov, T. Eissfeller, S. Kapfinger, E. C. Clark, F. Klotz, M. Bichler, J. G. Keizer, P. M. Koenraad, G. Abstreiter, and J. J. Finley. Observation and explanation of strong electrically tunable exciton g factors in composition engineered In(Ga)As quantum dots. *Phys. Rev. B*, 83(16):161303–, April 2011.

[62] T. Nakaoka, T. Saito, J. Tatebayashi, and Y. Arakawa. Size, shape, and strain dependence of the g factor in self-assembled In(Ga)As quantum dots. *Phys. Rev. B*, 70(23):235337–, December 2004.

[63] J. Pingenot, C. E. Pryor, and M. E. Flatte. Electric-field manipulation of the lande g tensor of a hole in an $In_{0.5}Ga_{0.5}As$/GaAs self-assembled quantum dot. *Phys. Rev. B*, 84(19):195403–, November 2011.

[64] A. J. Bennett, M. A. Pooley, R. M. Stevenson, I. Farrer, D. A. Ritchie, and A. J. Shields. Free induction decay of a superposition stored in a quantum dot. *Phys. Rev. B*, 84(19):195401–, November 2011.

[65] D. Loss and D. P. DiVincenzo. Quantum computation with quantum dots. *Phys. Rev. A*, 57(1):120–126, January 1998.

[66] F. H. L. Koppens, C. Buizert, K. J. Tielrooij, I. T. Vink, K. C. Nowack, T. Meunier, L. P. Kouwenhoven, and L. M. K. Vandersypen. Driven coherent oscillations of a single electron spin in a quantum dot. *Nature*, 442(7104):766–771, August 2006.

[67] D. Press, T. D. Ladd, B. Zhang, and Y. Yamamoto. Complete quantum control of a single quantum dot spin using ultrafast optical pulses. *Nature*, 456(7219):218–221, November 2008.

[68] A. Morello, J. J. Pla, F. A. Zwanenburg, K. W. Chan, K. Y. Tan, H. Huebl, M. Mottonen, C. D. Nugroho, C. Yang, J. A. van Donkelaar, A. D. C. Alves, D. N. Jamieson, C. C. Escott, L. C. L. Hollenberg, R. G. Clark, and A. S. Dzurak. Single-shot readout of an electron spin in silicon. *Nature*, 467(7316):687–691, October 2010.

[69] P. Neumann, J. Beck, M. Steiner, F. Rempp, H. Fedder, P. R. Hemmer, J. Wrachtrup, and F. Jelezko. Single-shot readout of a single nuclear spin. *Science*, 329(5991):542–544, July 2010.

[70] D. Gammon, Al. L. Efros, T. A. Kennedy, M. Rosen, D. S. Katzer, D. Park, S. W. Brown, V. L. Korenev, and I. A. Merkulov. Electron and nuclear spin interactions in the optical spectra of single GaAs quantum dots. *Phys. Rev. Lett.*, 86(22):5176–5179, May 2001.

[71] J. M. Kikkawa and D. D. Awschalom. All-optical magnetic resonance in semiconductors. *Science*, 287(5452):473–476, January 2000.

[72] A. I. Tartakovskii, T. Wright, A. Russell, V. I. Fal'ko, A. B. Van'kov, J. Skiba-Szymanska, I. Drouzas, R. S. Kolodka, M. S. Skolnick, P. W.

Fry, A. Tahraoui, H.-Y. Liu, and M. Hopkinson. Nuclear spin switch in semiconductor quantum dots. *Phys. Rev. Lett.*, 98(2):026806–, January 2007.

[73] C. Latta, A. Hogele, Y. Zhao, A. N. Vamivakas, P. Maletinsky, M. Kroner, J. Dreiser, I. Carusotto, A. Badolato, D. Schuh, W. Wegscheider, M. Atature, and A. Imamoglu. Confluence of resonant laser excitation and bidirectional quantum-dot nuclear-spin polarization. *Nat Phys*, 5(10):758–763, October 2009.

[74] H. Kosaka, H. Shigyou, Y. Mitsumori, Y. Rikitake, H. Imamura, T. Kutsuwa, K. Arai, and K. Edamatsu. Coherent transfer of light polarization to electron spins in a semiconductor. *Phys. Rev. Lett.*, 100(9):096602–, March 2008.

[75] N. Gisin, G. Ribordy, W. Tittel, and H. Zbinden. Quantum cryptography. *Rev. Mod. Phys.*, 74(1):145–, March 2002.

[76] R. Ursin, F. Tiefenbacher, T. Schmitt-Manderbach, H. Weier, T. Scheidl, M. Lindenthal, B. Blauensteiner, T. Jennewein, J. Perdigues, P. Trojek, B. Omer, M. Furst, M. Meyenburg, J. Rarity, Z. Sodnik, C. Barbieri, H. Weinfurter, and A. Zeilinger. Entanglement-based quantum communication over 144 km. *Nat Phys*, 3(7):481–486, July 2007.

[77] T. Flissikowski, A. Hundt, M. Lowisch, M. Rabe, and F. Henneberger. Photon beats from a single semiconductor quantum dot. *Phys. Rev. Lett.*, 86(14):3172–3175, April 2001.

[78] P. Maletinsky, A. Badolato, and A. Imamoglu. Dynamics of quantum dot nuclear spin polarization controlled by a single electron. *Phys. Rev. Lett.*, 99(5):056804–, August 2007.

[79] K. Harris, R. *Nuclear Magnetic Resonance Spectroscopy.* Wiley, 1986.

[80] R. J. Abraham, J. Fisher, and P. Loftus. *Introduction to NMR Spectroscopy.* Wiley, 1988.

[81] A. Mohan, M. Felici, Gallo P., B. Dwir, A. Rudra, J. Faist, and E. Kapon. Polarization-entangled photons produced with high-symmetry site-controlled quantum dots. *Nat Photon*, 4(5):302–306, May 2010.

[82] E. Knill, R. Laflamme, and G. J. Milburn. A scheme for efficient quantum computation with linear optics. *Nature*, 409(6816):46–52, January 2001.

[83] R. Raussendorf and H. J. Briegel. A one-way quantum computer. *Phys. Rev. Lett.*, 86(22):5188–5191, May 2001.

[84] D. E. Browne and T. Rudolph. Resource-efficient linear optical quantum computation. *Phys. Rev. Lett.*, 95(1):010501–, June 2005.

[85] P. Kok, W. J. Munro, K. Nemoto, T. C. Ralph, J. P. Dowling, and G. J. Milburn. Linear optical quantum computing with photonic qubits. *Rev. Mod. Phys.*, 79(1):135–174, January 2007.

[86] S. Gasparoni, J. Pan, P. Walther, T. Rudolph, and A. Zeilinger. Realization of a photonic controlled-not gate sufficient for quantum computation. *Phys. Rev. Lett.*, 93(2):020504–, July 2004.

[87] J. L. O'Brien, G. J. Pryde, A. G. White, T. C. Ralph, and D. Branning. Demonstration of an all-optical quantum controlled-not gate. *Nature*, 426(6964):264–267, November 2003.

[88] R. Okamoto, H. F. Hofmann, S. Takeuchi, and K. Sasaki. Demonstration of an optical quantum controlled-not gate without path interference. *Phys. Rev. Lett.*, 95(21):210506–, November 2005.

[89] A. Politi, M. J. Cryan, J. G. Rarity, S. Yu, and J. L. O'Brien. Silica-on-silicon waveguide quantum circuits. *Science*, 320(5876):646–649, 2008.

[90] B. Lounis and W. E. Moerner. Single photons on demand from a single molecule at room temperature. *Nature*, 407(6803):491–493, September 2000.

[91] C. Brunel, B. Lounis, P. Tamarat, and M. Orrit. Triggered source of single photons based on controlled single molecule fluorescence. *Phys. Rev. Lett.*, 83(14):2722–2725, October 1999.

[92] A. Kuhn, M. Hennrich, and G. Rempe. Deterministic single-photon source for distributed quantum networking. *Phys. Rev. Lett.*, 89(6):067901–, July 2002.

[93] A. Gruber, A. Drabenstedt, C. Tietz, L. Fleury, J. Wrachtrup, and C. von Borczyskowski. Scanning confocal optical microscopy and magnetic resonance on single defect centers. *Science*, 276(5321):2012–2014, 1997.

[94] Christian Kurtsiefer, Sonja Mayer, Patrick Zarda, and Harald Weinfurter. Stable solid-state source of single photons. *Phys. Rev. Lett.*, 85(2):290–293, July 2000.

[95] P. Michler, A. Kiraz, C. Becher, W. V. Schoenfeld, P. M. Petroff, Lidong Zhang, E. Hu, and A. Imamoglu. A quantum dot single-photon turnstile device. *Science*, 290(5500):2282–2285, December 2000.

[96] T. C. Ralph, N. K. Langford, T. B. Bell, and A. G. White. Linear optical controlled-not gate in the coincidence basis. *Phys. Rev. A*, 65(6):062324–, June 2002.

[97] D. C. Unitt. *Enhanced Single Photon emission from a Quantum Dot in a Semionductor Microcavity.* PhD thesis, University of Cambridge, 2005.

[98] C. K. Hong, Z. Y. Ou, and L. Mandel. Measurement of subpicosecond time intervals between two photons by interference. *Phys. Rev. Lett.*, 59(18):2044–2046, November 1987.

[99] T. Legero, T. Wilk, A. Kuhn, and G. Rempe. Time-resolved two-photon quantum interference, 2003-12-01.

[100] C. Santori, D. Fattal, K. C Fu, P. E Barclay, and R. G. Beausoleil. On the indistinguishability of raman photons. *New Journal of Physics*, 11(12):123009–, 2009.

[101] A. Kiraz, M. Atature, and A. Imamoglu. Quantum-dot single-photon sources: Prospects for applications in linear optics quantum-information processing. *Phys. Rev. A*, 69(3):032305–, March 2004.

[102] H. S. Nguyen, G. Sallen, C. Voisin, Ph. Roussignol, C. Diederichs, and G. Cassabois. Ultra-coherent single photon source. *Appl. Phys. Lett.*, 99(26):261904–3, December 2011.